Magnetic Reconnection Physics in the Solar Wind with Voyager 2

by

Michael L. Stevens

SM Physics
Massachusetts Institute of Technology (2006)
BA Physics
Cornell University (2002)

Submitted to the Department of Physics
in partial fulfillment of the requirements for the degree of

Doctor of Philosophy in Physics

at the

MASSACHUSETTS INSTITUTE OF TECHNOLOGY

June 2009

Author .....
Department of Physics
May 25, 2009

Certified by .....
John W. Belcher
Professor of Physics
Thesis Supervisor

Certified by .....
Thomas J. Greytak
Professor of Physics
Associate Department Head for Education

Magnetic Reconnection Physics in the Solar Wind with Voyager 2

by
Michael L. Stevens

Submitted to the Department of Physics
on May 25, 2009 in partial fulfillment of the
requirements for the degree of
Doctor of Philosophy in Physics

Abstract

Magnetic reconnection is the process by which the magnetic topology evolves in collisionless plasmas. This phenomenon is fundamental to a broad range of astrophysical processes such as stellar flares, magnetospheric substorms, and plasma accretion, yet it is poorly understood and difficult to observe *in situ*. In this thesis, the solar wind plasma permeating interplanetary space is treated as a laboratory for reconnection physics.

I present an exhaustive statistical approach to the identification of reconnection outflow jets in turbulent plasma and magnetic field time series data. This approach has been automated and characterized so that the resulting reconnection survey can be put in context with other related studies. The algorithm is shown to perform similarly to *ad hoc* studies in the inner heliosphere.

Based on this technique, I present a survey of 138 outflow jets for the Voyager 2 spacecraft mission, including the most distant *in situ* evidence of reconnection discovered to date. Reconnection in the solar wind is shown to be strongly correlated with stream interactions and with solar activity. The solar wind magnetic field is found to be reconnecting via large, quasi-steady slow-mode magnetohydrodynamic structures as far out as the orbit of Neptune. The role of slow-mode shocks is explored and, in one instance, a well-developed reconnection structure is shown to be in good agreement with the Petschek theory for fast reconnection. This is the first reported example of a reconnection exhaust that satisfies the full jump conditions for a stationary slow-mode shock pair.

A complete investigation into corotating stream interactions over the Voyager 2 mission has revealed that detectable reconnection structure occurs in about 23% of forced, global-scale current sheets. Contrary to previous studies, I find that signatures of this kind are most likely to be observed for current sheets where the magnetic field shear and the plasma-β are high. Evidence has been found of thinning in Kelvin-Helmholtz unstable reconnection structures. I hypothesize that reconnection in turbulent environments occurs predominantly on smaller scales than one can measure with Voyager 2.

Thesis Supervisor: John W. Belcher
Title: Professor of Physics

Acknowledgements

I would like to extend my deepest thanks, first and foremost, to my family for their inspiration, love, and support. I thank my parents, Jean and Ernest Stevens, who have encouraged me to follow my every ambition in life and then driven me, literally and figuratively, wherever I needed to go to succeed. I thank my sister, Cathy, who has been an inexhaustible source of enthusiasm and a centering influence. Thank you to my grandparents, Gladys Hayward and Ray LaBounty, who encouraged me from the first and contributed so much to my education. I also give special thanks to my honorary aunt, Betsey Wimperis, for giving a homeless graduate student his own Walden Pond from which to write.

Thank you to my thesis supervisor, John Belcher, and mentors, Al Lazarus and Justin Kasper. It has been a privilege and a pleasure to work with you, and I am extremely grateful for the opportunities that you have given me. Thank you also to the space plasma group at MIT, including Justin Ashmall, Slobodan Jurac, John Richardson, Ying Liu, and Leslie Finck for helping me to make the transition to astrophysics, and for continuously sharing your time and expertise. I am especially indebted to the tireless Anne MacAskill, through whom everything is possible (and with whom, everything is more fun). I have also been fortunate to have excellent mentors in the space physics community at large. I am particularly grateful to Keith Ogilvie, John Steinberg, Adam Szabo, Chuck Smith, Chadi Salem, Len Burlaga, Jack Gosling, and Harlan Spence for taking an interest in my career, taking the time to correspond with me, and for sharing their expertise.

Like so many of my peers, I am indebted to Al Levine, the patron saint of the astrophysics qualification exam. Thank you all of your time and compassion.

Thank you to my fellow graduate students for your comaraderie and for so many stimulating discussions. Thanks especially to my conference accomplices, Christina Prested, Pin Wu, Tulasi Parashar, Kevin Schoeffler, and Ben Maruca. Thank you also to my fellow students, fantasy baseball opponents, and foosball pupils in MIT physics, including Ben Cain, Robyn Sanderson, Jeff Blackburne, Josh Carter, Aidan Crook, Tamer Elkholy, Will Farr, Dacheng Lin, Adrian Liu, Philip Zukin, Sarah Vigeland, Chris Williams, Molly Swanson, Jake Hartman, Miriam Krauss, Leo Stein, Jared Markowitz, and Andrew Grier. I am also very grateful for the good humor of my officemates and neighbors Stephen O'Sullivan, Anajali Tripathi, Paola Rebusco, and Balu, through many late nights and early mornings.

I am grateful for the indulgence of my good friends here in Boston, without whom I would be a dim-witted teetotaller, lacking all but the most rudimentary knowledge of 19th century U.S. Presidents, world geography, teen actors, and college sports. They are Ari Friedland, Emily Vincent, Zach Perez, Jon Lee, Greer Muldowny, Eric Nelson, Brock Bose, Sarah Forrest, and Leah Premo.

Finally, thank you with all of my heart to Kieran Pechter, whose unflagging support I dearly wish I could repay.

Contents

List of Figures

List of Tables

Chapter 1

Introduction

Magnetic reconnection (MR) is a fundamental plasma process in nature. Astrophysical plasmas, such as those found in the sun's corona, in interplanetary and interstellar space, and in the disks of gravitationally accreting objects, typically carry strong magnetic fields that rigidly constrain two degrees of freedom for charged particles. As a result, the connectivity between plasma elements that lie on the same line of magnetic force plays a central role in plasma dynamics. When plasmas are deformed in such a way as to alter that connectivity, some or all of the magnetic energy associated with particle confinement in those two degrees of freedom may be liberated. Virtually all plasmas experience this very general effect, yet understanding it in a general way presents a significant theoretical challenge.

A large amount of cross-disciplinary research effort is presently dedicated to magnetic reconnection, including numerical simulation, laboratory experiments, indirect observation, and direct, space-based observation. One reason that the subject receives so much attention is because, like many of the most significant problems in the field of plasma physics, reconnection involves microscale physics that manifests itself on a large scale. The most successful theoretical tool for understanding the dynamics of strongly magnetized plasmas on large scales is magnetohydrodynamic (MHD) fluid theory, yet changes in field-line connectivity involve particle-field interactions on scales that are too small for the plasma to behave as a fluid. Magnetic reconnection belongs to the class of problems that are too large and complex to simulate or model kinetically, but apparently too strongly rooted in nonlinear kinetic physics to be successfully simulated or modeled otherwise.

For problems of this nature, the widest possible range of observations must be pursued to guide our numerical and theoretical efforts. The largest and best available laboratory for directly observing many of these processes is in space. Today, a growing number of spacecraft-based experiments provide

continuous measurements of fields and particle distributions in the earth's magnetosphere, in interplanetary space, and beyond. The vast majority of these spacecraft are earth-orbiting, and the phenomenology of reconnection between the magnetic fields of the sun and the earth's magnetosphere, for example, has been observed directly for three decades (e.g. [69, 89]).

Examples of kinetic processes playing a central role in fluid-like plasmas abound in space (see, for example, [60]). Recently, kinetic instabilities have been shown to play a significant role in limiting deviations from thermodynamic equilibrium in the solar wind [42, 51]. The saturation of the kinetic magnetic mirror instability has been linked to large-scale magnetic flux depletions in the solar wind by several studies [58, 65, 90, 98]. Cyclotron-resonant wave absorption has been explored as a major source of acceleration and heating in solar wind origination theories [3, 20, 55]. The conversion of MHD wave energy to particle kinetic energy in dissipative turbulence is expected to be a significant source of heating in the solar wind and the corona [19, 54].

Magnetic reconnection is particularly important in space physics because it is involved in any release of magnetically confined plasma or mixing of magnetically separated plasma. Solar flares and coronal mass ejections are examples of eruptive processes on the sun that require magnetic reconnection in order to release magnetically confined masses of plasma [1, 86, 96]. The micro-flare theory of the solar wind generalizes the flare process to all solar wind release (e.g. [95]), while another popular theory models solar wind release as a reconnective diffusion of open field lines away from coronal holes [22]. Magnetic reconnection is also required to transfer solar wind plasma from the solar wind's magnetic field to the earth's. Magnetic reconnection at the dayside magnetopause and in the magnetotail dictates the geoeffectiveness of the solar wind and space weather [30, 46, 82]. It has also been hypothesized that reconnection plays a major role in dissipative turbulence, converting magnetic energy at the thin current sheets bounding turbulent eddies [61].

1.1 Reconnection in the Solar Wind

Reconnection theory is specifically concerned with so-called "fast reconnection," the family of reconnection processes that cannot be mediated by simple Ohmic diffusion, as in weakly resistive MHD. In space plasma physics, the extremely slow rate at which magnetic fields diffuse through the plasma is insufficient to account for any of the phenomena we have mentioned. Similarly, reconnection of the solar wind magnetic field in interplanetary space is certain to be fast when it occurs. Until recently, however, the subject of solar wind reconnection was largely unaddressed, despite a series of plasma probe missions in interplanetary space including Helios, Wind, ACE, Voyager, Ulysses, and others. Perhaps these missions had been overlooked by the reconnection community because the solar wind does not provide us with obvious places to look for reconnection

signatures, whereas magnetospheric missions can expect to find reconnection in the magnetotail and the dayside magnetopause.

Current sheets, thin surfaces separating regions of different magnetic field, are often encountered in the solar wind, and strongly sheared fields may be driven together under many circumstances to set up magnetic reconnection. Three major sources of current sheets in the solar wind provide good places to look for reconnection on large scales in the solar wind. The heliospheric current sheet (HCS), which separates the inward and outward-oriented magnetic field in the heliosphere, is one location where reconnection might be reasonably expected to occur. Corotating interaction regions (CIRs) between different solar wind streams typically coincide with thin current sheets that might be ideal places to look for reconnection. Perhaps the most obvious source of potentially reconnecting current sheets, however, is in the sheaths of interplanetary coronal mass ejections (ICMEs). The diversion of the solar wind around a magnetic obstacle like a planet is qualitatively similar to the diversion of solar wind around an ICME. The solar wind field is likely to reconnect with the magnetic cloud field or with itself in the wake of the ICME just as it reconnects on the dayside or nightside of the earth.

It was in the sheath of an ICME that the first direct evidence of reconnection in the solar wind was identified by Gosling et al. [39] with magnetic field and plasma data from ACE. Gosling et al. showed that simple, large-scale reconnection sites in the solar wind could be inferred from their outflow signatures, recorded in situ as these sites pass near observing spacecraft. The characteristic outflow signature is based on Petschek's model for fast reconnection in two dimensions [70, 71]. In this model, reconnection of field lines is localized in the plane of symmetry to a small diffusion region. The size of this region is on the order of the ion gyroradius, $\lambda_{c,i}$. Far from the diffusion region, the outflow, or "exhaust," is bounded on both sides by slow-mode shocks. Across each shock, plasma flowing into the exhaust is accelerated to near the Alfvén speed parallel to the shock front. The diffusion region lies at the intersection of these shock planes, often called the "x-line." In the simplest case, the spacecraft observes a bifurcated current sheet in which the exhaust flow is embedded. As a spacecraft drifts through such an exhaust, two slow-mode transitions are observed separating three distinct regions. First, the upstream region is observed with some inflowing component of the velocity field perpendicular to the reconnecting component of the magnetic field. Second, the exhaust region is observed with accelerated flow along the reconnecting field direction, nearly zero inflow velocity, and near annihilation of the reconnecting magnetic field component. The temperature and density are also higher in this region. Third, the downstream region is observed with inflow and reconnecting field oriented opposite to the upstream region.

Petschek-like exhaust signatures have been found in nearly every solar wind data set, from 0.31 AU with Helios [34] out to 5.4 AU with Ulysses [35]. So called "D-sheets," bifurcated current sheets consistent with reconnection, have also been observed in the heliosheath with Voyager 1 [14]. The timescale for

these exhaust signatures is typically from several seconds to several minutes [35], with structures longer than $\sim$ 10 seconds occurring about once every other day at 1 AU. In some cases, multi-satellite observations have proved to be consistent with Petschek-like x-lines in the solar wind extending for hundreds of earth radii at least [72]. The driving forces behind solar wind reconnection include but are not limited to ICMEs [33], CIRs, and super-radial expansion into the heliospheric current sheet [40]. In the quiescent wind, reconnection seems to occur more often at small shear angles and when the magnetic energy density is large compared to the thermal energy density of the plasma [34, 37]. It has also been hypothesized that small-scale reconnection driven by turbulence could be a significant dissipative process in the solar wind [62]. While many reconnection exhausts have been shown to have slow-mode-like boundaries, it has not been conclusively shown that these boundaries evolve into fully developed slow-mode shocks [35].

At the meeting of the Solar, Heliospheric, and Interplanetary Environment (SHINE) group in June of 2008, a workshop was dedicated to comparative magnetic reconnection. Among the questions addressed in the workshop and in the working group's summary were the following:

- Can a reconnection site be initiated in the solar wind or is it a fossil of coronal structure?
- By what mode do interplanetary current sheets tear?
- Is reconnection spontaneous or must it be driven by large-scale interactions?
- Do Petschek shocks, the theoretical boundaries of purely fluid, steady-state reconnection, occur in nature?
- What is the global energy budget for solar wind heating by reconnection?

In 2006, Gosling et al. made the observation that MR exhausts at the Ulysses apogee, on timescales of minutes, were qualitatively and statistically similar to those at 1 AU [35]. On this basis, one must expect to find MR beyond the Jupiter encounter with Voyager 2. If there is a significant statistical departure beyond 5.4 AU, the Voyager 2 data set contains the plasma record of it. The Voyager 2 results can also be easily calibrated against other spacecraft through the early part of the mission. Assuming data accuracy for the interplanetary magnetic fields to $\sim$0.1 nT, reconnection exhausts with strong field shears could in principle be resolvable in periods of strong magnetic fields as far out as $\sim$ 60 AU.

1.2 Advantageous environments and timescales accessible to Voyager 2

Voyager 2 is unique in that it is the only spacecraft to have provided both thermal ion spectra and magnetic field vectors in the interplanetary medium beyond 5.4 AU. Voyager 2 has enabled us to study the evolution of ICMEs, CIRs, and other solar wind structure far from the sun, at dynamical ages otherwise inaccessible. It can likewise inform the study of reconnection on timescales and spatial scales that no other spacecraft can. The Voyager 2 data sets are the last and most significant untapped resources in the sub-field of solar wind reconnection. To the fullest extent possible, the Voyager 2 data sets should be utilized for this purpose.

While the expansion and rarefaction of the plasma make small-scale features like reconnection exhausts increasingly difficult to discern, there may be advantages to searching for MR at large distances. The steepening of the Parker angle, the angle between the mean magnetic field and the radial direction, is one such advantage. Voyager observations have had a dramatic impact on the science of corotating stream interaction regions, which may be a key driver for magnetic reconnection in the solar wind. In the spiral structure of solar wind wave-fronts, stream interaction regions between opposite magnetic polarities are driven at lower velocity shear at large distances. These velocity shears, when Alfvénic in magnitude, can drive the Kelvin-Helmholtz instability and can suppress current sheet instabilities. At large distances, stream interaction regions with polarity reversals might more closely resemble the simplified 2D structure of Petschek's model. Radial driving flows, as in such interfaces, are also ideal for accurate inflow measurement with the radially-aligned Faraday cup plasma experiment on board Voyager 2.

Furthermore, the trailing and leading edges of CIRs have been shown to typically overlap at heliocentric distances of 5-10 AU. In this regime, CIRs transition from simple two-stream interactions into dynamically rich merged structures[97, 13]. One example of a new structure to evolve in the merged regime is the forward-reverse slow-mode shock pair. To date, these slow shock pairs have been observed only in CIRs, and no closer than $\sim$ 5 AU [44]. So-called Petschek shocks would be examples of this phenomenon, and require the same dynamical timescales to develop. Thus, one might also be better positioned to observe Petschek shocks at large distances from the sun. If Petschek shocks develop after the onset of reconnection, the steady state structure is established on the timescale of L/c_A, where L is the system size. In the solar wind at 1 AU, this timescale is on the order of weeks for a structure of significant angular extent. Whereas the solar wind structure convects at a rate of 1-2 AU/week, MR exhausts at distances of several AU may be much more likely to exhibit Petschek shocks.

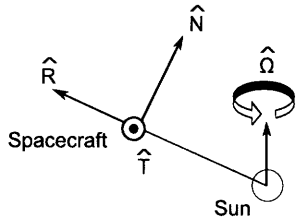

Figure 1.1: The heliographic RTN coordinate system.

1.3 Conventions used

In this thesis, boldface is reserved to signify vector quantities. Unit vectors are denoted by the hat symbol, as in $\hat{\mathbf{x}}$.

The preferred coordinate basis for all spacecraft data is the heliocentric RTN basis, depicted in Figure 1.1, which is used unless explicitly stated otherwise. In that coordinate system, the radial basis vector, $\hat{\mathbf{R}}$, points from the sun to the spacecraft. The tangential basis vector, $\hat{\mathbf{T}}$, is chosen such that $\hat{\mathbf{T}} = \hat{\mathbf{\Omega}} \times \hat{\mathbf{R}}$, where $\hat{\mathbf{\Omega}}$ is the spin axis of the sun. The normal basis vector, $\hat{\mathbf{N}}$, completes the right-handed system. We will also refer to the inclination and orbital angles, θ and ϕ. For a given vector, θ measures deflection out of the RT-plane and ϕ measures the [right-handed] deflection of the in-plane component from $\hat{\mathbf{R}}$.

Equations are given in the centimeter-gram-second (CGS) units system unless otherwise specified. Results and discussion will be framed in units appropriate to the scales in the solar wind, following as closely as possible the conventions in the space sciences literature.

Chapter 2

Theory

2.1 MHD and space plasmas

The solar wind is an excellent example of a collisionless plasma. This means that the system length scales appropriate to the solar wind are much smaller than the mean free path for binary particle collisions. Under typical conditions in the solar wind, a particle will undergo an average of about one binary collision as it travels from the sun's corona to 1 AU. Fluid theories generally rely on collisions to drive the system towards statistical equilibrium, thus assuring that the basic fluid moments like bulk velocity, pressure, and heat flux density are accurate descriptors of the system. Nonetheless, the solar wind is usually well-described by magnetohydrodynamic (MHD) fluid theory.

The solar wind relies on confinement by a strong magnetic field to preserve fluid behavior. In the solar wind, the motion of charged particles across the field is constrained to gyro-orbital motion about the magnetic field. In effect, the field-particle interaction in magnetized collisionless plasmas plays a similar role to collisions in a collisional fluid towards preserving statistical equilibrium. When the energy density of the magnetic field is large compared to the thermal energy of the plasma, magnetic confinement effectively dominates random thermal motion. In lieu of the collisional mean free path, then, the minimum fluid scale in the solar wind is set by the ion gyroradius. The parameter that describes the relative energy density in the plasma, and thus the appropriateness of the fluid approximation in collisionless plasma, is the ion plasma beta:

$$\beta \equiv \frac{p_i}{B^2/8\pi}, \tag{2.1.0.1}$$

where p_i is the [scalar] ion pressure and B is the magnetic field strength. The MHD fluid approximation is generally valid for $\beta \ll 1$. In the solar wind at 1 AU, β may actually vary by several orders of magnitude but is frequently $\lesssim 0.1$.

			1 AU	30 AU
magnetic field strength	$\|B\|$	$\propto R^{-1}$	5 nT	0.2 nT
ion number density	n_i	$\propto R^{-2}$	5 cm^{-3}	0.005 cm^{-3}
bulk speed in the ecliptic	u		400^{+200}_{-100} km/s	
ion thermal speed	w_i	$\propto R^{-0.35}$	50 km/s	10 km/s
Alfvén speed	c_A		50 km/s	
Coulomb collision length	λ_{mfp}	$\propto R^{1.3}$	10^{13} cm	10^{15} cm
ion gyroradius	$\lambda_{c,i}$	$\propto R^{0.65}$	100 km	1000 km
plasma parameter	β	$\propto R^{-0.7}$	$0.1 - 10$	$0.01 - 1$

Table 2.1: Typical values for select properties of the solar wind plasma at 1 AU and 30 AU. Temperature scaling based on empirical expansion rate from Gazis & Lazarus, 1982 [27].

Caution must be used in applying MHD when $\beta \gtrsim 1$, as kinetic effects and non-Maxwellian particle distributions may become important. Some properties of the solar wind plasma are given in Table 2.1.

Because magnetic confinement only applies across the magnetic field, the fluid moments of the plasma are typically anisotropic. Although a host of kinetic modes have been shown to drive thermal isotropy in the solar wind (e.g. [42, 73, 26]), even an anisotropic fluid treatment may not adequately describe the parallel dynamics. The key to fluid behavior in spite of the parallel freedom in collisionless plasmas is that the parallel dynamics operate too slowly to affect the perpendicular dynamics ([23, 68]). The kinetic dynamics of the plasma are mitigated by sound waves, and so perturbations to the plasma propagate and relax along the field at the sound speed. The perpendicular fluid dynamics of the plasma, however, are associated with Alfvén waves. Qualitatively, the MHD fluid approximation remains valid as long as the Alfvén speed, c_A, is much faster than the sound speed, c_s, so that cross-field dynamics proceed much more quickly. This is, in fact, equivalent to the requirement $\beta \ll 1$. It is easily demonstrated that

$$\beta \sim (\frac{c_s}{c_A})^2. \tag{2.1.0.2}$$

The equations of single-fluid, isotropic, weakly-resistive MHD consist of the basic fluid conservation laws, closed by Maxwell's Equations, Ohm's Law, and a polytropic equation of state. Additionally, one considers only the non-relativistic low-frequency, long-wavelength limit. In this limit, the electron inertia is small, so the electron reponse time to any non-zero electric field occurs almost instantaneously[23]. Formally, one lets $m_e \to 0$ and $c \to \infty$ where m_e is

the electron mass and c is the speed of light. The equations are repeated below for reference in Gaussian (cgs) units. In the following, we use $\mathbf{E}$, $\mathbf{B}$, and $\mathbf{J}$ to denote the electric field, magnetic field, and current density, respectively. The fluid moments are the number density, n, the bulk velocity u, and the isotropic scalar pressure p. We use ρ to denote charge density. The polytropic index, γ, is typically $\sim 5/3$ in a Maxwellian plasma [68]. The effective mass, m_0 is approximately equal to the proton mass, $m_p \approx 1.67 \cdot 10^{-24}$g, in the solar wind. These conventions will be followed elsewhere unless explicitly stated.

- The continuity equation:

$$\frac{\partial}{\partial t} n + \nabla \cdot (n\mathbf{u}) = 0 \tag{2.1.0.3}$$

- The momentum equation:

$$m_0 n(\frac{\partial}{\partial t}\mathbf{u} + \mathbf{u} \cdot \nabla \mathbf{u}) + \nabla p - \frac{1}{c}\mathbf{J} \times \mathbf{B} = 0 \tag{2.1.0.4}$$

- Ohm's Law:

$$\mathbf{J} = \sigma(\mathbf{E} + \frac{\mathbf{u}}{c} \times \mathbf{B}) \tag{2.1.0.5}$$

- Ampere's Law (neglecting the displacement current):

$$\nabla \times \mathbf{B} = \frac{4\pi}{c}\mathbf{J} \tag{2.1.0.6}$$

- Faraday's Law:

$$\nabla \times \mathbf{E} = -\frac{1}{c}\frac{\partial \mathbf{B}}{\partial t} \tag{2.1.0.7}$$

- Gauss's Law:

$$\frac{1}{4\pi\rho}\nabla \cdot \mathbf{E} \ll 1 \tag{2.1.0.8}$$

- No magnetic monopoles:

$$\nabla \cdot \mathbf{B} = 0 \tag{2.1.0.9}$$

- Equation of State:

$$\frac{d}{dt}(pn^{\gamma}) = 0 \tag{2.1.0.10}$$

In ideal MHD, the conductivity, σ, is taken to be infinite. In this limit, the steady-state current density in the plasma, $\mathbf{J}$, is only finite if $\mathbf{E} = -\frac{\mathbf{u}}{c} \times \mathbf{B}$. By substituting for $\mathbf{E}$ into equation 2.1.0.7, one obtains the ideal induction equation:

$$\frac{\partial \mathbf{B}}{\partial t} = \nabla \times \mathbf{u} \times \mathbf{B}. \tag{2.1.0.11}$$

2.2 Magnetic Reconnection

There is some debate in the field of plasma physics about how to rigorously define magnetic reconnection [75]. In ideal MHD, however, the concept is highly intuitive: reconnection is a process that changes the field-line topology of the plasma.

Magnetic field lines are curves that are tangent to the magnetic field at every point. Because the magnetic field and fluid move together as one in ideal MHD, a field line and the filament of plasma it penetrates may be thought of as a physical object whose identity is preserved over the convection and deformation of the flow, as long as the field is nonzero. Such an object or a contiguous group of such objects is often called a "flux tube." Ideal MHD plasmas are often heuristically described as a continuum of deformable elastic tubes, each having a radius of approximately $\lambda_{c,i}$.

It is easily shown that plasma in a given flux tube is perfectly confined to it provided that the plasma is a perfect conductor. This is often called the "frozen-in" law because the magnetic flux is trapped, or "frozen," into the fluid. Consider an arbitrary flux tube cross section, S. We can show that the invariance of magnetic flux through S over deformation by the flow follows directly from the ideal MHD equations.

Consider the flux of $\mathbf{B}$ through a surface element, S, over time. Let S be bounded by the curve l. The flux through S is given by

$$\Phi_B = \int_l \mathbf{B} \cdot \mathbf{dS}.$$

The change in this flux can be thought of in two parts. First is the change in flux through S due to changing $\mathbf{B}$. Second is the change in flux through S due to the deformation of S (illustration). The new area swept out by a differential segment of the boundary, l, is equal to $\mathbf{u} \times \mathbf{dl}$. Thus the total rate of change of the flux is

$$\frac{d\Phi_B}{dt} = \underbrace{\int \frac{\partial \mathbf{B}}{\partial t} \cdot \mathbf{dS}}_{\text{due to change in B}} + \underbrace{\oint \mathbf{B} \cdot (\mathbf{u} \times \mathbf{dl})}_{\text{flux through change in area swept out by flow}} . \quad (2.2.0.12)$$

Making use of the vector identity $A \cdot (B \times C) = -C \cdot (B \times A)$, the second part of the equation can be rewritten

$$\oint \mathbf{B} \cdot (\mathbf{u} \times \mathbf{dl}) = -\oint \mathbf{dl} \cdot (\mathbf{u} \times \mathbf{B}).$$

Using Stokes' Theorem, this can be re-expressed as a surface integral

$$-\oint \mathbf{dl} \cdot (\mathbf{u} \times \mathbf{B}) = \int \mathbf{dS} \cdot (\nabla \times \mathbf{u} \times \mathbf{B}),$$

and substituting this back into equation 2.2.0.12, one finds that the change in flux through S is given by

$$\frac{d\Phi_B}{dt} = \int \mathbf{dS} \cdot (\frac{\partial \mathbf{B}}{\partial t} - \nabla \times \mathbf{u} \times \mathbf{B}). \tag{2.2.0.13}$$

The integrand of equation 2.2.0.13 is an expression of the convection of the magnetic field in an ideal MHD plasma. According to the ideal induction equation (eq 2.1.0.11), the integrand is identically equal to zero when conductivity is perfect. Thus the magnetic flux through S does not change. We can define the flux tube of which S is a cross section as the solid swept out by parallel transport of S along the field, i.e. $S' \rightarrow S + \triangle$ where $\triangle \times \mathbf{B} = 0$. By construction, any such cross-sectional surface S' encloses the same magnetic flux as S. The "frozen-in law" demonstration above is repeatable for the evolution of all cross sections S' in time, thus any field line intersecting S is fully contained in the flux tube at all times.

Flux tubes are intuitive constructs in MHD plasmas. They are a simple physical representation of the degrees of freedom and the stresses at work in the fluid. Particles are confined perpendicular to the flux tube and free to travel along it unencumbered. Changes in the magnetic tension and pressure acting on the plasma are manifested as changes in flux tube curvature and diameter, respectively. Flux tubes may also be thought of as wave guides. Because the group velocity of the shear Alfvén wave is parallel to the local magnetic field, an Alfvénic perturbation will always propagate along the length of flux tube.

Magnetic reconnection is the most basic violation of the flux tube heuristic, and perhaps the most fundamental correction to an ideal MHD model of any physical system. Magnetic reconnection is any process that changes the flux-tube topology of the plasma.

In ideal MHD, the uniqueness of magnetic field lines, i.e. trajectories of parallel transport, in the plasma may break down when the magnetic field is zero. The tangent to a field line s, obeying the equation $\mathbf{ds} \times \mathbf{B} = 0$, can be multi-valued when $\mathbf{B} = 0$ or when $\mathbf{B}$ is discontinuous. As a result, a flux tube convected across a magnetic null or discontinuity admits branching that is dependent on the field geometry. Flux tubes may intersect pairwise and connect or disconnect across a magnetic null or discontinuity, providing a new degree of freedom for parallel transport. Heuristically, magnetic reconnection may be thought of as a joining of two distinct flux tubes, followed by a disconnection that severs the original connectivity of each segment while preserving the new connectivity (see Figure 2.1). The locus at which pairs of field lines intersect is often called the *x-point*. The mapping of conjoined field lines at the moment of connection is called the *separatrix*. The separatrix is the topological boundary between the initial field line geometry and the reconnected field line geometry.

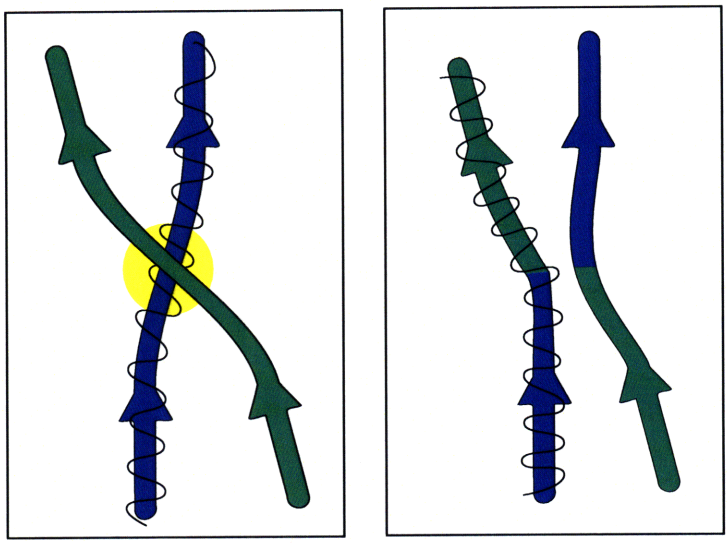

Figure 2.1: A heuristic illustration of magnetic reconnection. Flux tubes are represented by the green and blue bars. The black path shows a hypothetical test particle trajectory before and after the flux tubes reconnect.

2.2.1 Non-idealness in reconnection: failure of the heuristic model

In the previous section, a heuristic picture of magnetic reconnection was presented in the framework of ideal MHD. While this heuristic is intuitive, it is misleading in that it involves several built-in violations of that framework. To address those violations and physically model the analogous process, the non-idealness of the plasma must be considered. In this section, we will discuss the treatment of MHD violations and give a more physically appropriate and general definition for magnetic reconnection.

First, we note that the validity of MHD is predicated on the condition $\beta \ll 1$. In the absence of collisions, the kinetic scale for an MHD plasma is established by the gyro-motion of ions and electrons in the magnetic field. Near a magnetic null, however, particles are not gyrotropically confined. In the region around the null where the ion thermal energy density, $\frac{1}{2}m_i w_i^2$, is comparable to the magnetic energy density, $B^2/8\pi$, the particles and the field become decoupled and flux tube is no longer physically valid. MHD is invalid in this region and a kinetic theory must be used. The ion-gyroradius, $\lambda_{c,i}$, which scales as $\beta^{-1/2}$, is a useful and intuitive parameter for the scale of this non-ideal region. Any point in space is considered non-ideal if a magnetic null or discontinuity is physically removed from it by a distance $\lesssim \lambda_{c,i}$.

A similar exception arises for any plasma configuration involving gra-

dients on scales comparable to the ion gyro-radius, $\lambda_{c,i}$. If the reconnection involves significant deflection of magnetic field lines, a field gradient scale on the order of $\lambda_{c,i}$ is typically created. This is another consequence of reconnection that is made obvious by the flux tube picture. To see why it is so, consider the joining of two unitary flux tubes ($r = \lambda_{c,i}$) carrying magnetic fields $B_0\hat{\mathbf{b_1}}$ and $B_0\hat{\mathbf{b_2}}$ that intersect at an angle θ. Without regard for the structure in the non-ideal region, we may continue to use the flux tube picture just beyond it to give an lower bound for the gradient of the antiparallel component of the field. Across the non-ideal region, the change in the field is just the difference between the frozen-in fields $\triangle B = 2B_0 \sin\frac{\theta}{2}$. Giving the non-ideal region a berth of $2\lambda_{c,i}$, the typical field gradient is $|\nabla \mathbf{B}| \sim B_0 \sin\frac{\theta}{2}/\lambda_{c,i}$. In the special case of merging anti-parallel fields, the system scale is automatically equal to $\lambda_{c,i}$.

In the previous section, we defined magnetic reconnection as a process that changes the field-line topology of a plasma. Field line permanence and MHD describe the behavior of space plasmas well when sufficiently removed from the non-ideal regions described here. Because a fully kinetic treatment of almost any problem in space physics is computationally intractable, the best approach to the reconnection problem is a hybrid of MHD and kinetic theory/corrections. Because the violations are localized, the topological definition is still correct with respect to MHD if we include the caveat that the actual process at work is not an MHD one. A similar definition was offered by Hesse and Schindler in a discussion of general magnetic reconnection theory[43]. They also defined it from the MHD perspective as "a breakdown of magnetic connection due to non-idealness."

The MHD theory is often adjusted to allow for magnetic reconnection by breaking with the ideal Ohm's Law (2.1.0.11), but only in the neighborhood of field line intersections. Including a finite resistivity, the general Ohm's Law becomes

$$\mathbf{E} + \frac{\mathbf{u}}{c} \times \mathbf{B} = \mathbf{R} \tag{2.2.1.1}$$

where $\mathbf{R}$ is a correction to the electric field that may model any number of non-MHD effects such as conduction by collisions, separation of charge due to particle inertia, and kinetic modes. $\mathbf{R}$ is taken to be nonzero in the neighborhood of the field line intersection and identically equal to zero elsewhere. Recall that $\mathbf{E}$ and $\mathbf{B}$ refer to the fields as measured in a general laboratory frame. The ideal Ohm's Law states that there is no net electric field in a frame co-moving with the plasma. In the vicinity of non-zero $\mathbf{R}$, however, a net electric field is admitted in the plasma frame. Non-zero $\mathbf{R}$ also implies a resistivity in the plasma if the resulting current is to be finite. Because such a resistivity violates the frozen-in law and allows the plasma to diffuse across field lines, the non-ideal region is often called the *diffusion region.*

To treat field-line identity in a mathematically concrete way, the magnetic field can be expressed in terms of Euler potentials.

$$\mathbf{B} = \nabla\alpha \times \nabla\beta \tag{2.2.1.2}$$

This form for the magnetic field admits no divergence by construction, and has the added property that $\nabla\alpha$ and $\nabla\beta$ are perpendicular to the field, implying that the potentials α and β are constant along field lines. In this way, the values of the Euler potentials can be thought of as a labels that uniquely specify particular field lines. The functions also specify the vector potential of the field, $\mathbf{A} = \alpha\nabla\beta$ in the gauge where $\mathbf{A} \times \mathbf{B} = 0$. In an elegant formulation of the reconnection problem, it was shown by Hesse and Schindler that a necessary and sufficient criterion for a field line with potentials (α,β) to re-emerge from the non-ideal region transit connected to a new field line (α',β'), is that the non-ideal component of the electric field, $\mathbf{R}$, must satisfy

$$\int_{-\infty}^{\infty} \mathbf{R} \cdot \mathbf{ds} \neq 0 \tag{2.2.1.3}$$

where the integral is carried out along a field line connected to the non-ideal region. When reconnection occurs, a net electrical potential exists along the field. In terms of the Euler potentials, the breakdown of field line permanence in the presence of a parallel electric field is reflected as a change in the functions (α,β) . Outside of the non-ideal region, where the potentials are preserved, the field lines maintain their identities.

Equation 2.2.1.3 serves as a rigorous, though perhaps unintuitive, definition of general magnetic reconnection. Its application for *in situ* spacecraft observations, however, is very limited. In order to measure $\mathbf{R}$ directly, a spacecraft must cross through the diffusion region itself. The scale of the diffusion region is presumably a very small fraction of the system scale, so these encounters are expected to be rare [89, 91]. The nature of the parallel electric field is a subject of ongoing research, particularly in laboratory plasmas [100]. One potential source is the Hall effect, wherein a parallel electric field is created by the inertial decoupling of ions and electrons as they are deflected in the diffusion region [76]. For the purposes of this thesis, the magnetic field topology will generally be inferred from likely symmetries and observations far from the diffusion region. The Hall effect is not a significant consideration in that regime.

2.2.2 Two-dimensional models and their applicability to space plasmas

Because a spacecraft time series can offer only a one-dimensional cross section of any three-dimensional solar wind structure that may be evolving in time, the amount of geometrical and topological complexity that can be observed and modeled with any confidence is extremely limited. Fortunately, the processes that establish boundary conditions for magnetic reconnection in the solar wind, particularly the interfaces between strongly sheered magnetic fields, often have a

high degree of symmetry on appropriate scales. Magnetic sectors are frequently observed in the solar wind, probably in direct correspondence with magnetic sectors on the sun, wherein the magnetic fields are roughly homogeneous [6]. Distinct sector structure in the solar wind, particularly near solar minimum, often takes on large angular scales[15]. Reconnection across magnetic sector boundaries may be one scenario, then, where a quasi-2D model could give a great deal of physical insight. These magnetic sector boundaries are called *current sheets*, because the field shear is accompanied by a current density along the boundary surface according to Ampere's Law (Equation 2.1.0.6). Other large-scale systems with smooth magnetic field structure, such as the sheaths of coronal mass ejections and the heliospheric current sheet, can also be slab symmetric on scales that are much larger than the kinetic scale length, $\lambda_{c,i}$, and might be well-approximated in two dimensions. Whenever 2D models are compared to actual observations, of course, great care must be taken to assure that sufficiently symmetric conditions exist, and that the observations are fully consistent with that symmetry.

It is convenient to establish a frame of reference that takes advantage of slab symmetry when available. In the region where two reconnecting flux tubes intersect, we define the *reconnection plane* as the plane that is tangent to the field lines at the point of intersection. In the case of two uniform magnetic sectors merging across a shared planar boundary, the system is invariant over translations perpendicular to the reconnection plane. Tractable problems in magnetic reconnection generally begin by solving the two-dimensional problem in the reconnection plane as a point of departure. As long as the magnetic fields and flows can be treated as uniform over a length scale that is significantly larger than the kinetic length scale, this is a valid approach for MHD plasmas.

We will proceed, then, to introduce two of the most general steady-state models of magnetic reconnection in two dimensions. For simplicity, these models will both assume two uniform regions of anti-parallel magnetic flux that are separated by a planar boundary. Both of these models assume that perfectly MHD behavior is only violated in a non-ideal region that is local to the boundary.

2.2.3 The Sweet-Parker Mechanism

For a reconnection model to successfully predict the behavior of the MHD system, one issue that must be addressed is the rate at which reconnection can occur. Sweet [92]and Parker [66, 67] offered a simple dimensional model of steady-state anti-parallel field merging that is mitigated by Ohmic diffusion. Presented here in a simple rectangular geometry, the Sweet-Parker mechanism has been explored in other related configurations with similar results and limitations [75].

Let anti-parallel flux be brought together in the non-ideal region at the diffusion speed, as dictated by the resistive MHD induction equation

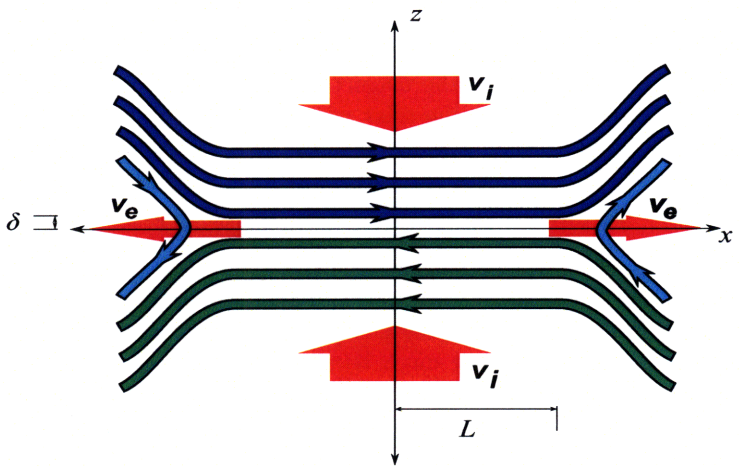

Figure 2.2: Schematic of a Sweet-Parker current sheet.

$$\frac{\partial \mathbf{B}}{\partial t} = \nabla \times (\mathbf{u} \times \mathbf{B}) + \eta \nabla^2 \mathbf{B}, \tag{2.2.3.1}$$

where the magnetic diffusivity, η, is related to the ohmic conductivity by $\eta = \frac{c^2}{4\pi\sigma}$. The timescale for magnetic diffusion along a gradient $\nabla \sim 1/\delta$ is given by

$$\tau_d = \delta^2/\eta. \tag{2.2.3.2}$$

For steady-state magnetic reconnection, this is the timescale on which convected flux can be admitted into the diffusion region.

In the Sweet-Parker model, we assume that the field configuration is symmetric along the magnetic field direction, $\hat{x}$, over some fluid length scale, $2L$ centered at the origin. Let the diffusion region have a length scale 2δ in the cross-field direction, $\hat{z}$, such that the current sheet and magnetic null sheet lie in the xy-plane (see Figure 2.2). To maintain a steady-state, the inflow speed into the diffusion region must be equal to the diffusion speed inside of it.

$$v_i = v_d \approx \delta/\tau_d \tag{2.2.3.3}$$

This diffusion allows the magnetic field to slip through the plasma and reconnect without forcing the plasma into the current sheet. Instead, the plasma is allowed to flow out of the diffusion region in the $\pm\hat{x}$ direction in a stream of width $\sim \delta$. This outflow is often called the ***exhaust jet*** and will be denoted by v_e here and elsewhere. The flow into the diffusion region along $\pm\hat{z}$ and out along $\pm\hat{x}$ contains a stagnation point at the origin. In the incompressible limit with density a constant n_d, the conservation of mass requires that the plasma influx, $4n_dLv_i$, be offset by the out-flux, $4n_d\delta v_e$. Similarly, because magnetic flux is conserved

outside of the diffusion region, it is required that the inflow of magnetic flux, proportional to $v_i B_i$ is offset by the outflow of magnetic flux in the exhaust, $v_e B_e$. These conservation laws together imply the following scalings:

$$L v_i \approx \delta v_e \tag{2.2.3.4}$$

$$\frac{B_i}{L} \approx \frac{B_e}{\delta}. \tag{2.2.3.5}$$

The force equation along the sheet can also be estimated, again by scaling $\nabla \sim 1/\delta$ across the diffusion region in the $\hat{z}$ direction and $\nabla \sim 1/L$ in the $\hat{x}$ direction, in order to estimate the exhaust speed. For a low beta plasma, we neglect the pressure gradient force in favor of the Lorentz force, leaving

$$m_0 n(\mathbf{u} \cdot \nabla) u_x \approx m_0 n \frac{v_e^2}{L} = \frac{1}{c} J_y B_e. \tag{2.2.3.6}$$

The current density, $\mathbf{J}$, is given by Ampere's Law, $\mathbf{J} = \frac{c}{4\pi} \nabla \times \mathbf{B}$. In the diffusion region, the current scales as

$$\mathbf{J} \approx \frac{c}{4\pi} \frac{B_i}{\delta} \hat{\mathbf{y}}. \tag{2.2.3.7}$$

Combining equations 2.2.3.5, 2.2.3.6, and 2.2.3.7, Sweet and Parker showed that the typical reconnection exhaust speed in this limit is Alfvénic.

$$m_0 n \frac{v_e^2}{L} \approx \frac{1}{4\pi} \frac{B_i B_e}{\delta}$$

so

$$v_e \approx \frac{B_i}{\sqrt{4\pi m_0 n}} \equiv c_A. \tag{2.2.3.8}$$

The reconnected magnetic field exerts a force that accelerates the outflowing plasma to the [external] Alfvén speed.

The Sweet-Parker prescription assumes that the magnetic diffusion layer spans the full boundary between regions of opposing magnetic field. The diffusion region length scale is taken to be comparable to the global system size. The separation of scales required by MHD is that any macroscopic system has length scale $L \gg \delta$, whereas the width of the diffusion layer is no smaller than $\lambda_{c,i}$. This separation of scales places strong limitations on the rate at which magnetic flux can be transported in the Sweet-Parker model. It is useful to parametrize the rate of reconnection rate in terms of the magnetic Reynolds number of the system. The magnetic Reynolds number (also called the Lundquist number) is given by:

$$R_m = \frac{L c_A}{\eta}. \tag{2.2.3.9}$$

The rate of reconnection can then be written in terms of global parameters as

$$v_i = \frac{c_A}{\sqrt{R_m}}, \tag{2.2.3.10}$$

where all parameters are calculated outside of the diffusion region and exhaust flow. A dimensionless measure of the reconnection rate is given by the Alfvén Mach number of the inflow, $M_i = R_m^{-1/2}$.

The inadequacy of the Sweet-Parker mechanism for space plasmas becomes quickly obvious when we consider the typical magnetic Reynold's numbers involved. In the solar wind, the terrestrial magnetosphere, and the sun's corona, the magnetic Reynold's number is typically $R_m \sim 10^{12} - 10^{16}$ [75]. The inflow Mach number required for disconnection of solar flares on the observed timescale of a few hours is between $M \sim 10^{-3}$ and $M \sim 10^{-6}$. A Sweet-Parker-like solar flare, however, would take months to erupt. The Alfvén Mach number of the slow solar wind at 1 AU, on the other hand, typically varies from $M \sim 5$ to $M \sim 25$ and may change by as much as an order of magnitude across a current sheet [68]. A Sweet-Parker-like inflow in the solar wind would be on the order of a few centimeters per second, which is both immeasurably small and an impossibly fine steady-state speed when compared to pervasive turbulent perturbations. As the magnetic Reynold's number decreases with distance from the sun, the inflow speed remains below the measurement resolution of any spacecraft even to just before the heliopause, where $R_m \sim 10^7$. The Sweet-Parker mechanism is also ruled out in solar wind physics by the lack of direct observations: because the Sweet-Parker diffusion surfaces would span the full boundaries of reconnecting magnetic sectors, they would be frequently traversed and measured *in situ* by spacecraft. To date, even circumstantial evidence of spacecraft encounters with such non-ideal regions is rare [78].

The Sweet-Parker mechanism is many orders of magnitude too slow to explain the reconfiguration of these magnetic fields in nature. Indeed, it is generally referred to as "slow reconnection," whereas processes with inflows faster than the Sweet-Parker rate are referred to as "fast reconnection." The basic physical insights, however, seem sound. For reconnection to occur in an ideal, or at least pseudo-ideal MHD system, the non-ideal behavior must certainly be localized. The exhaust mechanism also ought to be Alfvénic, energized by the conversion of magnetic energy. The reconnection of anti-parallel fields obviously creates a tightly-kinked configuration at the exhaust which must relax self-consistently. In order to produce faster rates reconnection rates, the original Sweet-Parker model requires an additional insight. By decreasing the system size, L, the magnetic Reynolds number of the system can be reduced and the Sweet-Parker mechanism might be salvaged. The implication of this insight is that steady-state reconnection must develop substructure beyond the uniform current sheet of Figure 2.2.

2.2.4 Fast Reconnection and the Petschek Mechanism

In the Sweet-Parker model, the system size L was taken to be the length of the diffusion region, the current sheet, and the length scale on which $\mathbf{B_i}$ is constant and parallel to the current sheet. The diversion of the plasma flow itself was attributed to the Lorentz force in the diffusion region. While we maintain that the plasma must obey the laws of ideal MHD outside of the diffusion region, there is no *a priori* requirement that translational symmetry must exist over the full length of the system, nor that the diffusion region must span the system. The only requirement for reconnecting field lines is that they pass through the diffusion region somewhere along their length. For fast reconnection to take place, the effective magnetic Reynolds number must be lower, which implies that the scale of the region in which reconnection actually occurs is much smaller than the system scale.

In the Petschek model, reconnection perturbs the flow and magnetic field geometry near the diffusion region (Petschek, 1968). The magnetic field is permitted to have a small $\hat{\mathbf{z}}$ component such that opposing field lines intersect in an X-like configuration at a small region l, rather than merging along the entire system length L in a sheet-like configuration (see Figure 2.3).

Because most of the plasma never passes through the diffusion region in this new picture, it must be diverted elsewhere. Petschek realized that the exhaust acceleration, ohmic heating, and reconfiguration of the field in the Sweet-Parker mechanism could qualitatively be accomplished by a pair of slow-mode MHD shocks extending from the diffusion region. Slow-mode shocks have the following useful properties:

1. Magnetic pressure and kinetic pressure are anti-correlated. Across the shock, the magnetic field decreases and the kinetic energy of the flow increases.

2. The magnetic field vector is deflected towards the shock normal. In the Petschek configuration, this rotates the initially anti-parallel $\pm\hat{\mathbf{x}}$-oriented fields to become parallel along $\hat{\mathbf{z}}$.

3. The flow normal to the shock is slowed. The normal component of $\mathbf{v_i}$ transitions from super-magnetosonic to sub-magnetosonic across the shock with respect to the slow-wave speed.

4. In the limit that the shock normal is perpendicular to $\mathbf{B_i}$, $\mathbf{B_e}$ goes to zero and the [exhaust] flow along the shock surface is accelerated to the Alfvén speed.

The Petschek model introduces four shock fronts extending along the separatrix of the system, as shown in Figure 2.3). Across these shocks, which are represented in the figure with thick black lines, the inflow is converted to an

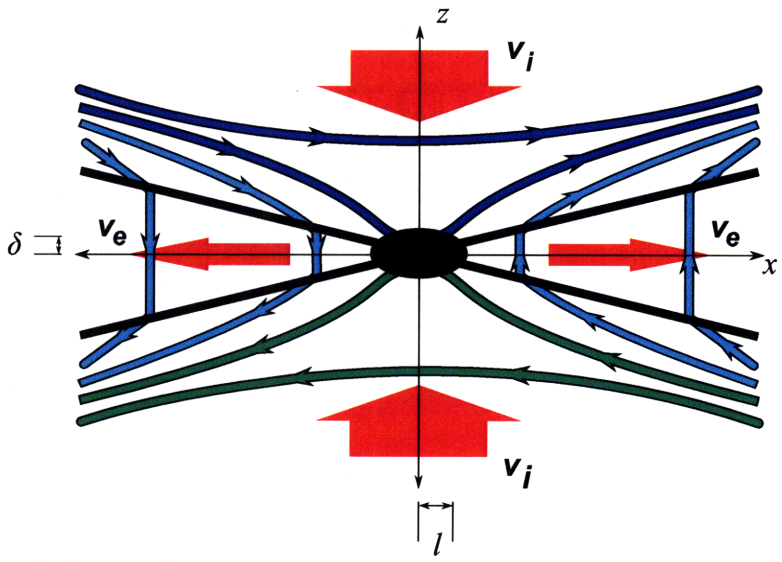

Figure 2.3: Schematic of a Petschek current sheet.

exhaust flow that is qualitatively similar to the Sweet-Parker exhaust flow. The magnetic field in the exhaust is $\pm\hat{\mathbf{z}}$-oriented, and kinked at the shock surface. These kinks propagate as Alfvén waves away from the x-point self-consistently, sweeping up the exhaust plasma to near Alfvén speed. In the inflow, the magnetic field is perturbed so as to align nearly tangentially with the shock. The inflowing magnetic field lines are thus bent so as intersect at a point rather than along the whole system length.

While Petschek's model uses the same implicit boundary conditions as that of Sweet and Parker, it admits an arbitrarily high reconnection rate because the slow-mode shock surfaces bend so as to intersect at an arbitrarily small diffusion region. The shocks, which mark the boundary between the inflow region and the *exhaust cone* region, essentially do all of the work necessary to minimize the necessary amount of diffusion. While the Sweet-Parker model diffusion region had an imposed scale set by the size of the current sheet, the Petschek model diffusion region scale is a free parameter, so long as $l \gtrsim \lambda_{c,i}$. Indeed, numerical experiments have shown that in a Sweet-Parker configuration where driving is increased to $v_i > v_d$, a Petschek transition occurs wherein the diffusion region contracts until a compatible magnetic Reynolds number is achieved [7, 102, 16]. At this transition, slow standing shocks are formed on Alfvén wave crossing timescale of the system, propagating outward from the diffusion region. It should be noted, however, that these simulations generally involve an artificially increased cross-field resistivity in the non-ideal region. While physically plausible sources of enhanced resistivity beyond the collisional Spitzer value abound, particularly due to inertial and wave-particle effects, increasing the re-

sistivity *ad hoc* a is controversial approach. A complete theory of resistivity in the diffusion region has yet to be fully-developed or accepted. Laboratory experiments designed to measure the effective resistivity in the weakly collisional regime have measured significant enhancements over the Spitzer value [99].

In Petschek's model, the allowable rate of reconnection scales more weakly with the global magnetic Reynolds number, $R_m = \frac{Lc_A}{\eta}$ because the field strength at the diffusion region and the size of the diffusion region are reduced. The new reconnecting field, $\mathbf{B_i'}$, is the sum of the original external field $\mathbf{B_i} = B_i\hat{\mathbf{x}}$, and the perturbation $\tilde{\mathbf{B}}$ at the new diffusion region. To be self-consistent with the original boundary conditions, the perturbation must go to zero at large distances ($\sim L$) from the diffusion region such that $\mathbf{B_i'} \rightarrow \mathbf{B_i}$. The perturbation also must be consistent with the exhaust field $\tilde{\mathbf{B}} = B_e\hat{\mathbf{z}}$ along the current sheet on the range $l < x < L$ to accommodate the magnetosonic transition. Petschek showed that for any such perturbation that solves the Laplace equation for these boundary conditions, the diffusion region inflow field is given by

$$B_i' = B_i(1 - \frac{4M_i}{\pi}\log\frac{L}{l}). \tag{2.2.4.1}$$

The corresponding rate of flux transport into the diffusion region, i.e. the reconnection rate, is thus also attenuated by the factor $1 - \frac{4M_i}{\pi}\log\frac{L}{l}$. Petschek estimated a maximum rate of magnetic reconnection for this process corresponding to a loose perturbation bound $\tilde{B} \lesssim B_i$. The maximum inflow Mach number allowed was shown to be

$$M_i \lesssim \frac{\pi}{8\log R_m}. \tag{2.2.4.2}$$

This rate is well-suited to reconnection in the solar wind, as it allows for inflow Mach numbers in the range of a few km/s. A Petschek reconnection inflow such as this could be accurately measured under most circumstances. It can also be shown from the Sweet-Parker scalings (Eq 2.2.3.4-2.2.3.5) that the new diffusion region scales like

$$\frac{l}{L} \approx \frac{1}{R_m M_i^2}. \tag{2.2.4.3}$$

For a measurable inflow in the solar wind, then, with $M_i \gtrsim 0.01$, the scale of diffusion region would typically be smaller than the associated current sheet by a factor of $\sim 10^{-8}$. Clearly, *in situ* observations of the diffusion region in Petschek reconnection should be extremely rare.

2.2.5 Petschek shocks in the laboratory and in nature

The Petschek model provides a unique set of observable features for space research. Because the slow wave speed is arbitrarily slow in the for perpendicular

shocks, however, the unambiguous identification of a slow-mode shock in the solar wind presents a significant challenge. Positive identifications of slow-mode shock fronts in the solar wind have been described by Ho et al. [45, 44], Richter [79], Chao and Olbert [17], and Burlaga and Chao [10] but in the absence of traditional "smoking gun" indicators such as distinct non-thermal shock-heated particle populations. These observations have also generally failed to localize the shock transition to kinetic scales.

The variability and detailed magnetic structure of the solar wind suggest a strong need for a robust and ubiquitous fast reconnection process. If that process is Petschek's mechanism then slow shocks should be found in forward-reverse shock pairs. To date, one such observational claim has been made, though not necessarily in conjunction with magnetic reconnection [44].

The observation of slow-mode shocks in laboratory plasmas also presents a significant challenge. While many laboratory experiments are well-suited to studying the ion diffusion region itself, they are generally inadequate for studying the large-scale reorganization of a collisionless system. Steady state, collisionless reconnection in a laboratory plasma requires experiments with large mean free paths, on scales that are much larger than the ion gyroradius, and large enough to simulate an open boundary condition for the exhaust flow. Most reconnection experiments operate on timescales that are significantly longer than the Alfvén crossing time of the vessel, so the closed boundaries tend to play a large role in the reconnection process [75]. Kinetic instabilities due to edge effects also tend to develop on timescales comparable to the hypothetical shock formation timescale. The size of the Princeton Magnetic Reconnection Experiment, for example, is between a few to ten ion gyroradii and several times the collisional mean free path. Charge separation and collisions play an important role both in the diffusion region and at any hypothetical slow shock surfaces [101]. Perhaps it is to be expected, then, that few modern laboratory experiments have claimed detection of slow-mode shocks or Petschek reconnection[1].

2.2.6 Unsteady current sheets

While a steady-state, stationary fast reconnection solution is attractive for its simplicity, plasma flows with large magnetic Reynolds numbers tend to evolve rapidly towards a turbulent state. Empirically, the quiescent solar wind observed at any given time may be classified as belonging to one of two states [29]. Each of these states is strongly turbulent, typically exhibiting a power-law relationship between the strength and scale of fluctuations. The two states are the fast wind, associated with open-field regions on the sun, and the slow wind, associated with

[1]Claims of Petschek shock detection were published by the Double Inverse-Pinch Device (DIPD) experimental team in 1970 [8]. These claims have not generally been accepted, however, due to difficulties associated with accurate magnetic field measurement and difficulty establishing the symmetry of the plasma configuration in the device.

closed-field regions. Figure 2.4 illustrates one example of the turbulent states on either side of a transition from slow to fast wind in the ecliptic at 1 AU.

It has been convincingly demonstrated that the fast wind originates from coronal holes (i.e. [28]). This wind state is sometimes observed in the ecliptic for flows from low latitude extensions of the polar coronal hole or from sunspots. Fast solar wind is associated with strong Alfvénic (non-compressive) turbulence. In-depth studies of fast wind in the ecliptic at 1 AU and extensions to greater distances and wider heliolatitudes with Ulysses and Voyager 2 have demonstrated that ongoing fluctuations of order $dB/|B| \sim 0.01$ to 0.1 and greater are typical on all timescales of interest to this thesis, from seconds to hours. For some periods, particularly at high plasma-β, the mean fluctuation amplitude approaches $dB/|B| \sim 1$, indicating a fully chaotic flow structure. No current sheet can be expected to be symmetric to beyond the order of these fluctuations. In the fully developed case, the magnetic field is completely fractionated and has no ongoing symmetry except in the statistical sense. Reconnection occurs between turbulent cells in the plasma, or ***plasmoids***, which are the MHD analogue of eddies in hydrodynamic fluids[80, 29].

In the slow solar wind, fluctuations are driven at low frequencies by the interaction of plasma streams from the sun and by eruptive events. These fluctuations couple continuously to higher frequencies in a turbulent cascade that appears to permeate the plasma at all times. Fluctuations at all frequencies from hours down to seconds typically exhibit a power law in this state. Fluctuations on short timescales are somewhat weaker and more compressive in the slow wind than they are in the fast wind.

Numerical studies such as [85], [52, 64], and [21] have demonstrated that the global reconnection rate of a current sheet system increases in the presence of strong turbulence. The effect of turbulence on the current sheet is illustrated in Figure 2.5. In the fully developed limit, diffusion takes place across thin Sweet-Parker current sheets between plasmoids, rather than across the mean field. Assuming that current sheets form efficiently on all scales, the appropriate diffusion velocity is based on the eddy-turnover rate instead of the collision rate, and is therefor scale-dependent [53].

$$v_d \approx \delta v_{eddy} \cdot \frac{\lambda_{eddy}}{L}. \tag{2.2.6.1}$$

The cumulative reconnection rate for a current sheet with stochastic substructure depends on the spectral index of the eddy distribution and the total wave amplitude therein. In terms of the wave amplitude at the global scale, δv_L and the spectral index, χ, the stochastic component of the reconnection rate can be estimated by

$$M_i \sim \frac{1}{c_A} \int_{\lambda_i}^{L} \delta v_L \cdot (\frac{\lambda}{L})^{-\chi+1} d\lambda. \tag{2.2.6.2}$$

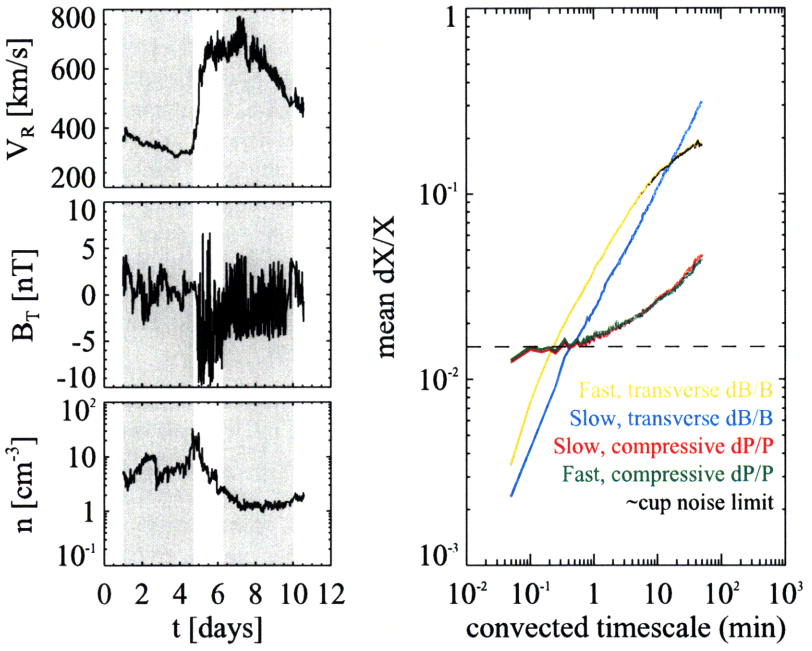

Figure 2.4: At left, the velocity, magnetic field, and density of the solar wind as measured by Wind crossing a coronal hole boundary layer. At right, the fluctuation spectrum is shown for the highlighted slow and fast streams. The slow solar wind, which is most abundant at low latitudes near solar minimum, is observed continuously until days 4-5, when the transition to fast wind takes place. Over the ensuing period, fast wind from a low-latitude coronal hole is observed. The transition region is associated with plasma originating at the low-latitude coronal hole boundary layer, along with some mixture of the two colliding streams.
Characteristics of the slow wind are stronger variability at the largest scales and a power law spectrum that approaches the fully turbulent power-law state[29]. This is indicative of an efficient cascade of fluctuation energy from large scales to small scales. The fast wind cascade is less developed, with large-scale energy less efficiently transferred to dissipative scales.

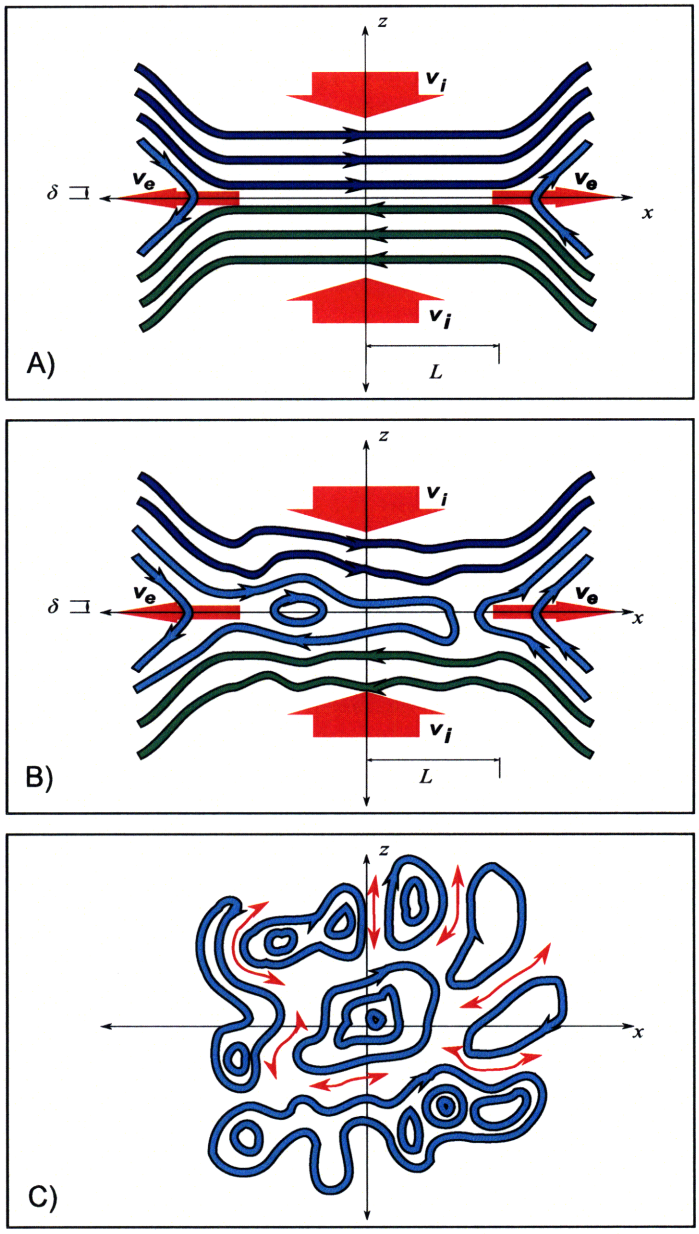

Figure 2.5: A conceptual view of reconnection in a turbulent current sheet. Panel (a) shows the familiar laminar picture. In Panel (b), weak turbulence $\delta B \ll |B|$ couples to the global field to enhance the diffusion rate. In Panel (c), strong turbulence $\delta B \sim |B|$ leads to coupling between plasmoids and a breakdown of the interface.

In principle, a strongly turbulent system can support reconnection rates approaching unity in this fashion. In the limit of strong, fully Alfvénic turbulence, $\langle \delta B \rangle \rightarrow |B|$ implies that $\langle \delta v \rangle \rightarrow c_A$; thus $M_i \rightarrow 1$. In more typical solar wind conditions, this may account for a significant fraction of the global reconnection rate, depending on the actual reconnection rate for the non-turbulent, laminar case. It has also been suggested that turbulence local to magnetic reconnection could be self-exciting. If so, runaway reconnection could occur even in the laminar case, as the motion of reconnected field lines would generate local turbulence, increasing the reconnection rate [53].

Thin Current Sheet Instability

Even in the absence of turbulent inflow, it has been argued [59] and demonstrated numerically [83] that thin current sheets are subject to a fast-growing instability that generates plasmoidal substructure when the magnetic Reynold's number is large ($R_m \gtrsim 10^4$). Loureiro's analysis is based on a perturbative analysis of the weakly-resistive current sheet in 2D, treating $\epsilon \equiv \delta/L$ as a small parameter. Those authors demonstrated that unstable modes with high wavenumber ($\delta < \lambda < L$) arise with growth rates that are fast compared to the Alfvén timescale, $\tau_A = \delta/c_A$, when the aspect ratio of the current sheet is very large.

This instability is similar to the tearing mode [25], which also takes place in sheets where the Reynold's number is high. The tearing mode is a simple resistive instability wherein a perturbative "pinch" of the magnetic field across a current sheet creates a weak X-point. Local to the pinch, the relief of magnetic pressure across the sheet, and the additional tension along it, drive a flow that amplifies the perturbation. The growth of the tearing mode, however, occurs on a hybrid timescale that is intermediate to the diffusive and Alfvénic timescales. The saturation timescale of this instability is proportional to $R_m^{1/2}\tau_A$, which is slow compared to the Alfvénic dynamics of the plasma, and prohibitively slow in the solar wind as $R_m \gg 1$. Furthermore, the fastest growing modes are long-wavelength modes, where the curvature (and thus any restorative magnetic tension) due to the pinch is smallest. Clearly, the tearing mode is too slow and too large-scale to be a significant source of intermittency in solar wind current sheets.

The Loureiro modes are qualitatively similar, but far faster to develop than tearing modes. The fastest growing Loureiro modes are short wavelength ($\lambda \ll L$) and grow with a linear timescale that is proportional to $R_m^{-1/4}\tau_A$. When $R_m \gtrsim 10^4$, this mechanism generates plasmoidal substructure that saturates efficiently regardless of the Alfvénic dynamics. If this instability is at work in nature, large current sheets in the solar wind should be identified with plasmoidal substructure in virtually all cases. Plasmoids generated in this fashion are a likely source of intermittency, and could constitute the type of self-exciting disruption envisioned by Lazarian et al.

Chapter 3

Time series analysis

Identifying reconnection outflows in spacecraft time series data

Simple reconnection geometries may be identified in the solar wind far from the diffusion region by their outflows. As discussed in Chapter 2, the outflow speed associated with magnetic reconnection at a large field shear angle is on the same order as the Alfvén speed of the inflowing plasma. A spacecraft that traverses or is traversed by such an outflow region will record a time series that is characterized by an isolated quasi-Alfvénic flow, corresponding to a one-dimensional cross section of the structure as long as the outflow is steady on a time scale that is long compared to the traversal time. Except under very rare conditions, the solar wind transports structure radially at a speed many times larger than the local Alfvén speed, typically at Alfvén Mach number M_A ~5-10. Thus, the spacecraft crossing time is generally much shorter than the Alfvén crossing time in the radial direction for a convecting structure. For this reason, it is conventional in space physics for a single spacecraft time series to be treated as an approximation of the physical cross section at a single point in time. This approximation is not appropriate, however, for large structures with crossing times on the order of the expansion timescale $\tau_{exp} \sim R/u$ of the solar wind (a few days at 1 AU).

The best way to understand the global structure of a reconnection site, or any structure in the solar wind, is to combine the signatures of a single event observed by multiple spacecraft. In practice, however, multiple spacecraft observations of the same structure are extremely rare. In the absence of multiple spacecraft, the magnetic fields and ion distributions over a single spacecraft transit may still be sufficient to constrain models, provided that some element of the signature can be unmistakably identified with the expected phenomenon. One hallmark of symmetrical reconnection is that the magnitude of the mag-

netic field is decreased in the exhaust region, owing to the annihilation of the reconnecting component. Compressing current sheets and isolated decreases in the magnetic field strength (magnetic holes) are both common occurrences in the solar wind near 1 AU [90, 11]. As defined, magnetic reconnection is a satisfactory explanation for a small subset of non-linear magnetic holes. Similar structures are thought to arise from a broad range of plasma effects, including phase-steepened stochastic MHD structures [93], MHD solitons [4], and saturated ion anisotropy instabilities (i.e. [90, 98]). By itself, reduced field strength at a current sheet certainly cannot be considered an unmistakable indicator of reconnection. The correct coupling of the exhaust flow to the field geometry, however, may be unique to reconnection. The current sheet with an embedded quasi-Alfvénic flow is not identified with any other steady-state phenomenon.

Observations with multiple spacecraft in the solar wind [72, 32] and in the earth's magnetotail (i.e. [77], have helped to establish the association of this particular kind of current sheet with quasi-steady reconnection. Multiple spacecraft at 1 AU have recorded signatures consistent with large ($\sim$0.1 AU) slab-symmetric exhaust wedge geometries in the solar wind in several cases. An exhaustive study of the presence/absence of correlated signatures with coordinated spacecraft has not been performed, however. As a result, it is anecdotally demonstrated that these current sheets can correspond to exhausts in the solar wind on large scales, but it is not clear if this is a normal or exceptional occurrence.

An automated time series analysis was developed to identify signatures that satisfy the key criteria of reconnecting current sheets, and applied to a merged time series combining plasma and magnetic field data for the full duration of the Voyager 2 interplanetary missions. In the next section, the measurements and their errors pertaining to the analysis will be briefly described. In the sections following, the criteria and automation will be discussed in detail.

3.1 Data

3.1.1 Interplanetary plasma data from Voyager 2

Voyager 2 was launched on August 20, 1977 and began reporting plasma and magnetic field data from the interplanetary medium near 1 AU shortly thereafter[9, 5]. Along with its twin, Voyager 1, the spacecraft spent more than three years journeying from 1 to 10 AU, conducting continuous solar wind observations between planetary encounters at Jupiter and Saturn. After the Saturn encounter, Voyager 1 was diverted out of the ecliptic plane and its plasma spectrometer system failed shortly thereafter. Unlike Voyager 1, however, Voyager 2 remained in the ecliptic plane of the solar system until reaching Neptune in the summer of 1989 at a distance of about 30 AU. After the Neptune encounter, Voyager 2 began to leave the ecliptic plane at an angle of about 48° and a speed of

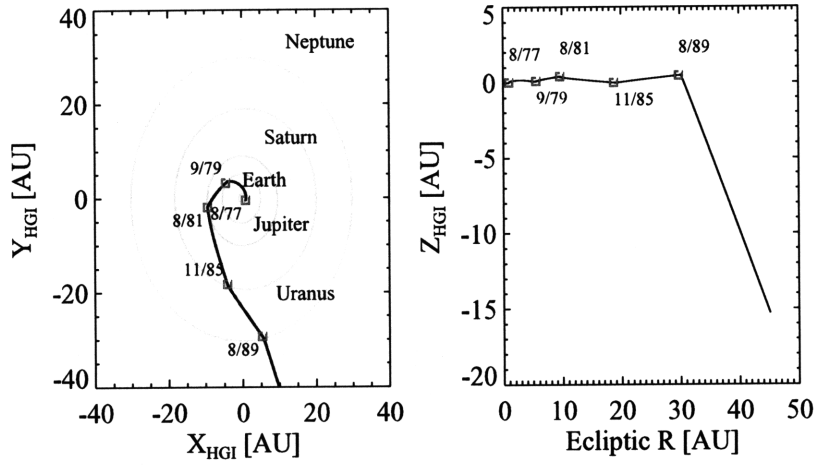

Figure 3.1: The trajectory of Voyager 2. **Left panel:** location in the plane of the ecliptic, in inertial coordinates. Planetary encounter dates are indicated. **Right panel:** distance from Voyager 2 to the ecliptic plane.

about 3.1 AU per year. Presently, Voyager 2 is in the heliosheath, the region of shocked solar wind between the termination shock and the heliopause. As of this publication, the plasma subsystem continues to function. The trajectory of Voyager 2 is shown in Figure 3.1. Magnetic reconnection was observed out to a distance of 34 AU in this thesis.

The full-resolution magnetic field, which is typically available at a faster rate than the plasma moments, is considered in the analysis of Chapters 4 and 5, but is averaged down for the purposes of the search code. The magnetic field data are averaged component-by-component to the cadence of the fastest available plasma parameters to create a single merged data set for searching. Data analyses will refer to these merged data except where otherwise noted.

The data coverage for this study is mitigated by telemetry gaps that occurred with increasing frequency and duration as the mission progressed. In terms of heliocentric distance, the typical cruise sampling period for our merged data set is 12 seconds inside of 3 AU, 96 seconds from 3 to 6 AU, and 192 seconds beyond. The total coverage by sampling rate as a function of heliocentric distance is summarized in Figure 3.2.

Thermal ion spectra

The Voyager 2 plasma experiment (PLS) consists of three Faraday cup plasma detectors clustered about an axis of symmetry that is roughly aligned in the

-$\hat{\mathbf{R}}$ direction, and a fourth cup that is oriented perpendicular to the cluster axis [9]. Each of the three sun-facing cups is tilted 20° from the cluster axis and they are 120° apart in azimuth. A modulator grid at each Faraday cup establishes a discrete window of ion energy admittance that is cycled through 128 steps. The ion flux admitted in each energy step registers a current that is proportional to a cross section of the phase space distribution function. In the solar wind, the cluster can scan the full range of channels, sampling the full distribution function, once every twelve seconds. At large distances from the sun, the required integration time is longer and sampling rates vary from 12 to 192 seconds.

The flux admitted by the Faraday cup is highest when the bulk solar wind flow is aimed directly down the axis of the cup. Because the main plasma instrument cluster is oriented back towards the sun, the measured radial velocity component, v_R, is based on the sum of the currents in the three sunward cups. The radial component of the solar wind speed is measured to a very high accuracy, generally $\sigma_{v_R}/v_R \sim 0.005$ or better near 1 AU [9]. The uncertainty in the flow angle is directly proportional, scaling as $\sigma_\phi \sim \sigma_{v_R}/(v_R \cos\phi)$ for small flow angles. At 1 AU, the single-spectrum error associated with v_N and v_T is typically a few km/s.

At 1 AU, the energy channels are narrow enough to fit each thermal peak over about$\sim$20 data points, each subject to a quantization error of 1.8%. Fits of the density and thermal speed in that near 1 AU are accurate to better than 2%. At 30 AU and beyond, the solar wind temperature is roughly constant due to heating by pickup ions [47]. In this regime, thermal peaks typically span five or more channels and fits are subject to binning and quantization errors amounting to $\lesssim$5%. The minimum measurable density is strongly dependent on the cup orientation to the bulk flow and the integration time.

Each full sample of the distribution function is retained so that more advanced fitting with multi-component Maxwellian or anisotropic Maxwellian models may be attempted where appropriate. The errors associated with advanced fitting vary widely with conditions, and will be discussed in later sections where appropriate.

Magnetic fields

The low magnetic field investigation on board Voyager 2 was designed to measure field strengths from 0.01 nT up to 1000 nT in the interplanetary solar wind and in planetary magnetospheres [5]. The experiment consists of two identical triaxial fluxgate magnetometers in separate locations on the spacecraft. This redundancy is designed to help characterize the complex, time-dependent field generated by the spacecraft so that it may be removed from the environmental field. The instrument measures three orthogonal field components independently, each with a measurement uncertainty of $\pm$0.1 nT at 12-second intervals, and $\pm$0.03 nT when averaged to 48-seconds. Beginning in 1985, unaccounted

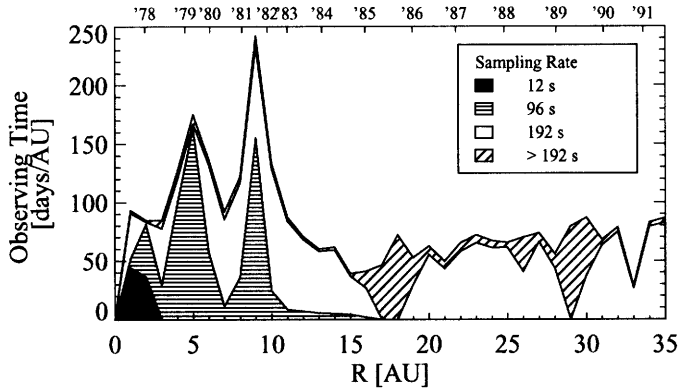

Figure 3.2: Voyager 2 interplanetary mission coverage for the merged plasma and magnetic field data set.

offsets in the magnetic field with periods of 1-12 hours have occurred that must also be corrected for. A measurement accuracy of $\pm 0.02 - 0.05$ nT at the 48-second rate is quoted by the instrument team for the corrected fields in the presence of this phenomenon and other late-mission uncertainties [12] .

The interplanetary magnetic field strength decreases by more than an order of magnitude in the merged data set, from $\sim$5 nT at 1 AU to $\sim$ 0.2 nT at 30 AU (see Figure 3.3). It is clear that uncertainty will become an important consideration for magnetic feature detection late in the study, however we note that spacecraft charging and anomalous offsets are low-frequency effects. These impact the accuracy, but not the precision of field vector measurements. Feature detection relative to measurement noise of ± 0.02 nT can still be possible in the presence of these offsets.

Interplanetary magnetic field vectors are not considered reliable by the MFI team after the Neptune encounter. The usable data for this study is very limitted from the point that Voyager 2 leaves the ecliptic plane. Hourly averages of the field vector will be used for case studies, but the continuous, high-resolution field data that accompanies the plasma data ends in 1991.

3.1.2 1 AU plasma data with Wind

Ongoing solar Wind observations near earth will frequently be used as a point of reference/departure for this study. The Wind spacecraft is well suited to this use. Wind is a spin-stabilized earth orbiter, one purpose of which is to provide baseline, 1 AU, ecliptic plane observations for inner and outer heliospheric missions. The spacecraft has undergone various interesting orbital maneuvers since launch in 1994. The three primary orbital states are (1) halo orbit around the

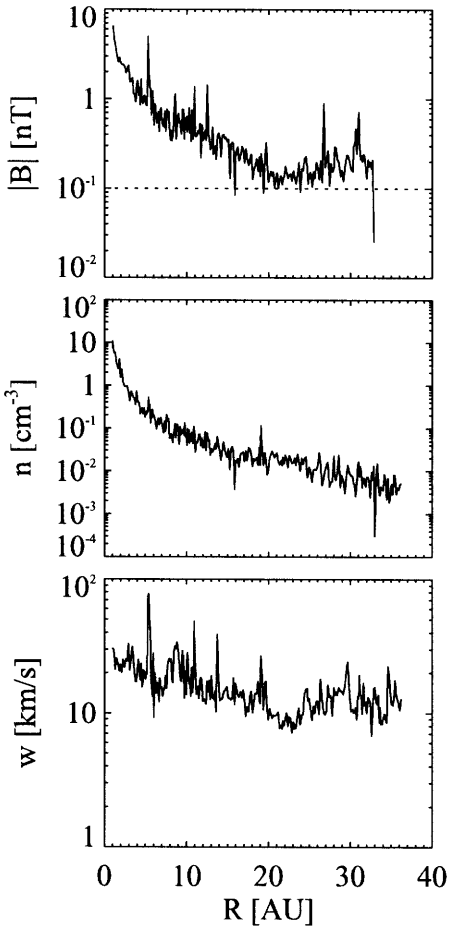

Figure 3.3: Monthly averages of the solar wind magnetic field strength, $|B|$, proton density, n, and proton thermal speed, w, as a function of heliocentric distance. The estimated sensitivity limit for the magnetic field instrument is shown with a dotted line in the top panel.

first earth-sun Lagrange point, observing the solar wind approximately 0.01 AU upstream of the earth, (2) prograde orbit to observe the solar wind in the ecliptic plane east and west of the earth to a few times 0.01 AU, and (3) "petal" orbit out to $\sim$ 50 earth radii, to frequently observe the solar wind-magnetosphere transition. We do not consider any periods where Wind is within the earth's magnetosphere.

Thermal ion spectra

The wind 3D particle (3DP) experiment includes ion electrostatic analyzers that measure the fully three-dimensional ion distribution 32-64 times per spin [57]. We use on board proton moment (3 second) measurements from the low-energy proton analyzer instrument (3DP/PESA-L) analyses here. Particle density is calculated as an integral over the distribution, velocity as the center of the distribution, and particle thermal temperature as the second moment of the distribution. For each, errors are due primarily to time aliasing and to real non-Gaussian solar wind distributions, rather than to measurement uncertainty. Errors in these quantities are taken to be less than 1%.

Magnetic fields

The magnetometer instrumentation included in the WIND Magnetic Field Investigation (MFI) is based on the magnetometers previously developed for the Voyager [63]. Nominally, magnetic field vectors are measured in three directions simultaneously at a rate of 10.9 per second. The data product used here is the 3-second spin-averaged field vector. These measurements are precise to within 0.025% [56].

3.2 Observables

With instrumentation to measure magnetic field vectors and moments of the thermal plasma distribution, a spacecraft such as Voyager 2 will record two boundary layers when crossing a reconnecting current sheet as $\mathbf{B}$ and $\mathbf{v}$ rotate from the upstream inflow orientation to the outflow orientation, and then to the downstream inflow orientation. The outflow region contains some nonzero magnetic field normal to the boundary, denoted B_n, that indicates the connection of upstream and downstream field lines. The fly-through time signature for an ideal Petschek reconnection exhaust is shown in Figure 3.4. A more realistic fly-through may be characterized by different levels of compressibility of the plasma depending on the β parameter, asymmetry due to differences in the upstream and downstream conditions, a different outflow Mach number corresponding to a different opening angle, and other variations. The characteristic of the signature that does not change is based on the pair of Alfvénic disturbances that

must together divert the inflowing plasma. At the boundaries where the field is kinked, the diverted plasma flows as an Alfvén wave propagating parallel (antiparallel) to the reconnecting field and producing correlated (anti-correlated) variations in $\mathbf{v}$ and $\mathbf{B}$. As the upstream and downstream kinks both propagate away from the reconnection site, the changes $\Delta\mathbf{v}$ and $\Delta\mathbf{B}$ must be correlated at one boundary and anti-correlated at the other. This is the primary observable element of magnetic reconnection and is the starting point for most studies of reconnection in the solar wind and magnetosphere to date (i.e. [89, 39, 35, 34]).

Discontinuities in space plasmas, such as the boundaries of the reconnection outflow, are classified by two parameters: the field strength along the normal to the discontinuity, $B_{\parallel}$, and the flow of plasma across the discontinuity, $G=\rho v_{\parallel}$ [68]. Discontinuities with $B_{\parallel} \neq 0$ and $G \neq 0$, such as reconnection exhaust boundaries, are called rotational discontinuities.

It should be pointed out that turbulent Alfvén waves in the solar wind may create rotational discontinuities not associated with reconnection. A qualitatively similar signature to that described here could be created by a pair of independent, stochastically steepened Alfvén waves. Such a configuration could re-create the appropriate rotations of $\mathbf{B}$ and $\mathbf{v}$ at two boundaries that are intermittent and/or non-stationary with respect to the bulk flow of the plasma and to each other. It has been hypothesized by some authors that Alfvénic fluctuations, be they turbulent or otherwise, may conspire to produce discontinuities accounting for some or all of the reconnection-like signatures observed in the solar wind to date [84]. One important observation to make is that purely Alfvénic propagating rotational MHD discontinuities are by nature non-compressive and preserving the magnitude of the magnetic field [68]. To distinguish reconnection from the type of phenomenon hypothesized by Scudder, one must rely on evidence of compression and magnetic energy conversion. The plausibility of Scudder's argument, then, rests in part on the presence of sufficient energy in compressive fluctuations to contribute significant false positives. Compressive turbulence in the solar wind is significantly weaker than Alfvénic turbulence in both the slow and fast states. For the most part, if the magnetic field strength is reduced and/or the thermal energy is increased in the inner region of a reconnection signature, one can be confident that the boundaries are not stochastic rotational discontinuities. The false positive rate will be addressed quantitatively in Section 3.2.2 and in future work.

It is also noted with respect to Scudder's contention that strong Alfvénic turbulence propagating along the mean field away from the sun is certainly caused by phase mixing between outwardly propagating modes of solar origin. Whether or not substantial *sunward*-propagating wave power exists in the solar wind is a controversial subject [36]. Sunward-propagating Alfvén waves have been demonstrated in limited context through stochastic processes [81] and in association with disconnection of flux from the sun [40]. In both cases, the sunward component is estimated to be a very small fraction of the total wave power. Sunward waves can also occur via reflection from planetary magnetospheres [68]. In certain environments, ahead of the earth's magnetopause for

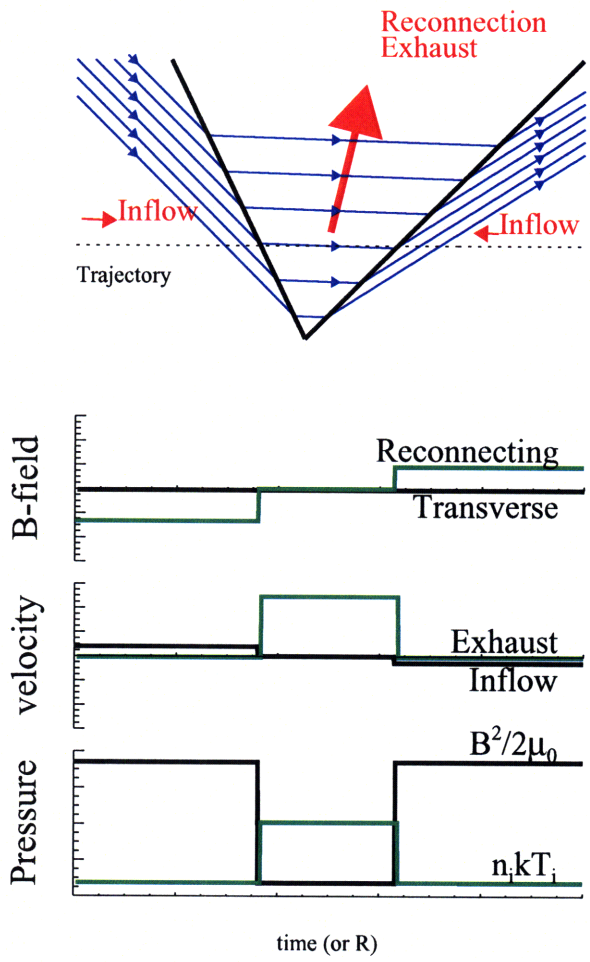

Figure 3.4: An illustration of the changes $\Delta\mathbf{v}$ and $\Delta\mathbf{B}$ across a pair of exhaust boundaries. In the top panel, magnetic field lines are shown in blue, with the discontinuity planes in solid black. The dotted line depicts the effective spacecraft trajectory through the structure. The lower three panels show the in-plane components of the magnetic field, the in-plane components of the velocity in the co-moving frame, and the pressure components of the plasma.

instance, Scudder's theory should certainly be explored. These circumstantial situations cannot, however, be the sources envisioned by Scudder that could seed a universal, omnidirectional "Alfvénic sea" in the solar wind. Without a strong source of sunward wave power flux, the collision of sunward anti-sunward pairs of stochastic rotational discontinuities would certainly not be observed.

3.2.1 The Walen Test

Across a given rotational discontinuity, the tangential electric field must remain constant [68]. Along with the conservation of mass flux this implies that, when the pressure is isotropic,

$$\Delta \mathbf{v}_\perp \propto \pm\Delta\frac{\mathbf{B}_\perp}{\sqrt{4\pi\rho}}, \tag{3.2.1.1}$$

where the perpendicular subscript denotes components perpendicular to the discontinuity normal, $\hat{\mathbf{n}}$ (and thus tangential to the discontinuity). It is also true that, in the frame co-moving with the discontinuity, ΔB_n and Δv_n are both equal to zero. This relation establishes that the boundary is a shear Alfvén kink, i.e. the tangential velocity difference is equal to the tangential Alfvén velocity difference, hereafter denoted $\Delta\mathbf{c}_{\mathbf{A},\perp} \equiv \Delta\frac{\mathbf{B}_\perp}{\sqrt{4\pi\rho}}$. By verifying that the upstream and downstream bifurcations of a current sheet satisfy these relations in the same frame with opposite signs, one verifies that the flow and field are correctly configured for a stationary reconnecting structure. This has come to be referred to as the Walen test of opposite sign.

In practice, we verify the Walen condition for a given reconnection candidate with the following procedure:

1. Prescribe three data periods of interest corresponding to the upstream (*up*), downstream (*dn*), and exhaust (*e*) regions.
2. Select all possible pairs of velocity measurements, $\mathbf{v}$, and Alfvén velocity measurements, $\mathbf{c_A}$, across the two boundaries, denoted 1 and 2. Build bootstrap distributions for the difference vectors: $\Delta\mathbf{v}_1$, $\Delta\mathbf{v}_2$, $\Delta\mathbf{c}_{A,1}$, and $\Delta\mathbf{c}_{A,2}$.
3. Require that each of these distributions prescribes a unique direction, $\hat{\mathbf{e}}_{\Delta\mathbf{v},1}$, $\hat{\mathbf{e}}_{\Delta\mathbf{v},2}$, $\hat{\mathbf{e}}_{\Delta\mathbf{c_A},1}$, $\hat{\mathbf{e}}_{\Delta\mathbf{c_A},2}$, that is localizable to an octant on the unit sphere.
4. Require agreement $\hat{\mathbf{e}}_{\Delta\mathbf{v},1} = \pm\hat{\mathbf{e}}_{\Delta\mathbf{c_A},1}$, $\hat{\mathbf{e}}_{\Delta\mathbf{v},2} = \mp\hat{\mathbf{e}}_{\Delta\mathbf{c_A},2}$ to within a 1-σ error ellipse on the unit sphere associated with each distribution.

We define the Walen test function, from (3) and (4) simply as

$$\mathcal{W}_{\pm} \equiv \begin{cases} 1 & \hat{\mathbf{e}}_{\Delta \mathbf{v},1} = \pm \hat{\mathbf{e}}_{\Delta \mathbf{c},1} \text{ and } \hat{\mathbf{e}}_{\Delta \mathbf{v},2} = \mp \hat{\mathbf{e}}_{\Delta \mathbf{c},2} \\ 0 & \text{otherwise} \end{cases} . \tag{3.2.1.2}$$

This function will be multiplied by a statistical weight function, $q_\star$, to form the basis of our exhaust detection algorithm. This weight function, which will be defined rigorously in Section 3.3, is a measure of the discontinuity magnitudes relative to the background. The $q_\star$ will be constructed to be non-zero whenever all four of the difference vectors, $\Delta \mathbf{v}_1$, $\Delta \mathbf{v}_2$, $\Delta \mathbf{c}_{A,1}$, and $\Delta \mathbf{c}_{A,2}$, are large compared background fluctuations.

This procedure is illustrated for a reconnection exhaust observed with Wind in the right panel of Figure 3.5. In that figure, difference vectors are plotted on the unit sphere to demonstrate the correlated and anticorrelated loci that correspond to the best choice of exhaust boundaries. The criterion described here is seemingly loose, but makes for an efficient sieve. To demonstrate this, we can employ the method described in Stevens & Kasper[90] to generate fake turbulent solar wind time series data for both $\mathbf{v}$ and $\mathbf{c_A}$ with realistic variances and spectra. We can then include pairs of randomly generated discontinuities in those time series. To characterize the sieve, we apply the Walen test procedure to many fake data trials and count false positives. Each trial time series consists of a unique, randomly generated background into which two pairs of discontinuities, ($\Delta \mathbf{v}_1$, $\Delta \mathbf{c}_{A,1}$) and ($\Delta \mathbf{v}_2$, $\Delta \mathbf{c}_{A,2}$), are added with random relative orientations.

The acceptance rates are given in Table 3.1. In each trial, the model background is moderately turbulent, consisting of Kolmogorov spectrum fluctuations with an average magnitude given in the first column. The number of resolved points, in the second column, is the number of data points that would be measured by Voyager 2 between the two discontinuities. These numbers are chosen to correspond to real convection times from a few minutes to a few hours. Each rate is the result of 5,000 trials for the given combination of parameters. Note that the false positive rate is not higher for longer averaging times. This is attributable to the power spectrum of the background, in which fluctuations become stronger at longer wavelengths. The typical false positive rate for events in this study is $\sim 5\%$.

Table 3.1 shows that even when randomly oriented structures are included in an *ad hoc* fashion, they will only satisfy the Walen criterion in a small number of instances. The net false positive rate for a reconnection signature search based on this test would be the product of this acceptance rate and the rate of intermittent solitary structure formation in the solar wind. The probability distribution function for small fluctuations in the solar wind is Gauss-normal. For any given choice of stream boundaries, then, the chance of a false positive detection from a pair of uncorrelated discontinuities that are n times stronger than the background fluctuation level, σ, should go roughly like $\sim 0.05 \cdot \exp(-n^2)$

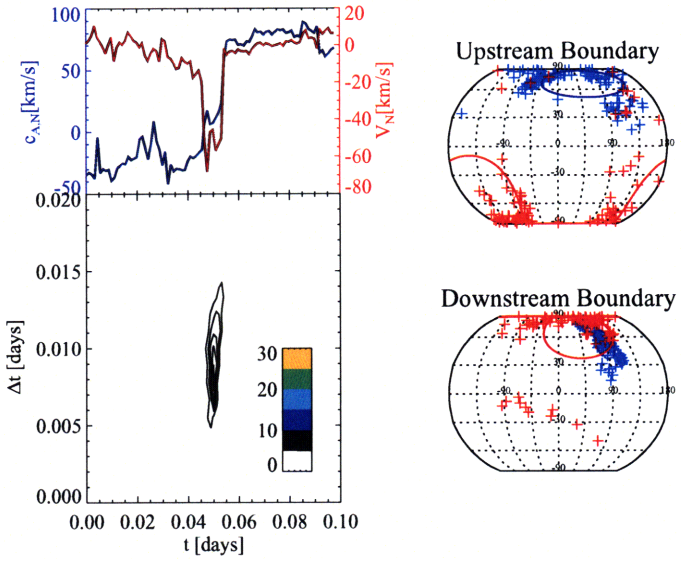

Figure 3.5: An example of a reconnection event detection. At left, the reconnecting component of $\mathbf{c_A}$ and exhaust outflow component of $\mathbf{v}$ are shown in time. The time series is shown above a contour map of the weight function, $q_\star$ as a function of the time, t, and the separation between the discontinuities, Δt. The filled contours are restricted region where $\mathcal{W}_\pm = 1$, showing a maximum at approximately $(t, \Delta t) = (0.05, 0.1)$. At right, the difference vectors $\mathbf{\Delta v}$, in red, and $\mathbf{\Delta c_A}$, in blue, that correspond to this maximum are plotted on the unit sphere along with 1-σ ellipses about their mean directions. The upstream transition is correlated and the downstream is anti-correlated.

$\delta v/v$ or $\delta c_A/c_A$	exhaust points	false positive rate (%)
0.1	3	1.9
0.1	10	2.6
0.1	30	2.4
0.3	3	6.0
0.3	10	7.3
0.3	30	7.4

Table 3.1: Percentage of randomly generated discontinuity pairs that are accepted by the Walen condition sieve. Percentage errors are one significant Figure.

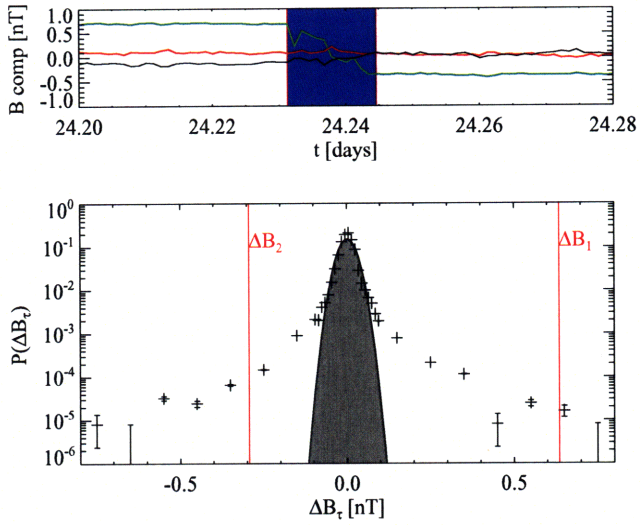

Figure 3.6: A pair of well-resolved magnetic field discontinuities at a reconnection exhaust site. **Top panel:** time series showing the B-field components. Two discontinuities, $\mathbf{\Delta B_1}$ and $\mathbf{\Delta B_2}$, bound the exhaust region, which is shaded blue. **Bottom panel:** the distribution of B-field fluctuations on the exhaust transit timescale. The core of the distribution, which is Gaussian, is shown in grey. The statistical magnitudes of the two discontinuities are shown with vertical bars. These discontinuities are well beyond the core, at $\sim 6\sigma$ and $\sim 13\sigma$.

for small n. At large n, the distribution of fluctuations in the solar wind is not Gaussian, and the false positive rate at diminishing probability transitions to a power law. This is illustrated for a real Walen signature in the solar wind in Figure 3.6.

The full condition for shear-stress balance across a discontinuity, more commonly called the Walen condition, is that an inertial frame exists, which we denote HT, wherein the convective electric field is zero and the plasma jump conditions satisfy

$$\mathbf{v} - \mathbf{v_{HT}} = (1-\alpha)\frac{\mathbf{B}}{\sqrt{4\pi\rho_1(1-\alpha_1^2)}} \tag{3.2.1.3}$$

where α denotes the thermal pressure anisotropy factor, defined by

$$\alpha \equiv \beta_{||} - \beta_{\perp} = \frac{p_{\shortparallel} - p_{\perp}}{B^2/8\pi}. \tag{3.2.1.4}$$

This reference frame is called the d'Hoffman-Teller frame [89]. In this frame, the elimination of the convective electric field ($\mathbf{E_c} = \mathbf{v} \times \mathbf{B} = 0$) implies

that there is no drift of the plasma relative to the field, i.e. the frame is co-moving with reconnecting field lines. The flows are aligned and Alfvénic, then, on both sides of the discontinuity. A reference frame velocity to guarantee consistency with this relation should be found for every candidate reconnection event.

3.2.2 Secondary indicators of reconnection outflows

In addition to the Walen conditions, there are other measurable properties one might expect of reconnection outflows, though the detection of these properties will be considered secondary for identification. These are discussed below:

1. Strongly reduced magnetic field strength in the outflow. It has been argued that because most reconnection events in the solar wind are not driven by strictly symmetrical upstream and downstream flows, the magnetic energy density of the outflow may actually exceed that of the weaker-field side. However, the exhaust field strength is not to exceed the mean inflow field strength, as that would indicate a pile-up of flux rather than relief of magnetic stress by reconnection.

2. Increased thermal pressure in the outflow. As in (1), it is possible for the density and/or temperature of the outflow to be less than that of the hotter/denser inflow in asymmetric reconnection. For a current sheet to be in steady-state, however, the system must be in pressure balance. Basic theoretical models suggest that the energy associated with the inflowing reconnecting magnetic field is converted to heat and kinetic energy of the outflow in rough equipartition[75].

3. A well-defined minimum variance frame consistent with $\mathbf{v}_{HT}$. Under favorable circumstances, the d'Hoffman-Teller frame can be found as the reference frame in which the mean-square convective electric field is minimized across the exhaust [89]. This is accomplished by finding the vector $\mathbf{v}_0$ corresponding to the minimum of the function

$$\delta E_c(\mathbf{v_0}) = \left\langle |(\mathbf{v} - \mathbf{v_0}) \times \mathbf{B}|^2 \right\rangle . \qquad (3.2.2.1)$$

4. Alfvénic outflow speeds relative to the bulk plasma. As argued above, the outflow speed is approximately equal to the Alfvén speed associated with the reconnecting field component. Far from the reconnection site, however, it is possible for the outflow jet to slow as material is swept up and the jet impinges on a region where driving is weak. The dissipation of reconnection outflows is a largely unstudied topic, but is addressed in [35]. For the purposes of a reconnection sieve, the outflow Mach number should be significantly higher than the inflow Mach number.

3.3 Confusion-limited automated detection

One procedure for finding regions-of-interest (ROIs) in time series data is to create what is often referred to as a "sliding window" function that can be evaluated at different times and timescales. In Stevens et al.[90], an algorithm was implemented to test for three-part ROIs consisting of an upstream region, a target region, and a downstream region that together obeyed a particular magnetic field condition. The strength of a detection, relative to the confusion limit, in some target time period can be defined in terms of the variance of the appropriate parameters in the periods immediately upstream and downstream. A similar strategy is employed here. The changes $\Delta\mathbf{v}$ and $\Delta\mathbf{c_A}$ that are taken to constitute a Walen signature must be statistically significant relative to other fluctuations on like scales for a reconnection outflow to be uniquely identifiable. What follows is a formalism for detecting reconnection exhaust signatures in a scale-free way. The sliding detection window consists of a target time period with some central time and duration that we scan over all possible times and scales, seeking to match to the times and durations of reconnection exhaust signatures. The window also includes a reference period on which a confusion baseline is measured. That reference period is scaled with the size of the window, and it consists of upstream and downstream data but excludes the target itself.

3.3.1 Formalism

The detection of a reconnection signature is a confusion-limited measurement, as opposed to a resolution-limited or noise-limited measurement, in that the background one must compare to is comprised of real fluctuations and not instrumental uncertainty or noise. As described in sections 2.2.6 and 3.2, fluctuations are omnipresent on all measured scales in the solar wind. Typically, the Wind MFI instrument measures a magnetic field variance on the order of 0.1-0.5 nT in the slow solar wind at 1 AU with 3-second resolution. Similarly, the Wind 3DP experiment clearly resolves large fluctuations in all parameters at the 3-second spin resolution of the instrument. Because the identification of solar wind signatures is usually confusion-limited, there is no strict working definition of a discontinuity. A wide variety of waves, steepened to every conceivable profile are no doubt present and interacting to some degree on every scale of the solar wind down to the ion inertial length. We are interested, however, in the emergence of singular structures that dominate the turbulent environment. One would expect that any such emergent structures either arise from non-stochastic processes, or have a somewhat predictable rate of intermittency dictated by the turbulent spectrum.

The distinguishability of a structure or discontinuity is most naturally quantified in terms of the magnitude of the background fluctuations that accompany it. For the three-part ROI, the variance of a parameter, such as proton velocity, is measured in the upstream and downstream regions as a baseline.

The relevant change in that parameter in and across the target region is compared to that variance. The scale of the upstream and downstream region is chosen to be an order of magnitude larger than that of the target region. In this framework, let us use the subscript 0 to denote the background, which excludes the target. A solitary structure in some parameter X is said to be detected at the $n\sigma$ level if

$$N_X \equiv \frac{1}{\sigma_{X,0}} \left| \langle X \rangle_{target} - \langle X \rangle_0 \right| \geq n, \tag{3.3.1.1}$$

$$\text{where } \Delta t_{target}/\Delta t_0 \ll 1.$$

In practice, we parametrize the background duration relative to the target duration with a scale factor, s, such that $\Delta t_0 = 2s \cdot \Delta t_{target}$. Let us drop the *target* subscript and take the window duration to be an independent variable, Δt, that will be varied over a large range of values from the measurement limit ($\Delta t_{min} \sim$ 10 s to 1 min) up to the expansion timescale of the plasma ($\Delta t_{max} \sim$ 1day). Consider the window of scale Δt centered at a time t on a data set with resolution dt. We can explicitly define the following range-specific moments for the exhaust (e), downstream (dn), and upstream (up) regions of the window as follows:

$$\langle X \rangle_{(t,\Delta t);\, e} = \frac{dt}{\Delta t} \sum_{i=0}^{\Delta t/dt} X(t - \Delta t/2 + i \cdot dt) \tag{3.3.1.2}$$

$$\langle X \rangle_{(t,\Delta t);\, \substack{dn \\ up}} = \frac{dt}{s\Delta t} \sum_{i=0}^{s\Delta t/dt} X(t \pm \Delta t/2 \pm i \cdot dt) \tag{3.3.1.3}$$

$$\sigma^2_{(X,t,\Delta t),\, \substack{dn \\ up}} = \frac{dt}{s\Delta t} \sum_{i=0}^{s\Delta t/dt} \left[X(t \pm \Delta t/2 \pm i \cdot dt) - \langle X \rangle_{\substack{dn \\ up}} \right]^2 \tag{3.3.1.4}$$

We seek to construct a window function, $Q_s(\mathbf{c_A}, \mathbf{v}, t, \Delta t)$, that reflects the relative probability that a reconnection exhaust has occurred with crossing time Δt centered at time t in some data set. To build a window function for reconnection exhausts, we combine the criteria outlined in Sections 3.2.1 and 3.2.2. This function must be identically zero when any one of the absolute criteria, such as the Walen test of opposite sign, is violated. When all absolute criteria are satisfied, the window function should provide a measure of the quality of detection. A practical prescription for Q_s is given by the following:

$$Q_s = q_\star \cdot \mathcal{W}_\pm \cdot \mathcal{C}. \tag{3.3.1.5}$$

We incorporate the statistical significance of the individual boundaries in the weight function, $q_\star$. The absolute criteria from the Walen Test and from our secondary indicators are incorporated into $\mathcal{W}_\pm$ and $\mathcal{C}$, respectively. The weight function is the product of four separate statistical weights, corresponding to the changes in $\mathbf{v}$ and $\mathbf{c_A}$ across both boundaries. Continuing to denote the upstream and downstream boundaries with the subscripts 1 and 2, respectively, we make the following definitions:

$$q_\star \equiv q_{\mathbf{v},1} \cdot q_{\mathbf{v},2} \cdot q_{\mathbf{c_A},1} \cdot q_{\mathbf{c_A},2}, \tag{3.3.1.6}$$

where

$$q_{\mathbf{X},\frac{1}{2}} \equiv \begin{cases} N_{\mathbf{X},\frac{1}{2}} & N_{\mathbf{X},\frac{1}{2}} \geq n_{min} \\ 0 & N_{\mathbf{X},\frac{1}{2}} < n_{min} \end{cases}$$

$$\text{with } N_{\mathbf{X},\frac{1}{2}} \equiv \frac{1}{\sigma_{(X,t,\Delta t),\,\frac{up}{dn}}} \left| \langle \mathbf{X} \rangle_{(t,\Delta t);\,e} - \langle \mathbf{X} \rangle_{(t,\Delta t);\,\frac{up}{dn}} \right|, \tag{3.3.1.7}$$

and, finally

$$\mathcal{C} \equiv \begin{cases} 0 & \langle B^2 \rangle_e \geq \max\left(\langle B^2 \rangle_{up}, \langle B^2 \rangle_{dn} \right) \\ & \text{or } \langle p_i \rangle_e \leq \min\left(\langle p_i \rangle_{up}, \langle p_i \rangle_{dn} \right) \\ & \text{or } \left\langle \frac{|\mathbf{v}-\mathbf{u}|}{c_A} \right\rangle_e \leq \left\langle \frac{|\mathbf{v}-\mathbf{u}|}{c_A} \right\rangle_{up,dn} \\ 1 & \text{otherwise} \end{cases}, \tag{3.3.1.8}$$

where $\mathbf{u} = \frac{1}{2}\left(\langle \mathbf{v} \rangle_{up} + \langle \mathbf{v} \rangle_{dn} \right)$ and p_i is the scalar ion pressure. (3.3.1.9)

The mappings $q_{\mathbf{X},\frac{1}{2}}$ are illustrated in Figure 3.7 for a reconnection exhaust observed by Voyager 2. In these plots, the q-score is shown in color scale as a function of the window time, t, and the window size, Δt. For each detection, a locus of points exists in $(t, \Delta t)$ corresponding to a range of windows that approximately fit the discontinuity. Multiple maxima frequently may correspond to degeneracy between the identification of a double-step at small scales verses a single-step at large scales. Another source of multiple maxima arises when the upstream window overlaps the downstream discontinuity, or vice-versa. These ambiguities are removed when the product of the four functions is taken.

An illustration of the complete detection algorithm incorporating the Walen test function has been shown in Figure 3.5.

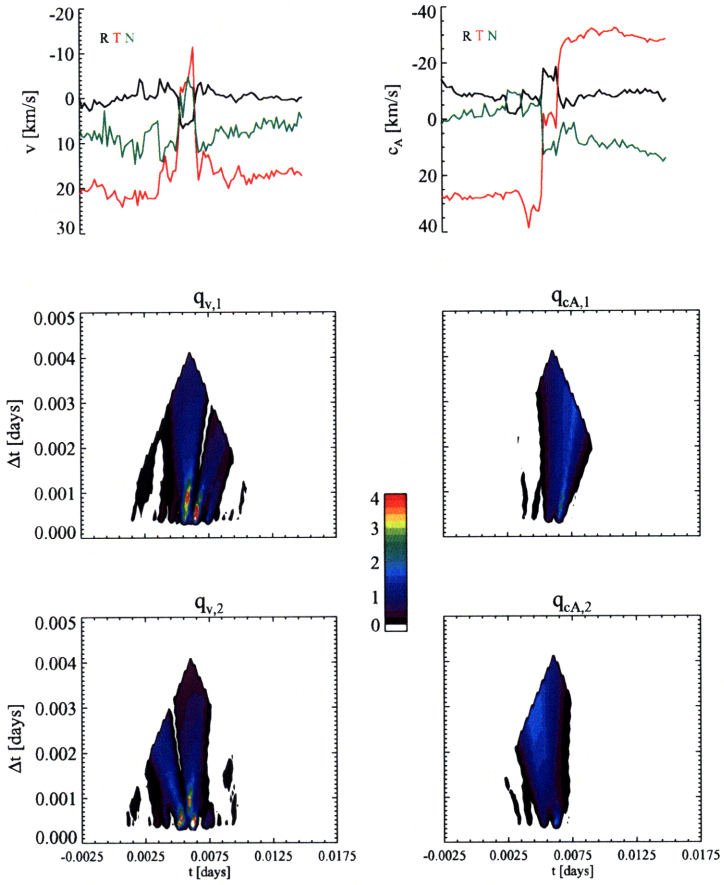

Figure 3.7: The weight functions, q, computed as in Equation 3.3.1.7 for the discontinuities bounding a Voyager 2 reconnection event. In the first row, the flow velocity and Alfvén velocity components are shown over time across the structure. In the second and third rows, the q-scores are shown on a linear color scale for a range of window sizes, Δt, on the same time period. Best-fit coordinates in $(t, \Delta t)$ correspond to maxima of the contour plots. The white regions of each contour plot corresponds to $q = 0$.

3.3.2 Parameters of the Search Algorithm

The analysis above essentially has two free parameters. The first is the scale factor, s, and the second is the cutoff parameter, n_{min}. One is free to choose the values for these parameters according to what one considers to constitute a discontinuity in the plasma. A fully quantitative optimization of n_{min} and s for reconnection would require a turbulent, multi-scale MHD model of the solar wind incorporating the field, flow, and compressivity of the plasma. The development of such models is a goal unto itself, however. We choose to follow some established conventions in our choice of parametrization. These will now be discussed in turn.

The s parameter dictates how many times larger the inflow/background region must be than the exhaust region. In the context of intermittency studies in MHD turbulence (e.g. [41]), s is akin to a minimum waiting time between discontinuities. In the context of solitary wave analysis (e.g. [90, 24]), s constitutes a scaled measure of isolation. For large s, nearby discontinuities and low-frequency oscillations have an increasing effect on the variance, raising the detection threshold. For small s, on the other hand, the concept of a discontinuity loses its meaning. In our present framework, it is implicit that the inflows identified upstream and downstream must be long-lived enough to support a quasi-steady state wherein the inflow is steady on a timescale that is large compared to the Alfvén crossing time of the exhaust. These criteria are, in fact, almost always satisfied for $s \sim 1$, as the Mach number of the inflowing plasma is usually small. We choose $s = 2$ to ensure isolation of the structure and further minimize false detections.

The cutoff parameter, n_{min}, provides a baseline magnitude below which a feature cannot be considered a discontinuity. Intermittency studies in the solar wind have shown that the probability density function (PDF) for fluctuations in a given parameter $\delta X_{\Delta t}=\langle X(t) - X(t + \Delta t)\rangle$ differs from the Gaussian distribution at large amplitudes in a manner that is strongly scale-dependent [80, 41]. The rate of small-amplitude fluctuations, however, is well-approximated by a Gaussian PDF on all scales. Intermittency is often quantified in terms of this deviation from Gaussianity in the tails of the PDF. A typical working definition of "discontinuity" is a boundary between two plasma populations that differ by greater than 2σ in some parameter. We have followed that convention and chosen $n_{min} = 2$ as the cutoff for each discontinuity score, q. The calculation of Q_2 for all reasonable values of $(t, \Delta t)$ on a spacecraft time series is computationally intensive for a large data set. The number of necessary computations scales as the full duration of the mission, T, times the maximum window size, Δt_{max}. Following the method of Stevens et al.[90], this problem is reduced to order $T \cdot \log \Delta t_{max}$by a prime factorization technique that eliminates redundancy in computing the statistical moments for overlapping windows.

3.3.3 Reducing the Q_2 Map

For a given spacecraft time series, contiguous regions of non-zero Q_2 in $(t, \Delta t)$-space are each identified with a unique reconnection signature. The choice of $(t, \Delta t)$ for which Q_2 is maximized on each of these regions prescribes the window that best fits the exhaust crossing. In some cases, multiple maxima or multiple regions of non-zero Q_2 that are not contiguous may occur for the same event. For each case, regions and maxima that are within a range Δt of the absolute maximum are grouped with the event corresponding to that maximum. A recursive algorithm was developed to order non-zero elements of the Q_2 map in this way, beginning with the largest maxima and proceeding to the smallest.

3.3.4 Selection Biases

This type of search can be expected to differ qualitatively from a search by simple inspection. It is constructed to be rigorous, and to provide a list of reconnection signatures for which we can discuss the statistics and context with confidence. Certain events that may be clear from a skilled visual inspection of the data may be omitted by this algorithm, however.

Exhaust signatures with asymmetric upstream or downstream regions are more difficult to detect. For a given exhaust signature, if there is a field gradient or velocity gradient in either region, that gradient will contribute strongly to the sigma value. In this way, inflow populations with significant slopes or other low-order moments, which might be easily picked out by eye, are harder to detect automatically.

Multiple crossings of the same reconnection event may be possible with the proper orientation. Such exhausts may be difficult to detect or to fit properly because each crossing event can contribute strongly to upstream or downstream variance of another. For window scales that are on the order of the separation between the two crossings, thus incorporating both crossings into the same exhaust window, the combination of the two will not satisfy the Walen relation. For window scales that are small enough to exclude the second crossing, the maxima of Q_2 may be significantly offset from the actual center times. To correct for this, regions of high $q_\star$ that do not satisfy the Walen test have been inspected by hand for substructure and included in the survey *ad hoc* where appropriate.

Chapter 4

Survey of Voyager 2 reconnection events

We have applied the automated detection process described in Chapter 3 to the Voyager 2 interplanetary mission and identified 138 reconnection exhaust crossings in the solar wind. To date, this list of events constitutes more than 60% of all reconnection observations in the solar wind beyond 1 AU. Fifty-eight of these events occurred after the Jupiter encounter, constituting a unique data set at heliographic radii not previously considered for such a purpose. In this chapter, the results of the full survey are presented in detail. A statistical description of the physical characteristics of reconnection signatures and the plasma environment in which they are found is given, and this description is compared to the reconnection landscape observed by Ulysses [35].

4.1 Overview of Voyager 2 survey results and statistics

The times and locations of all Voyager 2 reconnection exhaust encounters are shown in Figure 4.1. In approximately the first six months of the mission, when high-resolution plasma data were obtainable, short-duration reconnection events of less than 96 seconds were observed at a rate of approximately one per 3.5 days. In all, 32 such events were observed before the PLS integration time was increased to 96 seconds in March, 1978. Adjusted according to the data coverage on that interval, the the actual rate of occurrence is ~ 0.6 events per day near 1 AU. We first compare this occurrence rate to published studies of Wind data under similar conditions at 1 AU. Two separate studies of reconnection with the Wind and ACE spacecraft near solar minimum have reported typical observation rates of ~ 1.3 events per month at a 64-second cadence, and as many as ~ 1.5

events per day at a 3-second cadence, respectively [37]. The initial observation rate from this study is compatible with these published rates at 1 AU. In a study of reconnection exhausts with Ulysses between 1.4 AU to 5 AU, events were observed at a rate of ~ 0.5 per month with a cadence of 4 minutes[35]. Over that range of heliographic radii, Voyager 2 observed seven exhausts with traversal times of greater than 4 minutes, also corresponding to a rate of ~ 0.5 per month.

For this study to be compared statistically to other independent studies, it is important that each study agrees on what constitutes a reconnection exhaust signature and to what extent these signatures can be distinguished from background. The fact that we have observed exhaust signatures at similar rates under similar conditions suggests a satisfactory consensus on this subject. The validity of our parametrization and search procedure is supported by the broad agreement of detection rates at well-separated timescales.

Eighty reconnection exhausts were observed in all from 1 to 5.4 AU. After the Jupiter encounter, an additional fifty-eight exhausts were observed in the outer solar system, nearly all at the 192-second plasma cadence. All of these events occurred in the slow wind, though thirty occurred in streams clearly perturbed by corotating stream interactions or coronal mass ejections.

Figure 4.1 shows that while the number of reconnection exhausts observed decreased with distance, the occurrence rate for large events (several minutes or greater) did not depend strongly on distance from the sun. For distances larger than about 15 AU, the interplanetary cruise speed and total data coverage remained roughly steady. In this time period, there were no events observed between 15 and 20 AU. A drop in 192-second coverage occurred in 1985, between 16-18 AU, yet the restoration of data coverage did not immediately coincide with the return of reconnection structures. It is difficult to ascertain the correspondence with data resolution, if any, at larger distances because the number of events there is small. It does appear, however, that there is a correspondence between magnetic reconnection in the outer solar system and solar activity.

The lower panel of Figure 4.1 shows a representation of solar activity relevant to the position of Voyager 2. This plot shows the International Sunspot Number [87], binned by month and delayed by the convection time, $\tau_{conv} = \langle u_R \rangle / R$. This number is a proxy for the degree to which solar weather may be disrupting the quiescent solar wind at Voyager 2. Suggestively, the period from 15 to 20 AU, over which no exhausts were observed, coincided with the convected solar minimum. The decline and return of reconnection around this period also seems to have coincided with the decline of solar activity to minimum and the rising phase of the next solar cycle. Long-duration exhaust signatures were most frequent near both solar maxima, and were most commonly found at s and in ICMEs, phenomena that are more common near solar maximum. When the occurrence rate of large events is divided by the appropriate rate of data coverage and the smoothed sunspot number, there is no remaining trend

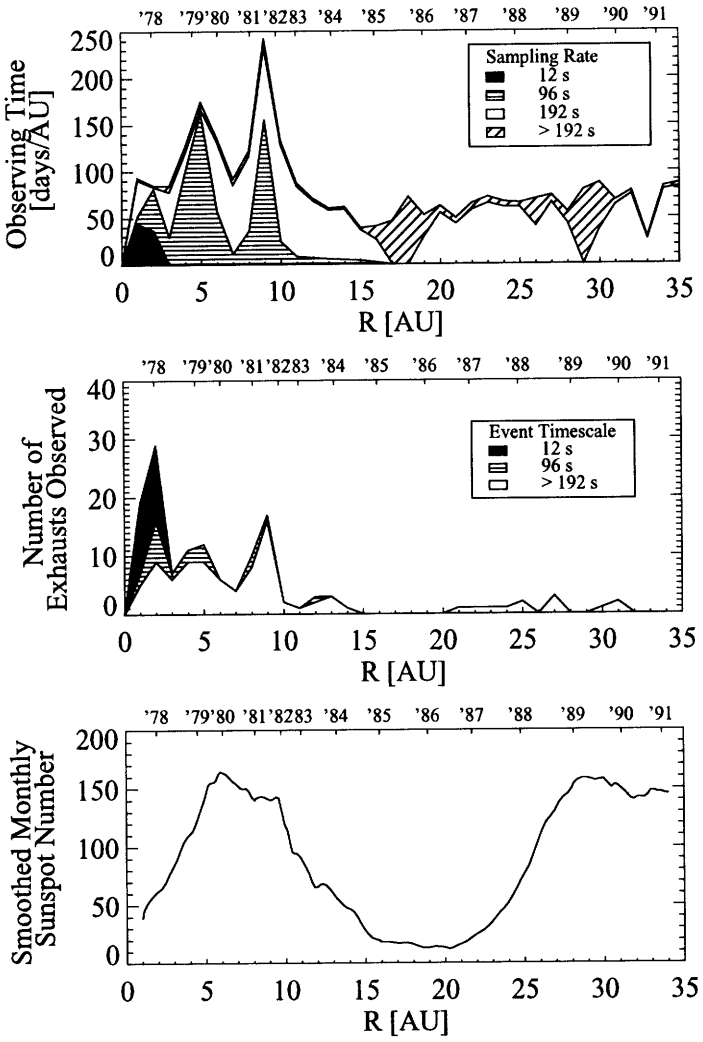

Figure 4.1: Voyager 2 reconnection survey results. Each plot shows Voyager-Sun distance on the lower x-axis and the corresponding year on the upper x-axis. **Top panel:** data coverage is plotted as a function of heliospheric distance for the three primary PLS instrument integration times. **Second panel:** reconnection exhausts observed as a function of radius for the events that could be identified at the associated timescales. **Lower panel:** the sunspot number, adjusted to reflect the time of origin for the solar wind at Voyager 2. The corresponding observation year is shown across the top of each plot.

of statistical significance to be found.

4.1.1 Exhaust Geometries

Using the conventions of Chapter 3, let $\langle \mathbf{v} \rangle_\mathbf{e}$ and $\mathbf{u}$ denote the average plasma velocity in the reconnection exhaust and in the inflow regions, respectively. For each event, the exhaust flow direction is defined as direction parallel to $\langle \mathbf{v} \rangle_\mathbf{e} - \mathbf{u}$. Figure 4.2 plots the outflow direction of each event on the unit sphere and shows histograms of the in-plane and inclination angles. These histograms are stacked according to the data cadence, showing the relative contributions of the three major survey components depicted in Figure 4.1. Outflow directions are distributed broadly on the unit sphere, spanning the full range of inclinations to the ecliptic plane.

Outflow longitudes are plotted in Figure 4.2 relative to the Parker angle in order to illustrate the tendency for reconnection exhausts on all scales to be aligned with the global configuration of the magnetic field. The Parker angle is the in-plane angle of the streamline one calculates by assuming that the solar wind takes a ballistic trajectory from some source surface near the sun, and that the magnetic field of the solar wind is frozen-in. For an event detected at heliographic radius R, in a stream with bulk flow speed u_R, the Parker angle, ϕ_{Parker}, is given by

$$\tan \phi_{Parker} = \frac{\Omega R}{u_R}, \tag{4.1.1.1}$$

where Ω is the rotation rate of the sun at the equator, approximately equal to $2\pi/27.3$ radians/day.

The statistical alignment of reconnection outflows with the Parker spiral suggests that a significant subset of our survey is associated with reconnection of a broadly symmetric, global magnetic field. Perhaps the simplest configuration that could be envisioned for simple, laminar reconnection on a large scale in the solar wind would be at the interface of outward-oriented and inward-oriented field lines on the Parker Spiral. Were this configuration to be the dominant reconnection geometry in the solar wind, the distribution of $\phi_{outflow} - \phi_{Parker}$ would be sharply peaked at 0° for crossings sunward of the x-line and 180° for crossings anti-sunward of the x-line. This stands in contrast to the strongly turbulent picture of reconnection, such as that portrayed in Figure 2.5c. The presence of substructure in the magnetic field would isotropize the distribution of $\phi_{outflow} - \phi_{Parker}$. Reconnection in the magnetic substructure of ICMEs might also be a source of outflows that are not Parker-aligned. The broadly double-peaked distribution in Figure 4.2 supports the interpretation that a combination of these scenarios is at work on all three of the event timescales shown.

A roughly equal number of sunward and anti-sunward outflows are observed at all three resolutions. This suggests that reconnection x-lines were generally present upstream and downstream of the spacecraft in equal proportion,

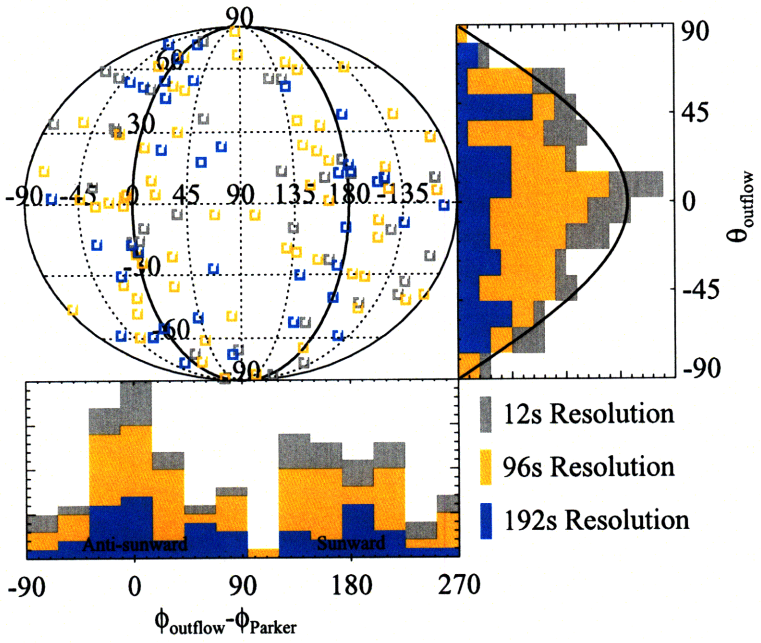

Figure 4.2: Exhaust flow orientations relative to the Parker angle. The data resolution for each event is signified by the color: grey for 12-second cadence, orange for 96-second, and blue for 192-second. **Upper-left panel:** scatter plot of outflow angles in Mollweide projection with the anti-sunward Parker angle at 0° longitude and the sunward Parker angle at 180° longitude. **Upper-right panel:** histogram of the flow inclination angle, the angle between each outflow vector and the solar heliographic plane. The solid line indicates an equal-area distribution of $\theta_{outflow}$. **Lower-left panel:** histogram of the in-plane flow angle, relative to the Parker spiral.

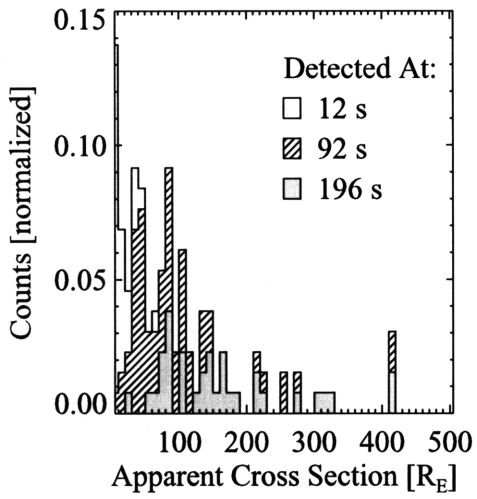

Figure 4.3: Distribution of estimated exhaust cross sections, in units of Earth radii. The components of this stacked histogram are filled in solid white, diagonal hashes, and solid grey to represent events observed at the 12-second, 96-second, and 192-second PLS resolution, respectively.

consistent with the previous observation that occurrence rate is not strongly dependent on heliographic radius. A similar symmetry between sunward and anti-sunward exhausts has been reported elsewhere at various distances [35, 34, 39].

The distribution of inclinations relative to the solar heliographic plane is roughly isotropic. In the upper-right panel of Figure 4.2, the distribution of inclination angles is shown for each of the data resolutions, with the isotropic distribution over-plotted. While the overall outflow distribution is consistent with isotropy, there is weak evidence that exhausts aligned with the plane tend to be thinner than exhausts with large inclination. The 192-second component of the $\theta_{outflow}$-distribution is flatter than the isotropic curve, whereas the 96-second and 12-second distributions are more sharply peaked at $\theta_{outflow} = 0$.

In the limit that each exhaust structure evolves on a timescale much longer than the timescale of the observation, we can convert the traversal time, Δt, directly to the apparent cross-sectional distance, $d \approx \Delta t/u$. Assuming that deformations to the structure propagate no faster that the Alfvén speed, the actual cross-sectional distance is approximately constant and equal to d over the duration of the observation as long as the solar wind is strongly super-Alfvénic. As noted in Section 2.2.3, this is usually a very good approximation.

Without knowing anything about the spatial configuration of the discontinuities that bound the exhaust region, we can take d to be an upper bound

on the width of the outflow jet. The smallest of the exhaust jets in this study was observed at 1.4 AU. This event was no greater than 3.3 earth-radii across, a distance that is more than two orders of magnitude larger than the associated ion inertial length. The potentially largest event, which occurred at 13.7 AU, was no greater than 0.15 AU across. The median value of d was 78 earth-radii.

The apparent cross sections for the entire survey are histogrammed in Figure 4.3. These events are broadly distributed by orientation, as shown in 4.2, so this distribution of d is broadened out to large distances relative to the distribution one would expect for the actual cross-sectional width of exhaust-wedge structures. The smallest event scales shown are obviously strongly coupled to the data cadence at the time of observation. There is no apparent preferred scale, except that the occurrence rate is generally a decreasing function of d.

The exhaust flow angle provides a good estimate of the angle-of-incidence that the effective spacecraft trajectory makes with the exhaust. If the opening angle of the exhaust wedge is small, the actual width, χ, of each exhaust is approximately given by

$$\chi \approx d \cos\theta_{outflow} \cos\phi_{outflow}. \qquad (4.1.1.2)$$

The number of exhausts observed is also a strongly decreasing function of χ, with typical event scales in the range of 1-100 Earth-radii. These estimates place the entire survey squarely in the fluid limit, with $\chi \gg \lambda_{c,i}$ in all cases. In a scenario where reconnection occurs primarily in turbulent current sheets, one would expect a negative power law scaling of the size distribution $P(\chi)$ to reflect the scaling of the plasma substructure that drives it. The event size data does not rule that sort of scenario here, but the measured distribution is strongly entangled with effects from the different data rates, the angular bias towards the Parker spiral, and the particular selection of bulk flow speeds associated with the quiescent slow wind, ICMEs, and stream interaction regions.

The magnetic field shear angle is histogrammed in Figure 17. In this plot, 180° corresponds to fully anti-parallel reconnection, which is the geometry of the theoretical models presented in Chapter 2. At very low field shear angles, the system undergoes "component reconnection." In that case, there is a significant parallel component of the magnetic field between reconnecting flux tubes, called the "guide field." Reconnection exhausts have been observed in this study at both extremes and everywhere in between. Reconnection at large field shears is slightly favored: the mean field shear for the survey is about 100°. Our survey is, however, quite naturally biased towards large changes in the field. Recal from Section 3.3 that the weights $q_{\mathbf{cA},1}$ and $q_{\mathbf{cA},2}$ are directly proportional to the vector change in the magnetic field. Amidst a similar level of background fluctuations, then, events with high field shear will more frequently satisfy the acceptance criterion $q_{\mathbf{cA}} > n_{min}$.

There are other systematic reasons to expect a higher detection rate at large field shears. For equal strengths of the total magnetic field, for example,

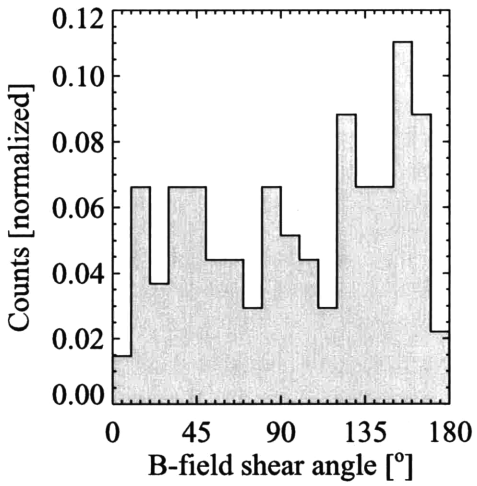

Figure 4.4: Distribution of the local magnetic field shear across the observed reconnection exhausts.

high-shear events convert a greater portion of the magnetic energy to accelerate and heat the outflow jet. Thus high-shear events would be expected to produce stronger outflows and higher values of q_v and again higher detectability.

When we consider the relatively flat distribution of field shear angles in this survey along with the increase in occurrence rate at small sizes, we are lead to believe that there may be a large number of small, low-shear reconnection events that have escaped our detection. This interpretation is supported by a recent examination of small-scale reconnection at 1 AU by Gosling and his co-authors[37], in which a large number of short-duration, low shear exhaust events were observed at near-gyro-scale resolution over one month of slow wind data.

4.1.2 Proton plasma-β

Over the full interplanetary mission, the hourly average of the proton plasma parameter, β_i, varied by more than five orders of magnitude. The overall median value, $\beta_i \approx 0.13$, is close to that of the typical plasma environment local to a magnetic reconnection exhaust. The median value of β_i in reconnection inflow regions was about 0.19. Figure 4.5 shows the distribution of inflow betas along with the full solar wind distribution. Events were found in a large range of plasma environments, between $\beta_{i,min} = 4 \cdot 10^{-3}$ and $\beta_{i,max} = 4.5$, with no discernible critical behavior.

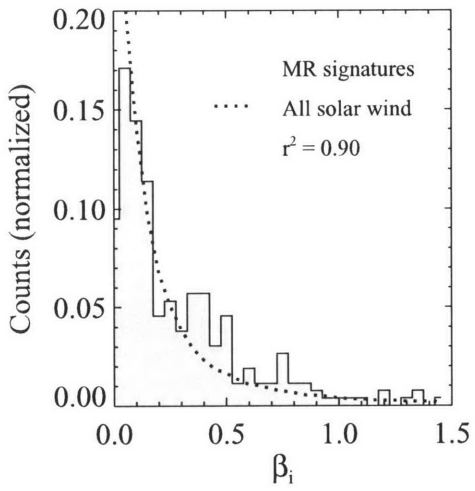

Figure 4.5: The local proton plasma-β values for each event. Shown in grey is a normalized histogram of the average plasma beta in each upstream and downstream region. The dotted line shows the plasma beta distribution for the solar wind over the entire study. These two distributions have a correlation coefficient of $r^2 = 0.90$, indicating that the plasma found local to reconnection outflows is representative of the typical solar wind.

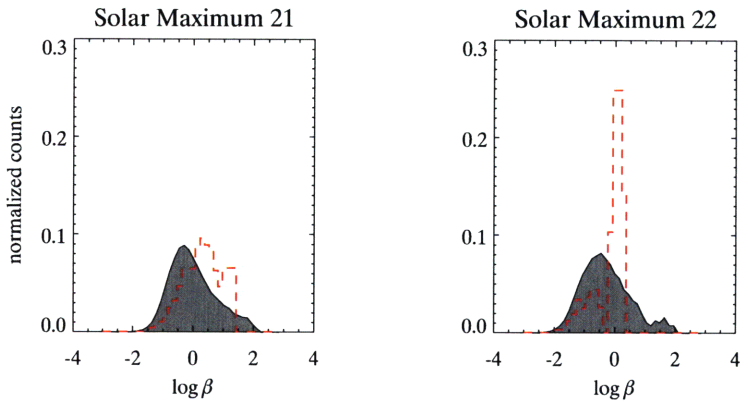

Figure 4.6: Logarithmic distributions of the proton plasma-β over solar maxima 21 and 22. Filled grey distributions represent all solar wind data over the most active three-year period of each cycle. Red dashed distributions show the proton plasma-β measured near the corresponding events.

The distribution of inflowing β_i is similar to that of the solar wind as a whole. The two distributions shown in Figure 4.5 have a correlation coefficient of 0.9. It is apparent, however, that the inflow distribution favors elevated β_i. In order to quantify that tendency, we can apply the Kolmogorov-Smirnov test to compare these two sets of β_i [74]. This test compares the cumulative distribution functions of the two sets, under the hypothesis that the two sets are sampled randomly from a common parent PDF. The Kolmogorov-Smirnov statistic, which is the maximum deviation between the two cumulative distribution functions, approaches zero when that hypothesis is true. For $\beta_{i,inflows}$ and $\beta_{i,all}$, the Kolmogorov-Smirnov statistic is $+0.16$. This deviation corresponds to a calculably minuscule 1-in-10^6 probability that the common PDF hypothesis is correct.

Based on this probability, one might hypothesize that the reconnection of solar wind current sheets occurs preferentially when β_i is relatively high. That hypothesis would contradict the assertion of several authors that reconnection tends to occur at low β_i [35, 34, 39]. We note, however, that the average β_i in the solar wind increases with solar activity and decreases with distance from the sun. This distribution could be biased, then, because the Voyager 2 events occurred preferentially close in and near solar maximum.

Figure 4.6 shows distributions of β_i for the solar wind and for reconnection inflows, both restricted to the ascending and maximum phase of the solar cycle. Over each of these periods, the monthly average and median value of the plasma beta was approximately constant. The inflow distributions in each case are, again, shifted towards higher β_i. At the maximum of cycle 21, the

Kolmogorov-Smirnov statistic is +0.19, corresponding to a 1-in-10^4 probability that the two curves are derived from the same PDF. At the maximum of cycle 22, the number of exhausts is not high enough for the two distributions to be compared with confidence. The calculated probability of a common PDF is ~ 0.3. In both cases, the median and mean of $\beta_{i,inflows}$ exceed the values computed for $\beta_{i,all}$.

This result runs contrary to the assertion that reconnection tends to occur at low β_i made in numerous publications. It is clear that reconnection does frequently occur when $\beta_i < 1$ and even $\beta_i \ll 1$ in the Voyager 2 data, and that these regimes are often referred to as "low-beta." It would be incorrect, however, to infer from this that the likelihood of observing an exhaust structure is inversely related to β_i. Based on these findings, we assert that reconnection in the solar wind preferentially occurs at elevated β_i.

4.1.3 Independence of events

As we have discussed in Section 3.3.4, this survey is biased against detections of multiple adjacent reconnection exhausts or repeated crossings of the same exhaust. The reason for this bias is the requirement that each signature include a quiet upstream and downstream region of comparable size. If, for any given exhaust signature, there is a second signature overlapping one of those regions, that exhaust is more likely to be excluded than if it were isolated.

In spite of this bias, certain reconnection events have been observed in close groupings. In three separate cases, multiple events were observed within two minutes of each other. In three other cases, apparent double-crossings or compound exhaust structures were discovered by the algorithm. In those cases, the event catalogue was corrected by hand to include both signatures separately. Most events, however, were well-isolated. The mean waiting time between events was about eight days in the early, high-resolution segment of the mission. The median waiting time, however, was only four days. This fact is suggestive, but not sufficient to indicate that the overall probability of observing a reconnection time signature is higher if another signature has been recently observed. In general, a large preponderance of short waiting times could indicate that reconnection exhausts occur in bunches.

The waiting time distribution provides an indicator of the independence of reconnection events. The distribution of times between Voyager 2 events is shown in Figure 4.7, on a logarithmic scale in days. The counts in the plot are re-scaled according to logarithmic binning, and the error bars shown on the plot are from the Poisson counting uncertainty. Noting that the longest event durations in this survey are less than one day and that about 90% of events are between 1 minute and 1 day long, the survey bias against grouped events should be manifest in that range in Figure 4.7.

Figure 4.7 does not exhibit a strong cutoff at short times. The rollover feature in Figure 4.7 between 0.1 and 1 days may be due to the survey bias effect.

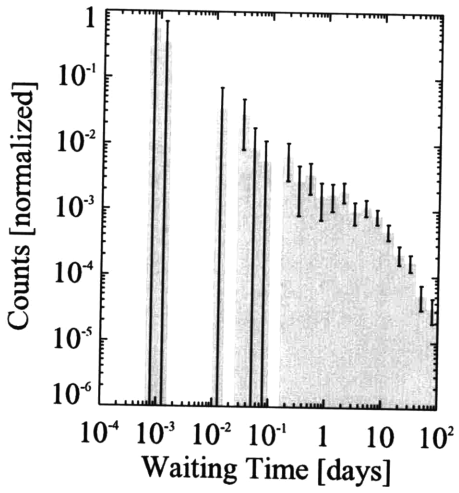

Figure 4.7: Logarithmic distribution of the waiting time, in days, between reconnection exhausts. The error bars shown are $\pm 1/\sqrt{N_{counts}}$.

For waiting times greater than 1 day, the data support that the distribution is unbiased. On that timescale, we can attempt to answer the question of whether exhaust events occur independently.

The waiting time distribution for a collection of independent events, i.e. a Poisson process, is an exponential function. The distribution for a set of correlated events might be more sharply peaked and containing more counts in the tails, by contrast. Once again, we can use the Kolmogorov-Smirnov test- this time to determine whether this distribution is consistent with an exponential, "memoryless" distribution of events. Early-mission events ($R < 10$ AU) were selected in the two upper decades of the waiting time distribution, accounting for 91 events. That subset was further reduced to 70 events that were detectable at the 96-second cadence in order to minimize the data rate variation. The resolution sub-distribution was fit to an exponential function using least-squares minimization. The fit exponential takes the form

$$F(t) = \lambda e^{-\lambda t},$$

where $\lambda \approx 0.04$ events per day is the nominal occurrence rate. The Kolmogorov-Smirnov statistic comparing the data to the fit distribution is 0.4, corresponding to a 6% probability that these reconnection events are a Poisson process.

This result confirms what we had already suspected: that reconnection

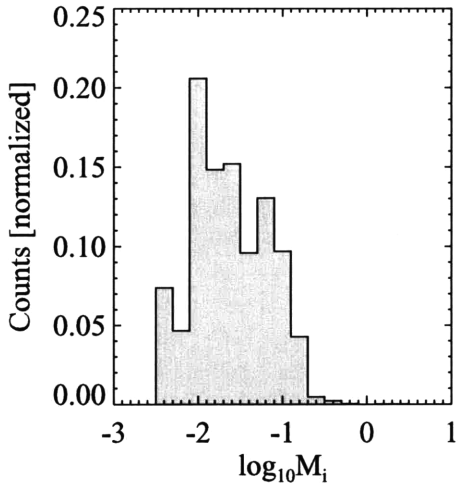

Figure 4.8: Distribution of the dimensionless reconnection rate, $M_i = v_{in}/c_A$ for Voyager 2 exhaust events.

occurs preferentially under certain conditions that are not themselves Poisson processes, such as CIRs or ICMEs. The continued trend at waiting times shorter than 1 day is suggestive of more interesting correlated behavior, such as multiple reconnection in regions with plasmoidal substructure. That behavior is not quantifiable, however, without significantly better statistics to remove any rollover near the resolution limit of the detection algorithm.

4.1.4 Reconnection Rate

In Section 2.2.3, we defined one representation of the dimensionless reconnection rate, M_i, for a Sweet-Parker current sheet to be equal to the Alfvén Mach number of the plasma flowing into the reconnection site. In the Petschek theory, a small, flow component is introduced across the inflow far from the reconnection site. As long as this Petschek component is small compared to the true inflow, the Alfvén Mach number that is measured far from the reconnection site is an accurate representation of the reconnection rate. Figure 4.8 shows the logarithmic distribution of M_i for the Voyager 2 survey.

Priest and Forbes have defined the "slow" and "fast" reconnection regimes relative to the magnetic Reynolds number of the system. As we showed in Section 2.2.3, slow reconnection via the Sweet-Parker mechanism proceeds at a rate $M_i \leq R_m^{-1/2}$. Fast reconnection is said to occur when $M_i > R_m^{-1/2}$. Based on our results, all of the observed reconnection exhaust events should be

considered fast as long as the magnetic Reynolds number is greater than about 10^4. The magnetic Reynolds number for any measurably large feature of the solar wind surpasses that value by several orders of magnitude.

The accuracy to which we can measure M_i is limited primarily by the strength of the inflow relative to velocity fluctuations. This accuracy limit effectively guarantees that "slow" magnetic reconnection rates cannot be measured for any realistic variance, $\langle \delta \mathbf{v}^2 \rangle$. Nor, in fact, could they be measured for any realistic integration time with the PLS experiment, even in the absence of variance, as a consequence of the Faraday Cup current quantization. It is not surprising, then, that all of the exhausts shown in Figure 4.8 are in the fast reconnection regime.

The range of observed values of M_i in this survey is $M_{i,min} \approx (5 \pm 4) \cdot 10^{-3}$ to $M_{i,max} \approx 0.8 \pm 0.4$. In two exceptional cases, the estimated reconnection rate was greater than unity, indicating super-Alfvénic driving at first glance. In both of those cases, however, there was a substantial converging component of $\mathbf{v}$ along the reconnecting field. Assuming that we are still correct to interpret these as quasi-2D structures, the additional flow component constitutes a large velocity shear across each exhaust. For a strong enough velocity shear ($\Delta v_{\parallel} \gtrsim 2c_A$), the reconnection interface is unstable to the Kelvin-Helmholtz (KH) instability [68]. A KH-unstable interface will develop curvature of the field as vortices grow, ultimately creating a turbulent mixing layer wherein the magnetic field turns back upon itself many times. These discontinuities cannot be considered static, and are unlikely to have translational symmetry on a large scale.

4.1.5 Dynamic timescale

In the Petschek model, slow shocks are initially formed at the x-line and extended outwards with the assembly of the Alfvénic jet. In general, any self-organized equilibrium configuration for the system is expected to develop on an Alfvénic timescale. That timescale can be estimated for each exhaust jet under the usual assumption that the local inflow plasma parameters are representative of the entire system.

The magnetic field shear angle for a slow-mode shock pair is equal to the opening angle of the shock wedge in the limit of switch-off shocks. For oblique shocks, as depicted in Figure 2.3, the field shear angle is greater than the opening angle. We can exploit this property of the Petschek model to estimate a lower bound on the length of the exhaust from the x-line to the spacecraft crossing:

$$L_{min} \approx \chi / \tan(180^\circ - \alpha_B),$$

where α_B is the magnetic field shear angle. We can also put a lower bound on the formation time of the structure based on the Alfvén timescale assumption

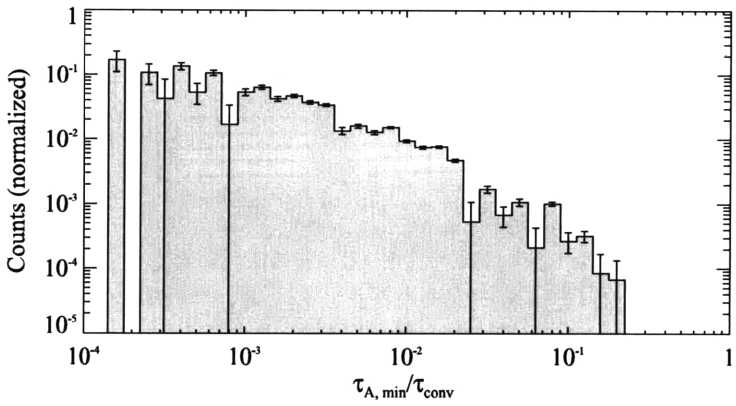

Figure 4.9: Distribution of Alfvénic structure formation time, relative to the convection time, of reconnection exhausts. For each exhaust, a lower bound on the Alfvén crossing time is estimated from the field shear angle and the cross section. This timescale is expressed on the x-axis as a fraction of the total time-of-flight for the local solar wind. The error bars shown are $\pm 1/\sqrt{N_{counts}}$.

$$\tau_{A,min} \equiv \frac{L_{min}}{c_A}.$$

In Figure 4.9, this timescale is compared to the total convection time for each event, τ_{conv}. The convection time is defined as the total time of flight for the solar wind to reach the point of observation:

$$\tau_{conv} \equiv \frac{R}{u_R}.$$

The binning in Figure 4.9 is logarithmic, and the distribution is rescaled according to bin size and renormalized. There are two contributions to the error bars shown in this Figure. First, measurement errors associated with τ_A/τ_{conv} are propagated from the standard deviations of $\mathbf{B}$, $\mathbf{v}$, and n over the upstream and downstream regions and translated into binning error. Second, the counting error per bin, $1/\sqrt{N_{counts}}$ is added in quadrature. The latter component is the dominant source of error.

The formation timescale for Voyager 2 events is typically much less than the convection time. The median value of the formation timescale is $\sim 0.007 \cdot \tau_{conv}$, and the median value is $\sim 0.02 \cdot \tau_{conv}$. The distribution of events is a decreasing function of the ratio τ_A/τ_{conv}, reflecting the similar distribution of cross-sectional sizes.

Timescale ratios that are greater than unity have unphysical implications for quasi-steady reconnection. An event that exhibits $\tau_A > \tau_{conv}$ develops more slowly than the convection of the solar wind to the spacecraft. Thus, it appears to require onset of reconnection *before* the solar wind is launched from the sun in order to be in equilibrium when observed. This is the case for one event in the Voyager 2 survey. That event, which is also one of the events presumed to be KH-unstable in Section 4.1.4, has a measured magnetic field shear of $159° \pm 19°$. It is very likely that, in this case, the outflow region has been significantly deformed by the instability. If the instability has created small-scale ripples at the exhaust interfaces, the field shear that is measured is not representative of the exhaust as a whole. If the instability has created a large-scale change in the structure, the exhaust jet may be curled. As the interface curls with the action of the instability, it also stretches out, which naturally drives the shear angle towards 180°.

The timescale ratio is less than 0.22 for all other Voyager 2 events. The distribution is consistent with the quasi-steady, slab-symmetric picture for reconnection structure that is established *in situ* in the solar wind. The increase in event frequency with decreasing τ_A/τ_{conv} is suggestive of a large number of small, short-lived structures below the detection threshold. It also suggests that reconnection onset can take place at large distances from the sun.

4.1.6 Exhaust energetics

The equilibrium of any convecting solar wind structure requires balance of pressures across that structure. The full equilibrium of most structures cannot be confirmed by Voyager 2 because changes in the electron component of the plasma cannot be measured. There is evidence, however, to confirm that the compression and heating of protons in these events occurs in direct response to the conversion of magnetic energy via reconnection.

The response of the proton population is shown in Figure 4.10. In most cases, the ion component of the plasma is significantly compressed and/or heated in the exhaust relative to the inflow region. Exhaust-like structures with $\Delta p_i < 0$ were excluded from the survey, however, so a spurious increase is expected, on average, even for a random sample of events with no reconnection or shock heating process occurring. We can estimate the spurious increase, which we write $\langle \Delta p_i \rangle_0$, as being on the order of the the observed standard deviation of the scalar proton pressure in the exhaust.

$$\langle \Delta p_i \rangle_0 \approx \sigma_{p_i,e}$$

This error is less than half of the measured Δp_i for all of the Voyager 2 events. On average, it is true that

$$\langle \Delta p_i \rangle_0 \lesssim 0.1 \cdot \Delta p_i.$$

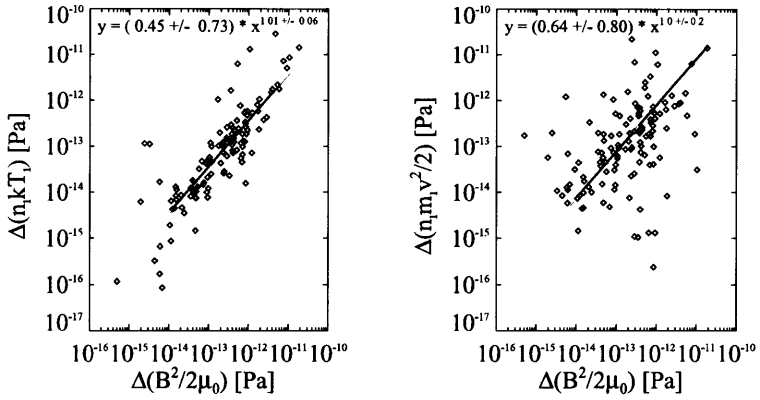

Figure 4.10: Conversion of magnetic energy in reconnection exhausts. **Left panel:** The increase in the [scalar] proton pressure is plotted against the magnitude of the decrease in magnetic field pressure in SI units. **Right panel:** The kinetic energy density of the exhaust is plotted against the magnitude of the decrease in magnetic field pressure. The power law regressions shown are consistent with compressive Sweet-Parker scaling, wherein the energy density associated with the reconnecting field is converted in equal parts to outflow kinetic energy and heat.

We can be confident, then, that the measured increases in ion pressure are significant. The left panel of Figure 4.10 shows the pressure change as a function of the change in the magnetic energy density, shown here in SI units $\Delta B^2/2\mu_0$. Also shown is the power law of best-fit, calculated from the maximum likelihood method assuming a power law distribution for the data [74]. The fit exponent is found to be 1.01 ± 0.06, which is consistent with a linear correspondence, $\Delta n_i k T_i \propto \Delta B^2/2\mu_0$. The coefficient is found to be $0.45^{+0.98}_{-0.33}$, which is loosely consistent with a net pressure balance.

The right panel of Figure 4.10 shows the kinetic energy of the reconnection outflow, also as a function of the magnetic energy density. There is a considerable scatter in this relationship, but we see that the energization of the outflow is also an increasing function of $\Delta B^2/2\mu_0$, with a roughly constant proportionality. The most likely scaling exponent is found to be 1.0 ± 0.2, with a coefficient of $0.64^{+1.10}_{-.26}$. The similar magnitude and scaling of outflow kinetic energy and thermal energy suggests an equipartition of the inflowing magnetic field energy between the two components.

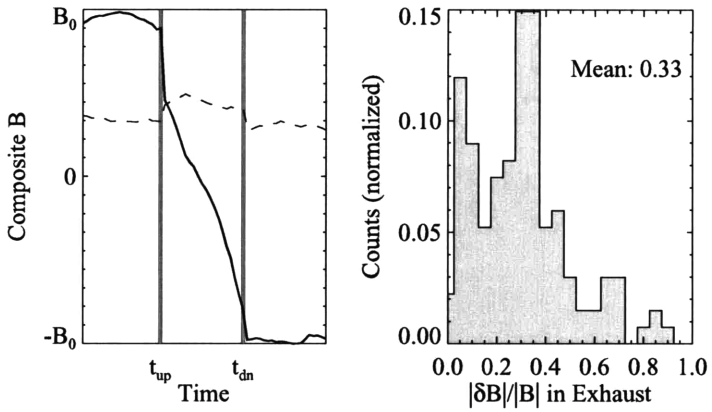

Figure 4.11: Ensemble of reconnection magnetic field signatures. **Left panel:** a composite of the magnetic field time signatures for all reconnection events, in the reconnection plane. The solid line indicates the field component in the [best-fit] outflow direction, and the dashed line indicates the component in the inflow direction. Vertical bands indicate the upstream and downstream exhaust boundaries. **Right panel:** histogram of the field fluctuation strength in the exhaust region.

4.2 Structure of the exhaust profile

Consider the symmetrical reconnection models presented in Chapter 2, and the associated idealized time signature illustrated in Figure 3.4. The signatures of $\mathbf{B}(t)/B_0$ and $\mathbf{v}(t)/v_0$ in the reconnection-plane projection, where B_0 is the reconnecting field strength and v_0 is the outflow speed, are scale-invariant. In this section, we would like to characterize the exhaust signatures observed by Voyager 2 relative to those idealized models.

4.2.1 The composite magnetic field profile

The left panel of 4.11 shows a composite of the reconnection-plane components of $\mathbf{B}(t)$. For this figure, each time series is re-scaled to align the upstream and downstream boundaries. The magnetic field vectors are then re-obtained at the highest available resolution from the original MFI data set, and re-sampled to linear interpolates on a grid of thirty elements. The figure shows the sum of those interpolates. The grid size is chosen to preserve as much structure as possible while minimizing up-sampling for the shortest-duration events.

Figure 4.11 demonstrates several properties of the typical exhaust signature observed by Voyager 2, which will now be discussed in turn.

Field rotation and discontinuities

The reconnecting component of the field is sharply discontinuous at the exhaust boundaries, t_{up} and t_{dn}, but it is not generally constant across the exhaust. The slow rotation of the field across the outflow region indicates that, on average, the field lines across the outflow are curved and convex to the exhaust wedge. The slow decrease and rotation of the field approaching the center of the exhaust accounts for more than half of the total change in **B**.

The mean change in the reconnecting component of the field between the grid locations immediately upstream and downstream of each discontinuity is $\sim 0.3 \cdot B_0$. If the discontinuities at t_{up} and t_{dn} are shocks, they are weaker than prescribed by the basic Petschek schematic by more than half. To accurately estimate shock normals for these structures, one would have to take into account the likelihood that the average **B** in the exhaust is not representative of the field immediately adjacent to the shock.

Also notable is the profile of the normal component of the field. Petschek theory predicts that there must be a small non-zero normal component of the magnetic field across the exhaust. This component increases in the immediate vicinity of the exhaust where the field bends away from the shock normals. The normal component of the composite B-field is shown with a dashed line in Figure 4.11. The strength of the normal component is $\sim 0.3 \cdot B_0$ outside of the exhaust, and increased by $\sim 0.15 \cdot B_0$ at the exhaust.

Substructure in the B-field

The right panel of Figure 4.11 illustrates the level of magnetic substructure in the Voyager 2 events. For each event, the first-, second-, and third-order trends in the field strength are fitted for and removed. The rms magnitude of residual fluctuation in **B** is calculated and included in the histogram. These fluctuations are frequently a significant fraction of the total field, with $\delta B / B_{exhaust}$ averaging 0.33, and falling between 0.1 and 1 in 80% of all events. This is an indication that the outflow is weakly substructured, whether by turbulence in the flow or by unsteadiness in the reconnection process.

4.2.2 The composite flow profile

The left panel of Figure 4.12 shows a composite of the reconnection-plane components of $\mathbf{v}(t) - \mathbf{u}$, constructed from event velocity data in the same way as Figure 4.11.

Flow geometry

The solid line in Figure 4.12 shows the speed of the reconnection jet, which is sharply confined by the two discontinuities. The typical reconnection exhaust

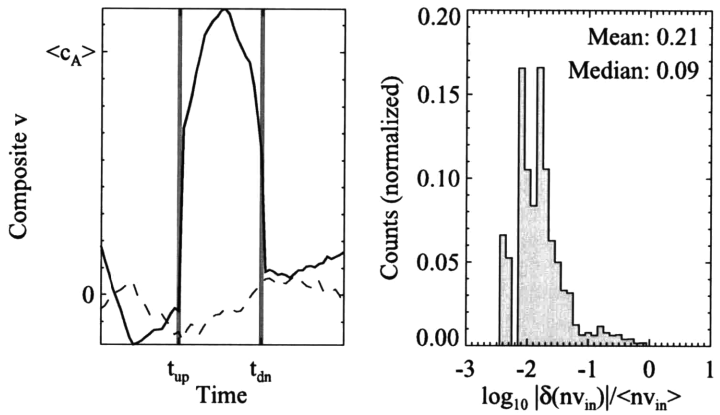

Figure 4.12: Ensemble of reconnection velocity signatures. **Left panel:** a composite of the velocity time signatures for all reconnection events, in the reconnection plane. The solid line indicates the component in the [best-fit] outflow direction, and the dashed line indicates the component in the inflow direction. Vertical bands indicate the upstream and downstream exhaust boundaries. **Right panel:** histogram of the compressive fluctuation strength in the inflow regions.

is indeed Alfvénic as we expect- the mean Alfvén Mach number for all Voyager 2 events, as compared to the average Alfvén speed in the inflow region, is 1.01 . The outflow speed is not constant across each jet. The composite jet speed jumps by an initial $0.6 \cdot c_A$ immediately across each discontinuity and peaks at about $1.2 \cdot c_A$ at the center.

The normal velocity component is shown in with a dashed line in the left panel of Figure 4.12. In the exhaust region, a small component runs counter to the inflow direction, away from the center of the exhaust. Thus the composite jet is fanned along the wedge rather than uniform throughout. A fanned, laminar outflow in the composite is self-consistent with the convex curvature of the frozen-in B-field described in Section 4.2.1. It possible that some of these exhaust traversals occur in a regions where the jet is colliding with unperturbed plasma. The attenuation of the jet and bending of the field near the boundaries could indicate in those cases that the wedge is in a process of forming or dissipating. It is also possible that the opening angle of the exhaust increases with distance from the reconnection site.

The typical flow profile includes a significant velocity shear in the inflow. Note the asymmetry in the component parallel to the jet across the inflow regions. The composite shows that velocity shear is typically present with an average Mach number of about 0.1. This shear is far below the Kelvin-Helmholtz

instability limit, but it is interesting to note that the shear component is frequently comparable to the inflow itself.

We also note that the composite velocity profile does not indicate any significant lateral diversion of the flow in the inflow region. In Petschek's model the deformation of the field just upstream and downstream of the exhaust wedge requires a perturbation to the inflow along the exhaust direction. This perturbation should be an even function of the distance from the exhaust mid-plane. No such perturbation is observed. Instead, the non-idealness of the inflow is dominated by the [odd] shear contribution.

Compressive substructure in the inflow

The right panel of Figure 4.12 illustrates the level of compressive variation in the Voyager 2 event inflows. This distribution shows the relative occurrence rate of different rms fluctuations in the flow momentum into the exhaust. Steady reconnection can only occur under steady driving conditions, so this fluctuation level is a strong indicator of the plausibility of the quasi-steady reconnection assumption. Half of the Voyager 2 events exhibited inflow momentum fluctuations of less than 10%, while the mean fluctuation level was about 20%. For nineteen signatures, the fluctuation level was on the order of the net inflow momentum itself. In those cases, the compressive variation of the driving must have a non-negligible effect on the exhaust geometry. Those structures cannot be considered stationary.

4.3 Discussion

The reconnection landscape that emerges from our survey indicates that large-scale, steady-state exhausts do occur in the solar wind and persist out to large distances. There is no evidence to suggest that reconnection effects occur preferentially near the sun or at any particular distance from it. It is naturally expected that as the solar wind mixes and relaxes at large distance, a state of minimal magnetic free energy is achieved and these processes die down. We are unable to verify, however, if that slowdown has occurred out to 31 AU. The behavior of the event distributions at short timescales and spatial scales, however, gives us strong reason to suspect that we are examining only the "tip of the iceberg." There is every indication that a great deal more reconnection-associated structure exists on smaller scales. We also do not exclude the possibility of other modes of reconnection, steady or unsteady, by these observations alone.

The results of this fully-automated search are consistent with the *ad hoc* searches in the literature, although thorough consideration of the backgrounds and observational biases involved have led us to some different conclusions. The primary statistical results of this survey are summarized as follows:

1. Large-scale reconnection structures form and persist in the solar heliographic plane out to a distance of at least 31 AU.
2. Exhaust traversals occur on all measurable timescales, from $\sim$ 1 minute up to $\sim$ 0.6 days.
3. The occurrence rate is a decreasing function of exhaust width, spanning scales of about 1-1000 R_E.
4. Reconnection exhaust flows are preferentially oriented along the Parker spiral direction.
5. Reconnection structure is more frequently observed near solar maximum.
6. Reconnection is more frequently observed at elevated β_i, relative to the mean solar wind.
7. Occurrences of the exhaust time signature are not statistically independent.
8. The implied reconnection process is always "fast," and the reconnection rate spans at least two decades.
9. The outflow kinetic energy density and thermal energy density of exhaust plasma are similar, and both scale linearly with the dropout in magnetic energy density.
10. The mean magnetic profile is not strictly discrete, and contains only weak substructure.
11. The mean flow profile fans out across the exhaust wedge, and is Alfvénic relative to the local plasma environment.
12. The mean velocity shear across each exhaust is on the order of the inflow speed.
13. In most, but not all cases, the level of compressive fluctuation in the inflow is too small to significantly disrupt the exhaust.

Most of the statistical tests applied have been designed to challenge the possibility of a quasi-steady model for the Voyager 2 survey events. Against that challenge, we have found compelling quantitative evidence for pressure equilibrium, dynamic maturity, and dynamic stability across the ensemble. We have also found that the composite picture emerging from the ensemble is very close to ideal, satisfying the scaling and qualitative expectations of simple, 2D, Petschek-like structure.

We claim, based on the conclusions above, that there exists a population of stable, large-scale exhaust structures that are driven by ordinary interactions between adjacent streams of different magnetic orientation, perhaps against a

backdrop of smaller, more random events. The Parker spiral alignment, solar cycle, and velocity inflow shear effects discussed in Sections 4.1 and 4.2 may all follow from reconnection in simple stream interface regions. Parker-like CIRs are simple two-stream collisions that are moderately sheared out to about 5 AU, where the the spiral completes its first full winding. It is these types of events that may provide the best laboratory for reconnection physics in the solar wind because the large-scale structure of the Parker spiral, which supplies the boundary conditions, is well known. In Chapter 6, we will study current sheets exclusively in well-modeled corotating interaction regions in order to better understand the role that quasi-steady reconnection plays there.

Chapter 5

Petschek shock pair analysis

In this chapter, we describe and employ a process for testing the Petschek hypothesis. It has been shown conclusively in Chapter 4 that the plasma discontinuities in most survey events are slow-mode-like. The inverse coupling between ion kinetic pressure and magnetic pressure at the two boundaries, demonstrated in Figure 4.10, defines these events as steepened slow-mode wave profiles. We now take this one step further by analyzing the flows across the discontinuities. In some cases, it is possible from conservation arguments to estimate the boundary planes and the slow-mode Mach numbers on either side.

This type of analysis requires some care, because if slow shocks do exist in the solar wind they are very weak. Furthermore, many of the secondary indicators one would use for shock detection are not available to us in this study. These indicators may include the presence of non-thermal shock-accelerated particles and enhanced plasma waves and radio emissions [2, 68]. There are experiments on board Voyager 2 to measure such effects; the Low Energy Charged Particle (LECP) Experiment and the Plasma Wave Spectrometer (PWS) have provided particularly useful data for the analysis of planetary bow shocks. Those experiments are designed to measure much larger and stronger phenomena than the interplanetary events studied here, however. The literature citing these data is concerned wholly with planetary magnetospheres and strong ICME encounters, and the associated MHD discontinuities that have been treated are strong, fast-mode shocks. A cursory inspection of the PWS and LECP experiment data sets has shown no correlated activity with any of the Voyager 2 reconnection signatures.

Studies at 1 AU have yet to reveal shock-accelerated particles in the vicinity of any interplanetary reconnection exhaust, a result that has been interpreted by some to mean that shocked Petschek reconnection does not occur in the solar wind [39]. We are unable to reproduce or refute those findings with Voyager 2, however we are able to address the fundamental fluid aspects of the shock model. We show in this chapter that survey event inflows exhibit

acceleration consistent with slow-mode Mach transitions in a small number of cases.

5.1 Rankine-Hugoniot analysis of exhaust discontinuities

The Rankine-Hugoniot (RH) relations are the set of conservation equations governing continuity of magnetic, particle, momentum, and energy flux across MHD discontinuities (see, for example, [88]). If the magnetic fields and ion moments are known on either side of an MHD shock in its rest frame, the normal direction, $\hat{\mathbf{n}}$, is the unique direction that conserves the equations simultaneously, closing the set.

Kasper and Manchester (in preparation) have laid out a procedure to solve the RH relations for the most probable $\hat{\mathbf{n}}$ and applied it to hundreds of fast-mode interplanetary shocks observed by Wind, ACE, and IMP8. Their findings have been catalogued in the CfA Interplanetary Shock Database [50] and have previously been used for studies of the connection between interplanetary shocks and geomagnetic storms (i.e. [49]). In their process, all unique pairwise combinations of measurements before and after each shock are drawn from hand-selected regions. For each combination, the corresponding values of a set of conserved quantities, $\{X\}$, are calculated and compared. The result is a distribution of differences for each conserved quantity and each trial value of $\hat{\mathbf{n}}$. A χ^2 statistic, quantifying the degree to which conservation is violated, is derived for each trial value of $\hat{\mathbf{n}}$. This χ^2 is equivalent to the goodness-of-fit parameter when the pairwise data for a conserved quantity, X, is compared to the equation $X_{upstream} = X_{downstream}$. A combination of goodness-of-fit parameters, weighted according to the propagated standard deviations of each measured quantity, gives a χ^2 for the full system. The most probable $\hat{\mathbf{n}}$ is that which minimizes the total χ^2 on the unit sphere.

Fast-mode shocks in the solar wind are usually identified with ICMEs, and are frequently strong and well-resolved. Because the analysis is the same for any type of planar MHD discontinuity, we can apply this process to candidate slow-mode shock events with essentially no modification. For each reconnection event in the Voyager 2 data set with well-resolved boundaries, we can hypothesize slow-mode shock transitions and attempt to find a convergent solution that is fully consistent with Petschek's model.

5.1.1 Jump conditions

Consider an MHD shock with normal $\hat{\mathbf{n}}$ and velocity $\mathbf{v}_s$ with respect to the interplanetary medium. Also assume that the solar wind plasma has a well-defined scalar pressure, p, and polytropic equation of state with adiabatic index

$\gamma = 5/3$. In a co-moving frame of reference such that $\mathbf{v} = \mathbf{u} - \mathbf{v}_s$, the jump conditions across the shock are given below. Square brackets are used to denote the change in the conserved quantity across the shock, i.e. $[X] \equiv X_{upstream} - X_{downstream}$.

- Conservation of mass:

$$[nv_n] = 0 \tag{5.1.1.1}$$

- Conservation of magnetic flux (3 equations):

$$[B_n] = 0 \tag{5.1.1.2}$$

$$[(\mathbf{v} \times \mathbf{B})_\perp] = 0 \tag{5.1.1.3}$$

- Conservation of momentum flux (3 equations):

$$\left[\underbrace{nm_0 v_n^2}_{ram\,pressure} + \underbrace{p}_{thermal\,pressure} + \underbrace{\frac{B_\perp^2}{8\pi}}_{magnetic\,normal\,stress} \right] = 0 \tag{5.1.1.4}$$

$$\left[\underbrace{nm_0 v_n \mathbf{v}_\perp}_{tranverse\,momentum\,density} - \underbrace{\frac{B_n \mathbf{B}_\perp}{4\pi}}_{magnetic\,shear\,stress} \right] = 0 \tag{5.1.1.5}$$

- Conservation of energy flux:

$$\left[\left(\underbrace{nm_0 \frac{v^2}{2}}_{kinetic\,energy\,density} + \underbrace{\frac{\gamma}{\gamma - 1} p}_{heat} \right) v_n + \underbrace{\frac{1}{4\pi} (\mathbf{E} \times \mathbf{B})_n}_{Poynting\,flux} \right] = 0 \tag{5.1.1.6}$$

These conservation laws comprise the Rankine-Hugoniot relations for an ideal MHD shock. The convective electric field is given by the ideal Ohm's Law, $\mathbf{E_{conv}} = -\frac{\mathbf{v}}{c} \times \mathbf{B}$. The subscripts n and $\perp$ denote vector components parallel and perpendicular to the shock normal, $\hat{\mathbf{n}}$, respectively. Under the usual approximation of a primarily hydrogen plasma, we let $m_0 \approx m_p$ and $n \approx n_p$ for the solar wind.

Finally, we have also assumed that ion heating dominates changes in the pressure, p. This assumption is a relatively poor one. The electron temperature

response to shocks in the solar wind, such as those driven by space weather events, can be significant but is typically several times smaller that than the proton response. In the ambient solar wind, small changes in electron temperature are generally poorly correlated to changes in the ion temperature. Fast measurement of the electron thermal distribution is not possible with PLS much beyond 1 AU, so electron corrections to Equations 5.1.1.4 and 5.1.1.6 are beyond the scope of this study.

5.1.2 RH analysis results for the Voyager 2 survey

A subset of 48 Voyager 2 outflow events was selected for RH analysis. Of all of the survey events, these were chosen specifically for sharp transitions at the boundaries with minimal long-wavelength variation in $\mathbf{B}$, $\mathbf{v}$, n_p, and w across the inflow and exhaust regions. These are the events that are most likely to have a well-defined sampling distributions for each X, as is necessary for the convergence of the RH analysis algorithm. We now describe the selection quantitatively.

Choosing RH analysis candidates

Consider some exhaust time signature. For each independent variable ($\mathbf{B}$, $\mathbf{v}$, n_p, and w), we can fit a linear regression to the data on each sub-interval (upstream, exhaust, downsteam) of the signature. If any of those linear regression trends are significant, the signature is excluded from the RH analysis. The significance of the trend is quantified by comparing to the standard deviation on that sub-region.

Let $\mathbf{m_y}$ be the slope and σ_y be the standard deviation in variable y for a sub-interval, T. The criterion for acceptance is given by

$$\frac{|\mathbf{m_y}|\,T}{2} < \sigma_y. \tag{5.1.2.1}$$

Each of the 48 events for which RH analysis was attempted satisfies this criterion, for all independent variables, on the associated upstream, exhaust, and downstream sub-intervals.

Results

The results of the RH analysis are summarized in Table 5.1. The RH analysis is convergent in cases where χ^2 has a distinct global minimum on the unit sphere. This is true of about one in four exhaust boundaries that were examined.

For most of the events, a convergent solution for $\hat{\mathbf{n}}$ existed either at both boundaries or at neither. Cases where solutions did exist were long duration,

	survey event boundaries		
	upstream	downstream	both
$\hat{\mathbf{n}}$ convergence	13	12	10
$\chi^2/\nu \leq 10$	11	7	7
$\chi^2/\nu \lesssim 1$	4	2	1
slow-mode sonic transition (68%)	3	3	3
$\theta_{\mathbf{B}\,\hat{\mathbf{n}}} \sim 90°$	4	1	1

Table 5.1: Summary of Rankine-Hugoniot analysis results for the 48 selected events. The number of events satisfying each condition at left is tabulated. $\theta_{\mathbf{B}\cdot\hat{\mathbf{n}}}$ denotes the angle that the upstream magnetic field makes with the shock normal.

lasting 10 minutes to a few hours, and the boundary normals were all within a range $-30° < \phi < 30°$. The latter is probably a direct consequence of the inflows being better resolved when aligned with the PLS cluster axis.

Statistically satisfactory solutions were not typical. In only one case did the best-fit $\hat{\mathbf{n}}$ produce a χ^2/ν value close to unity at both boundaries. In most cases, the χ^2/ν was on the order of 10, implying either that the errors have been underestimated or that one or more of the simplifying assumptions of the analysis are unsound. Given that the plasma-β for these survey events has not been strictly in the fluid regime, this result is not unexpected. Pressure anisotropy, which is not well-measured beyond 1 AU, may play a frequent and significant role. The anisotropic change in pressure across an MHD shock is a strong function of the $\theta_{\mathbf{B}\cdot\hat{\mathbf{n}}}$ and the plasma-β. A change of $\Delta(p_\perp - p_{\shortparallel}) \sim p_{dn}$ can occur, for example, when $\beta \sim 1$ and $\theta_{\mathbf{B}\cdot\hat{\mathbf{n}}} \sim 90°$ [18]. This anisotropy change would create a small violation in Equations 5.1.1.4 and 5.1.1.6. It is also possible that systematic changes in the electron component of the pressure, neglected here as noted, are significant as well.

For each of the convergent cases, the slow-mode Mach number was calculated on both sides of the discontinuity for cross-boundary flows. For three events, the analysis uncovered Mach number transitions that are consistent at a 68% certainty level with slow-mode magnetosonic shocks. In each of these cases there was an apparent magnetosonic transition on both sides of the exhaust. For only one of these cases was χ^2/ν of order unity. That event is discussed in detail in Section 5.2.

In several other cases, the apparent shock angle $\theta_{\mathbf{B}\cdot\hat{\mathbf{n}}}$ was identical, within error, to 90°. In those cases, the shocks are in the "switch-off" limit, and the slow wave speed is identically zero upstream. The associated Mach number is undefined, but these have also clearly been identified as slow shocks. For the other slow-mode shock events, $\theta_{\mathbf{B}\cdot\hat{\mathbf{n}}}$ was between 60° and 80° at all six discontinuities.

5.2 Case study at 31 AU

The most distant event of the automated survey was observed on February 9, 1990 at a distance of 31.33 AU, shortly after Voyager 2 began to move out of the solar equatorial plane. Figure 5.1 shows a time series of Voyager 2 measurements over a six day period that included this event. Shaded in grey, the exhaust jet stands out due to the sharp increase in tangential velocity, v_T, and density, n_p. Local to the exhaust region are variations in the bulk speed, u, with periods on the order of one day and amplitude on the order of 10 km/s. Tracking gaps, which typically last half a day and occur every few days at this point in the mission, make the long-term structure of the solar wind on this scale difficult to assess. The event in question occurs at a weak compression region. The hypothesized shock pair occurs following a trough in velocity where a stream is being overtaken by a faster stream with nearly opposite magnetic field direction. Other speed increases correlated with density and temperature features in this time period suggest similar structure. The outflow and reconnecting magnetic field are oriented approximately in the $+\hat{\mathbf{T}}$ direction while the inflow is a mix of $\hat{\mathbf{R}}$ and $\hat{\mathbf{N}}$. We note that, as in many of the survey events discussed in Chapter 4, this jet is oriented roughly along the Parker spiral direction at the juncture of two merging streams. It is likely that the plasma environment local to the exhaust is a corotating interaction region in the late stages of merging, also referred to as a *merged interaction region* (MIR).

The plane of reconnection is well-defined by a basis $\hat{\mathbf{u}} \times \hat{\mathbf{v}}$, where $\hat{\mathbf{u}}$ is a unit vector parallel to the d'Hoffman-Teller frame velocity and $\hat{\mathbf{v}}$ is the orthogonal direction that maximizes the apparent inflow. $\hat{\mathbf{u}}$ is found numerically by minimizing the convected electric field variance, given by Equation 3.2.2.1, and using the initial guess

$$\hat{\mathbf{u}}_0 = \frac{\mathbf{B}_{up} - \mathbf{B}_{dn}}{\|\mathbf{B}_{up} - \mathbf{B}_{dn}\|}.$$

The (u, v) plane, containing the inflow, outflow, and reconnecting field vectors, is inclined about 33° to the ecliptic. The reconnecting field itself is approximately 0.25 ± 0.05 nT. Figure 5.2 shows the reconnection time signature in this plane. A guide field into the plane is also present of about 0.09 ± 0.05 nT.

The outflow convected past Voyager 2 over a period of 281 minutes. This corresponds to a distance of approximately 0.05 AU between the discontinuities. The orientation of the inflow and the reconnecting field imply that the reconnection site is extended somewhat in the $\hat{\mathbf{R}}$ direction and is probably continuous over at least ~ 0.04 AU.

The transition regions marked in Figure 5.2 are each very large compared to the ion inertial length scale normally associated with shock widths. If there are slow shock transitions in these boundary layers they must be very weak

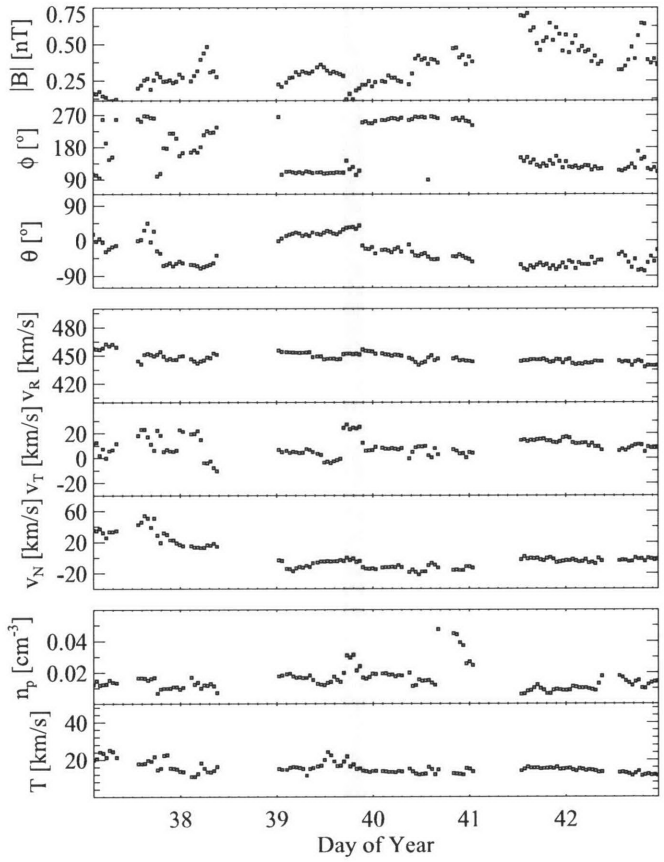

Figure 5.1: Voyager 2 hourly averages showing the plasma environment for three days before and after the 31 AU exhaust event. The grey bar highlights the exhaust region identified by the search algorithm. **Top panel:** magnitude and field angles for **B**. **Middle panel:** components of the proton velocity. **Lower panel:** proton density and temperature.

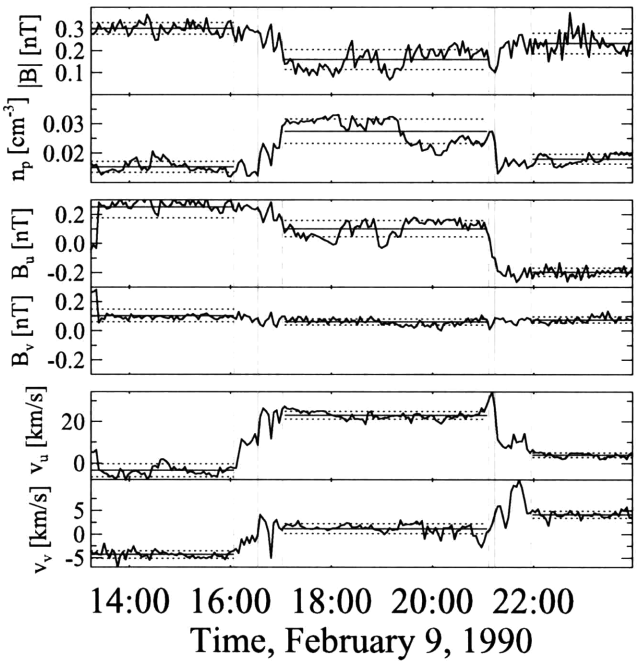

Figure 5.2: Reconnection-plane signature for the Voyager 2 reconnection exhaust observed at 31 AU. The search algorithm bounds are shown with solid vertical lines. The boundary layers used in the Rankine analysis are shown with dashed vertical lines. The average parameter values and 1-σ widths in each region are shown with solid and dashed horizontal bars, respectively. **Top panel:** Magnetic field strength, $|B|$, and proton density, n_p. **Middle panel:** B-field components in the reconnection plane, (u, v), where $\hat{u}$ is along the reconnecting field. **Lower panel:** velocity components in the reconnection plane.

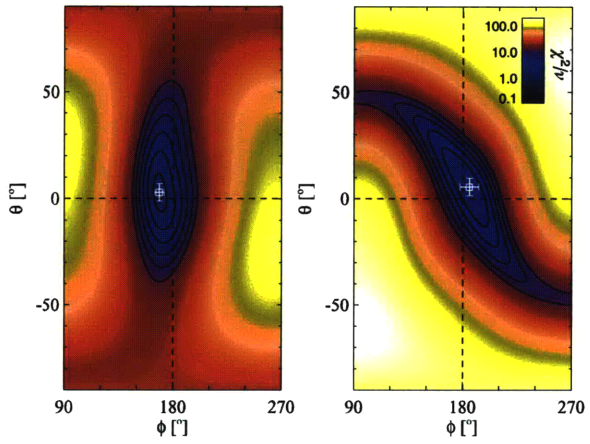

Figure 5.3: Map of the goodness-of-fit parameter, χ^2, per degree of freedom, ν, for a grid of trial values of $\hat{n}$ for each discontinuity. Plots span the unit hemisphere centered on $\hat{\mathbf{R}} = (0, 0)$ for the upstream (left) and downstream (right) discontinuities associated with the 31 AU event. White crosses indicate the most probable shock normals and the associated 68% confidence levels. The solid contours in the plot mark $\chi^2/\nu = \{2, 4, 6, 8, 10\}$.

because the magnetic field component along the presumed shock normal, and thus the slow wave speed, is very small. The shock transition must be on the order of our inflow speed estimate, $v_v \sim 6$ km/s, which is also of the same order as the random thermal velocities of the ions. The dimensionless reconnection rate for this site is $v_{in}/c_A \approx 0.1$. The inflow is in the direction of minimum variance, where random fluctuations in v_v are empirically ~ 2 km/s. Measurement error may be a further concern for flows that are less than 1% of the bulk speed. There is also substructure in these transition regions making it difficult to identify a single, clear transition from the inflow to the exhaust jet. The hypothesis that this outflow is bounded by shocks will therefore be tested by the consistency of the Rankine equations and the exhaust flow speed instead of by simple observation of a sudden transition in plasma parameters.

While we cannot deduce the detailed global structure of the reconnection site with observations from a single spacecraft, we will be able to show for the first time that the shock properties and separation between the shocks are consistent with an equilibrium Petschek flow structure.

We have applied the Rankine-Hugoniot jump conditions across the boundaries in search of a self-consistent solution (see Figure 5.3). The analysis predicts

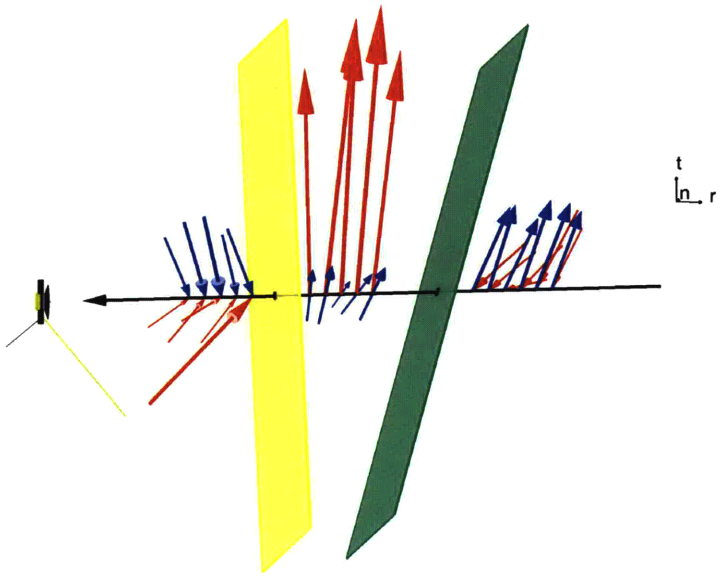

Figure 5.4: 3D rendering of the exhaust traversal. The effective trajectory of Voyager 2 through the exhaust is depicted by the black arrow. The yellow and green planes represent the shock surfaces from Rankine analysis. Blue arrows represent vector averages of the magnetic field along the traversal, scaled according to relative magnitude. Red arrows show the velocity vector, also scaled by to relative magnitude.

unique shock planes for each boundary that are roughly stationary with respect to the bulk flow speed. In the inertial frame of the spacecraft, the upstream and downstream shocks have radial speeds of 439 ± 6 km/s and 450 ± 2 km/s, respectively, compared to a bulk flow speed of 451 ± 3 km/s. These boundaries open in the $\hat{\mathbf{T}}$ direction and intersect at an x-line that is inclined $80 \pm 4°$ to the ecliptic plane. If we do assume planar symmetry, the ratio of the ion influx to outflux dictates the opening angle of the outflow according to $n_{in}v_{in}/n_{ex}v_{ex} = \tan\alpha$, where α is the opening angle and in and ex denote inflow and exhaust quantities, respectively. According to our (u, v)-plane estimates of v_{in} and v_{ex}, the opening angle is $9.46 \pm 1.2°$ for this outflow. This value is a good check on the opening angle predicted by Rankine-Hugoniot analysis. Figure 5.3 shows that the best-fit upstream and downstream shock normals are very nearly in the $\hat{\mathbf{R}}$ direction, with $(\theta, \phi) = (2.9 \pm 4.1°, 168.5 \pm 4.0°)$ and $(5.5 \pm 4.1°, 185.5 \pm 3.9°)$. These planes meet one another at an angle of $8.6 \pm 5.7°$, which is in good agreement with the flux conservation argument.

Figure 5.4 shows a rendering of the magnetic fields and ion velocities measured by Voyager 2, along with the best-fit shock planes obtained here. This visualization is a data-driven analogue of the Petschek exhaust schematic shown in Figure 3.4.

From the orientations we have derived, we can calculate the slow wave Mach numbers for flows across the boundaries. Based on our estimation of the slow wave speeds, it is likely that the boundaries of this reconnection exhaust are indeed slow magnetosonic shocks. At the first boundary, the upstream slow-mode Mach number for inflow along the calculated shock normal is 2.1 ± 1.5, while the downstream Mach number is 0.15 ± 0.7. Based on these error estimates, there is a 68% certainty that a slow magnetosonic transition has occurred in the first boundary. The same analysis shows that the upstream and downstream Mach numbers for the second boundary are 2.4 ± 1.2 and 0.13 ± 0.6, respectively. We can estimate an 81% certainty that a slow mode transition has occurred in the second boundary.

As a final check on this model, we compare the exhaust speed to the expected speed under the hypothesis that the primary mechanism for ion acceleration in the exhaust is shock acceleration. For a slow shock in the switch-off limit, plasma is accelerated to the Alfvén speed parallel to the shock front. The exhaust plasma is loaded on magnetic field lines that span the exhaust and are connected to the kinks in the field at the shocks. As those kinks propagate along the shocks at the Alfvén speed, the plasma in the exhaust is swept along at a speed of $c_A \cos\alpha$. The expected exhaust flow speed from our calculation of α is $\sim 25 \pm 4$ km/s. The actual exhaust speed is 24 ± 3 km/s, in very good agreement with the theory.

The ion Larmor radius, which sets the scale of the diffusion region itself, is about $\lambda_p \sim 1.1 \times 10^3$ km in the region of this observation. The projected closest approach from Voyager 2 to the x-line is 0.15 AU, or $\sim 14000\lambda_p$. This could correspond to the longest exhaust jet yet observed, yet it subtends only about $1/20$ of a Parker spiral winding at that distance. Because the boundaries of many of our survey events appear to be convex, this estimate is only a lower bound on the distance of closest approach. This jet length is small compared to the largest coherent scales expected at $\sim$ 31 AU from the sun and large compared to the kinetic scale of the diffusion region where reconnection was or had been taking place. It is in this range where modeling the global structure with planar boundaries, as we have, should be appropriate.

Chapter 6

Corotating interaction regions

Reconnection and current sheet forcing by stream interactions

In Section 4.1, it was shown that many reconnection exhaust structures in the solar wind are aligned with the Parker spiral. That particular result is a boon for reconnection physics research in the solar wind for several reasons. Firstly, because Voyager 2 is sun-facing, the Parker spiral alignment at large distances corresponds to alignment of reconnection inflows with the PLS cluster axis. As demonstrated in Section 5.2, that alignment has allowed us to make a very sensitive and important measurement of slow-mode magnetosonic transitions.

Secondly, reconnection jets that are aligned with the Parker spiral could be the direct result of field merging in corotating interaction regions. This type of scenario, which is illustrated in Figure 6.1, is a potentially very symmetric source of large-scale reconnection in the solar wind. The Parker spiral is the natural shape of laminar magnetic field lines and the leading/trailing edges of wind streams. Between two adjacent streams of different radial flow velocity and different magnetic field orientation, a current sheet exists at the boundary that is also globally Parker-spiral oriented. For long-lived, steady streams, this current sheet may be very large. For streams that are steady over some significant angle $\Delta\theta$ of solar rotation, the unperturbed current sheet has slab symmetry over a scale $\sim R\Delta\theta$.

With a single spacecraft time series the spatial extent of a reconnection jet or a current sheet can only be estimated in terms of consistency with model predictions. With additional information about the global structure and symmetry of the current sheet, however, that time series is a much more powerful measurement. Across a perfectly slab-symmetric, steady-state current sheet as one might try to create in the laboratory experiment, for example, a single cross

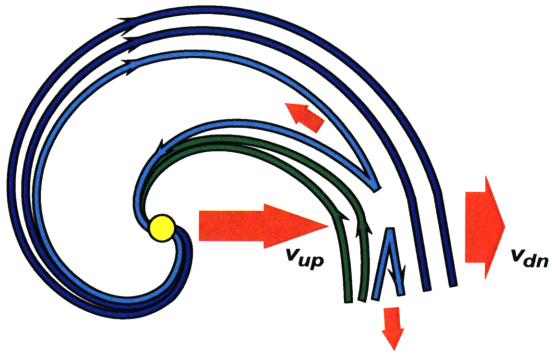

Figure 6.1: Schematic representation of global-scale reconnection in an antiparallel corotating interaction region (CIR). The sun, which spins about an axis directly out of the page, is depicted with the filled yellow circle. A fast stream with bulk speed v_{up}, transporting sunward-oriented magnetic flux (green), overtakes a slower stream with bulk speed v_{dn}, transporting anti-sunward-oriented flux (blue) in the solar wind. The reconnected field kinks (cyan) drive pair of sunward and anti-sunward outflows.

section is representative of the entire system. Current sheets that are bifurcated by spiral-oriented reconnection flows are the most ideal analogues for that type of experiment in the solar wind.

In this chapter, we propose that current sheets embedded in corotating interaction regions (CIRs) are a natural laboratory for reconnection physics in the solar wind. We will make use of the symmetries and range of driving conditions that these well-studied objects can offer as environments for reconnection. Through statistical comparison of those CIRs exhibiting reconnection structure and those not, the conditions conducive to reconnection structure can be controlled for. Based on the driving conditions in CIRs, we compliment our thus far event-driven study of reconnection outflows with a more general survey of forced current sheets, most of which are not observed in the reconnection exhaust state.

6.1 CIRs in the reconnection survey

Corotating interaction regions are among the most-studied phenomena in the solar wind because they provide simple boundary conditions for complex plasma processes such as shock formation, turbulent evolution, particle transport, and particle acceleration [38]. They also provide a simple, *in situ* dynamic phenomenon that is regularly observed and can be used as a benchmark for MHD computer simulations. The signature of plasma and magnetic compression that occurs when a fast stream overtakes a slow stream in the solar wind has been

characterized by epoch analyses with multiple spacecraft [31], and reproduced with some success using MHD models (e.g. [94]).

The simplest scenario under which a CIR might drive magnetic reconnection globally is the one shown in Figure 6.1, although the structure of the mixing region itself may become complex as the CIR develops. Dropouts in magnetic flux, including global-scale structures like crossings of the Heliospheric current sheet and local structures like magnetic holes and bifurcated current sheets, have been previously observed in conjunction with CIRs [38]. The elevated turbulence in CIR compression regions is a likely source of many of the latter such structures. The HCS, however, is an example of a current sheet that might be globally compressed within CIRs and driven to a Petschek-like state. Sunward and anti-sunward reconnection jets in the HCS have been observed at 1 AU with Wind. Bi-directional streaming of halo electrons has also been observed in sunward-oriented reconnection exhausts, which indicates continued connectivity with the sun. Sustained connectivity of spiral field lines with the sun is another encouraging indicator of the kind of global-scale symmetry we seek.

The model event of Section 5.2 may be one another example of a crossing where the HCS is observed in a reconnecting state. Consider the field angle histogram shown in Figure 6.2 for the 31 AU event encounter and over the month of its observation. In this case, the field angles directly upstream and downstream of the current sheet are representative of the steadily-maintained field angles over the entire month of observation. This event is the boundary between magnetic sectors with just the type of geometry that we have been describing. The field angles on all three timescales shown are very close to the angles one would predict from a ballistic propagation model of the solar wind with no dynamics, as in the Parker spiral. It is a reasonable assumption that similar driving conditions exist over a large arc of the spiral interface.

Reconnection events with inflow structure representative of large-scale CIR structure are not unusual among the Voyager 2 survey events. Particularly near solar maximum, when stream structure is most varied and interaction regions are frequent, as many as 60% of the survey events occur at sustained polarity reversals with driving flows that are consistent with changes in radial component of the bulk speed. CIRs occur as often as several times per month, and the same CIR is often observed for more than one Carrington period. CIRs that are observed only once are sometimes simply referred to as stream interaction regions (SIRs), in order to distinguish them from stream interactions that apparently span more than one full turn of the Parker spiral. The endurance of these structures is evident in spacecraft data from quasi-periodic variations in v_R near the Carrington rotation period. These variations become steepened into a sawtooth-shaped profile over time at distances of about 1-10 AU as plasma piles-up at the leading edges, and are accompanied by increases in magnetic and kinetic pressure there. In many cases, a magnetic sector boundary also occurs at the leading edge.

The radial speed and sector structure of three periods of solar wind from

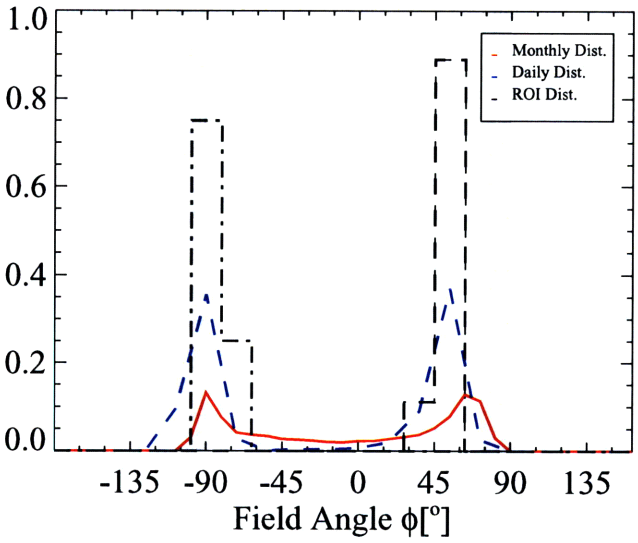

Figure 6.2: Normalized histograms of the B-field angle for data periods containing the case study event of Section 5.2. The black dot-dashed and single-dashed lines show the field angle in the inflow directly upstream and downstream of the event, respectively. The blue dashed line shows the distribution over the full day, and the solid red line shows the distribution over that month. The grey bars show the sunward and anti-sunward Parker angles, as measured at the reconnection exhaust.

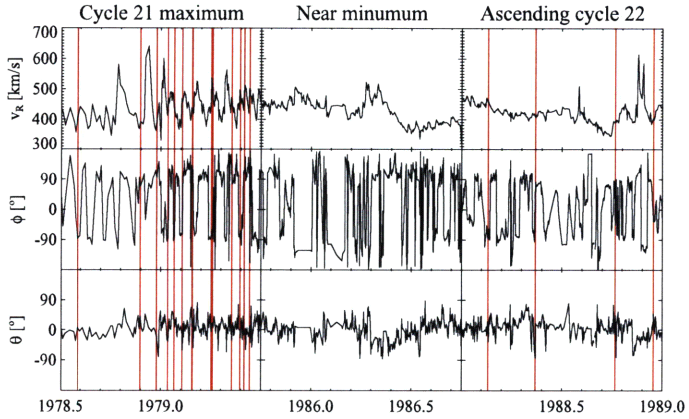

Figure 6.3: Daily averages of the radial solar wind speed and B-field angles, plotted as a function of time in years, for three periods of different solar activity. The radial speed exhibits the sawtooth oscillations representative of steepened CIRs, which disappear as the CIRs merge at large distances. Magnetic sectors are periods of nearly constant ϕ. Magnetic reconnection exhaust encounters are marked with vertical red bands.

the Voyager 2 mission is shown in Figure 6.3. On this plot, red vertical bars mark reconnection exhaust traversals. At the maximum of solar cycle 21, the quasi-periodic structure of v_R is pronounced near 3 AU, with the magnetic field changing sign about once per month. The average Parker field angle is about $110°$ (or $-70°$) at that distance. Ten of the seventeen reconnection exhausts over that period coincide with steep leading edges in v_R and discrete reversals of the in-plane field angle between $\phi \sim 110°$ and $\phi \sim 70°$. At the solar minimum that followed, no CIR structure was apparent and the magnetic sector structure was much less regular. As solar activity increased again going into cycle 22, Voyager 2 observed less CIR structure and less ordered magnetic structure at 25 AU than in the previous maximum, indicating that most CIRs become fully relaxed over the $\sim$ 100 days that it takes for the solar wind to convect to that distance. Four reconnection events were observed at the boundaries of comparatively irregular magnetic sectors, but it would seem that the type of large-scale reconnection we are associating with CIR driving does turn off naturally as CIRs relax.

CIRs supply a large parameter space of driving conditions for magnetic sector current sheets. Streams with speed differences of up to $\sim$ 200 km/s collide in the solar wind with flow shear angles from about $45°$ near 1 AU down to nearly $0°$ at large distances. While some CIRs coincide with strict reversal of the magnetic field direction, as in HCS crossings, most occur between streams with gentler field shears. This field shear depends on the relative flow speeds,

the distance from the sun, the solar source region, and the field components out of the heliographic plane. The global field shear angle across a CIR may be anywhere from 0° to 180°. CIRs may separate streams at any of the full range of characteristic densities, temperatures, and field strengths in the solar wind.

6.2 CIR identification and modeling

A catalogue of CIRs in the Voyager 2 data was assembled according to the definitive properties. Because these are events with long timescales (a few days to a month), it was expedient to identify these CIRs by inspection rather than with automation. For each event, a three-part region of interest was defined including a slow-stream region, a mixing region (denoted "*mix*"), and a fast-stream region. In the mixing region, the plasma and magnetic field pressure are elevated and the radial flow speed is intermediate to that of the slow and fast streams. Each is checked for consistency with a ballistic propagation model where the stream-fronts are mapped back to the surface of the sun. This model simply assumes that every plasma element convects freely from the sun to the observer with the measured radial speed, v_r. The stream fronts are the surfaces of constant heliolongitude or, equivalently, the plasma element trajectories in a frame corotating with the surface of the sun, i.e.

$$\frac{dR}{v_R} = \frac{Rd\theta}{v_\theta} = \frac{\sin\theta}{\Omega_\odot}. \tag{6.2.0.1}$$

For each interface, we require that this model produces well-ordered stream-fronts and a mixing region width that is consistent with merging between the fast and slow streams. Let the mixing region duration be T_{mix} and the heliographic radius of the observation be R_{obs}. If the fast and slow streams have an average speed $\bar{v}_R$ and a speed difference Δv_R, the structure can only be well-modeled in this way if

$$T_{mix} \lesssim \frac{R_{obs}\Delta v_R}{\bar{v}_R^2}. \tag{6.2.0.2}$$

The compression of the mixing region should also be well-behaved. The accumulated density should on the order of $n_{mix} \gtrsim n_{slow} + n_{fast}$. Implicit in both of these assumptions is that the CIR is still compressing, i.e. it is not yet at a stage where expansion due to the already accumulated pressure in the mixing region is comparable to compression by the inflowing plasma. CIRs that can be modeled this way are dynamically young. Beyond that stage, the Parker stream model would not apply, and the boundary conditions for reconnection would have to be obtained from some sort of dynamic model.

Two-hundred and forty stream interactions were identified in the Voyager 2 data set that satisfy these criteria. As a consistency check, it is noted that a

recent survey of Wind and ACE data identified about 40 SIR events per year over the last decade, occurring with 30% greater frequency near solar maximum than solar minimum[48]. The Voyager 2 rate is comparable to this, with the first 86 stream interaction regions identified in the first two years of the mission. The difference in plasma speed across these events ranged from 10 km/s up to 200 km/s, with a median of 34 km/s.

6.3 Embedded current sheets

Twenty-three percent of the CIRs in this study contained reconnection exhaust signatures. The data time series for one such event is shown in Figure 6.4, and the corresponding stream model is rendered in Figure ??. The mixing region is shown in green on both plots. The pile-up in the ion density, n_p, and magnetic flux, $|B|$, is apparent in the mixing region time series, along with the intermediate radial velocity component, v_R.

This CIR separates two nearly antiparallel magnetic sectors, each one lasting for about a week. Across the CIR, the magnetic field rotates by about 156°. We see that the bulk of that rotation occurs at a current sheet near the upstream edge of the mixing region, where the component B_T changes sign. The reversal of B_T occurs over a period of about 12 hours, and consists of a series of large fluctuations in the field and flow directions. Only about half of this transition was observed by Voyager 2, owing to two three-hour tracking gaps in the data over that period. One reconnection exhaust was clearly resolved, however, amidst the transition. A zoom-in on the exhaust is shown in the right panel of Figure 6.4.

It is interesting to note that, in this particular case, the local orientation of the reconnecting sheet is nearly orthogonal to its global orientation. One natural interpretation of this is that the current sheet has developed ripples, whether by an inherently non-steady reconnection process or by turbulence that has developed in the merging streams. In addition to compression, this CIR exhibits a significant out-of-plane flow, v_N, in the mixing region. This flow component approaches 40 km/s, apparently diverting a substantial fraction of the colliding particle flux. While the in-plane velocity shear is low for this CIR, the $\hat{\mathbf{N}}$-oriented shear component may drive Kelvin-Helmholtz vortices in RT-plane to create this reconnecting geometry.

6.3.1 Driving flows

Treating field rotations across CIRs as trial current sheets, we wish to investigate the reconnection states of the sheets as a function of the forcing and asymptotic boundary conditions. For each CIR, the magnetic fields in the fast and slow streams were compared. In cases where the fields were consistent with sunward

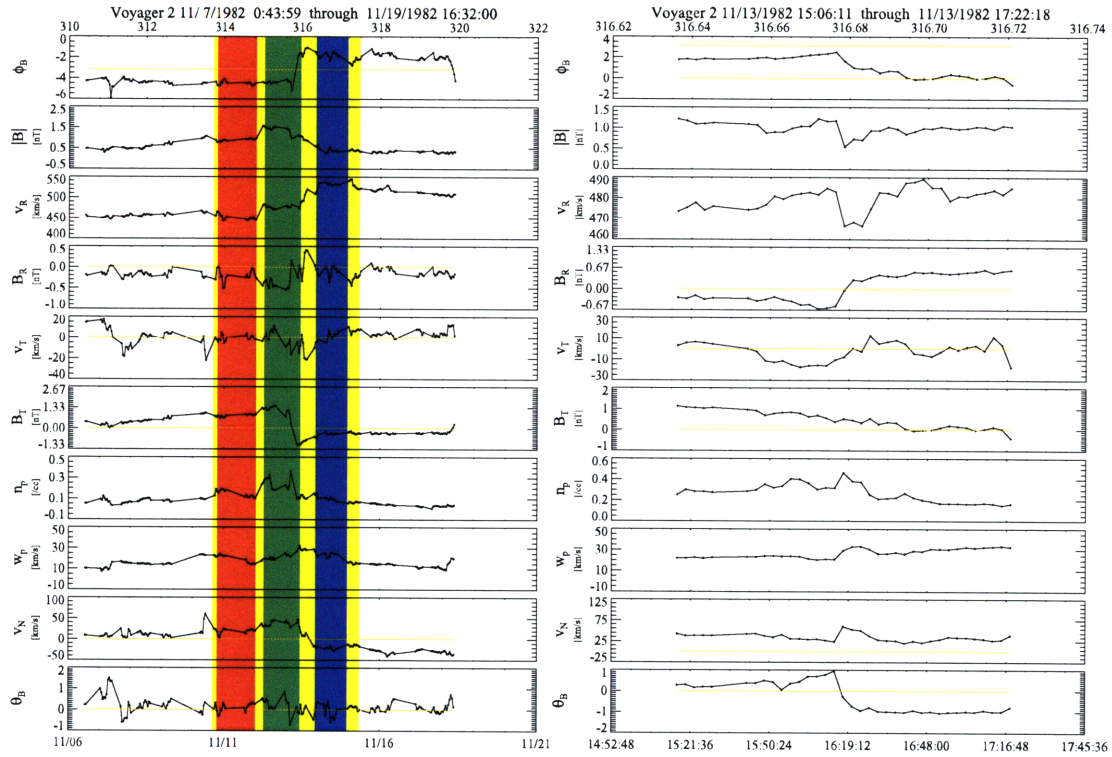

Figure 6.4: Example of a corotating interaction region observed by Voyager 2 at a distance of 10 AU. **Left panel:** The upstream, downstream, and interaction regions are highlighted in red, green, and blue, respectively. **Right panel:** the reconnection exhaust observed late in the interaction region. Plotted from top to bottom are the in-plane B-field angle in radians, the B-field magnitude, the radial flow speed, the radial B-field, the tangential flow speed, the tangential B-field, the proton density, the proton thermal speed, the normal flow speed, and the out-of-plane B-field angle in radians.

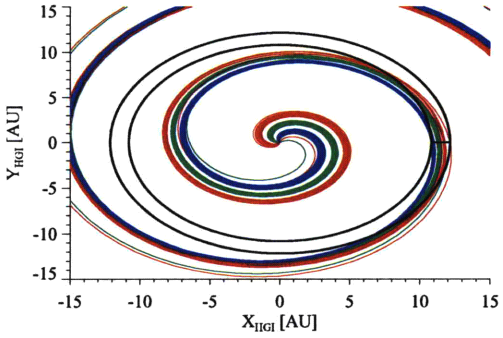

Figure 6.5: Stream-front model for the event shown in Figure 6.4 in arbitrary heliographic coordinates with $\hat{\mathbf{X}}_{\mathbf{HGI}} \parallel \hat{\mathbf{R}}$. The upstream, downstream, and interaction regions are shown in red, green, and blue, respectively. The inner black annulus shows the radius of initial observation and the outer radius shows the corresponding convected radius at the end of the observation.

Parker spiral field lines on one side and anti-sunward Parker spiral field lines on the other, the CIR was flagged as containing a magnetic sector boundary.

Figure 6.6 demonstrates the range of driving flows and velocity shears that were observed. The inflow Mach number, which is plotted on the vertical axis, is the Alfvén Mach number of the Δv_R component across the stream interface. It is also the global dimensionless reconnection rate across the CIR. The velocity shear Mach number, which is plotted on the horizontal axis, is a proxy for the instability of the interface to Kelvin-Helmholtz modes. CIRs with shear Mach numbers $\gtrsim 1$ may be unstable and develop vortical substructure. Sector boundary events that exhibited reconnection exhausts are shown in orange on the plot, with all other reconnecting events shown in blue. CIRs and reconnection signatures alike were most often seen at low inflow and shear Mach numbers, but the rate of occurrence was not strongly correlated to either parameter.

It is immediately apparent that the Kelvin-Helmholtz instability plays little or no role in suppressing magnetic reconnection. Whether or not the instability actually *promotes* reconnection, however, is an interesting question. The CIR interface was found to be KH-stable in 78% of cases. The percentage of those stable CIRs with reconnection exhaust structure was found to be 23%, compared to 28% of the unstable CIRs. The average current sheet thickness, χ, which is estimated for each exhaust as described in Section 4.1.1, was a factor of about four times thinner in the KH-unstable cases. It appears likely that the embedded current sheets are being deformed in those cases, though the field continues to reconnect. Multiple reconnection exhausts, as might be expected in strongly rolled-up reconnecting sheets, were not observed but might generally

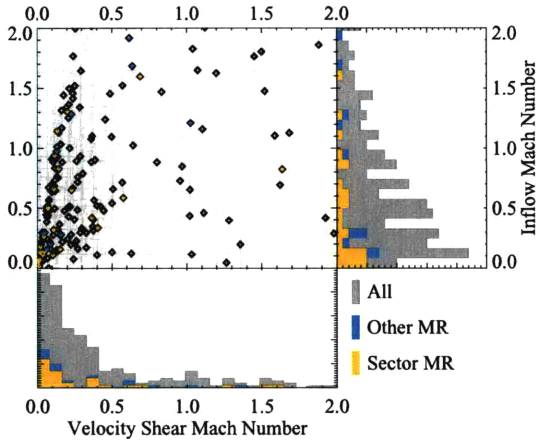

Figure 6.6: Voyager 2 CIR driving conditions. CIRs in the Voyager 2 data set are plotted and histogrammed according to the Mach numbers of the velocity shear and the velocity difference across the model interface. Cases containing a magnetic sector boundary in a reconnecting state are shown in orange. Cases containing other reconnecting sheets with irregular orientations are shown in blue.

be too thin to resolve.

The probability of observing a reconnection outflow was also not a strong function of the global reconnection rate. In over-driven cases, where the inflow Mach number was $\gtrsim 1$, however, the average estimated exhaust width was about 2.3 times thinner than in the less driven cases. This could be another indication that substructure develops when strong flows dominate the magnetic tension and pressure, as in the KH-unstable case. Once again, multiple exhausts were not observed.

6.3.2 Field shear and plasma-β

Figure 6.7 shows the number of interaction regions identified and their reconnection states as a function of the magnetic field shear angle. Although the number of total CIRs observed is a decreasing function of the shear angle, those CIRs containing magnetic sector boundaries tend to have large field shears. Because sector boundaries account for more than half of the CIR-associated reconnection in this study, the number of reconnecting current sheets was a strongly increasing function of the field shear angle. At low shear angles ($\leq 45°$), about 10% of CIRs contained reconnection exhaust signatures. At large shear angles ($\geq 135°$) , that fraction increased to 43%.

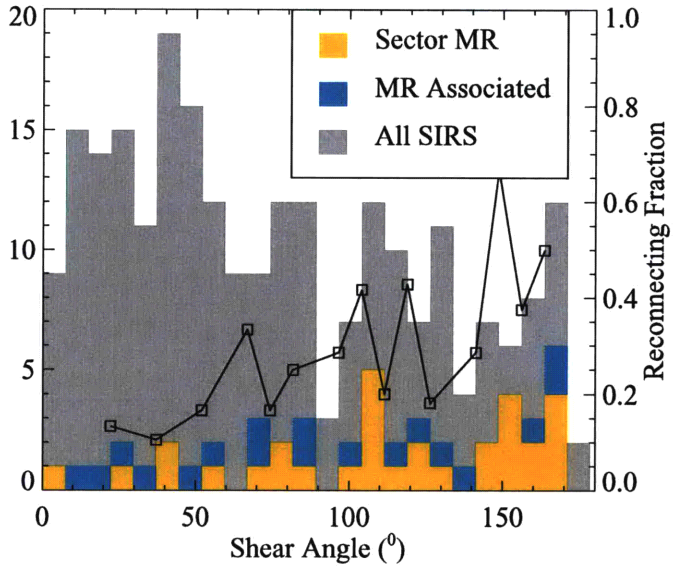

Figure 6.7: Histogram of the field shear angle between interacting streams in Voyager 2 CIRs. In orange are CIRs that drive sector reconnection events. In blue are CIRs where other reconnection exhaust signatures have occurred that are not aligned with the stream interface. The fraction of CIR-driven current sheets that are observed in the reconnection exhaust state is over-plotted.

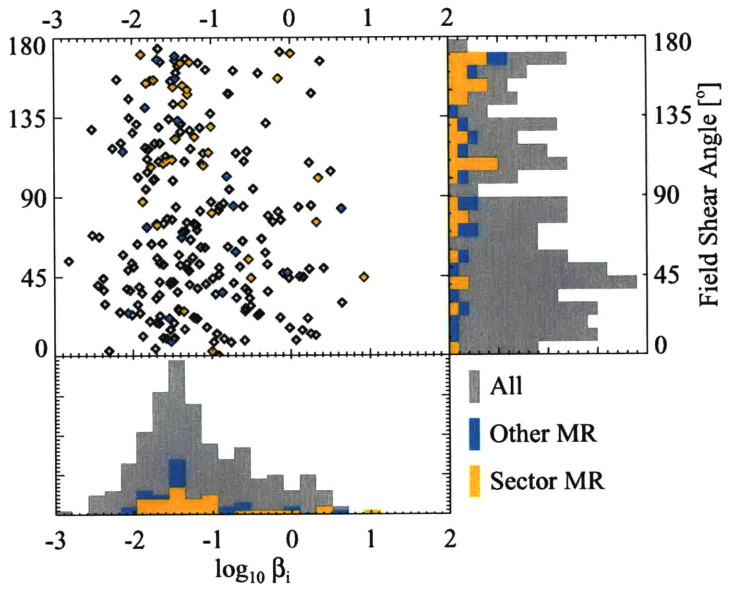

Figure 6.8: All CIRs in the Voyager 2 data set are scatter plotted according to the mean proton plasma-β and the field shear angle of the interacting streams. In orange are CIRs that drive sector reconnection events. In blue are CIRs where other reconnection exhaust signatures have occurred that are not aligned with the stream interface.

One frequently quoted inference from high-resolution studies at 1 AU is that magnetic reconnection across weak field shears, which are ubiquitous in turbulent environments, occurs only at low β [37]. The stability of a reconnection exhaust with high field shear, it is hypothesized, is more robust and can occur for a wide range of β. We have examined CIR current sheets across a wide parameter space in β and shear shear angle in order to discover if weakly-sheared current sheets are, in fact, more likely to be found in the reconnection outflow state at low β.

The field shear angle is scatter plotted against the logarithm of the plasma-β in Figure 6.8. We first remark that, as in the general survey from Chapter 4, the distributions of β associated with reconnecting and non-reconnecting current sheet environments are very similar. Just as before, we have found that the probability of observing a reconnection exhaust is slightly higher, on average, with higher β. As noted in Section 4.1.2, this finding contradicts one of the most frequently quoted results in the literature.

We suggested in Section 4.1.2 that this contradiction might be resolved

	$\beta < 0.13$	$\beta > 0.13$
$\alpha > 90°$	0.41	0.21
$\alpha < 90°$	0.1	0.22

Table 6.1: The fraction of CIR current sheets exhibiting reconnection exhaust structure in four regimes of the plasma parameter, β, and the magnetic field shear angle, α. The median value of β in the solar wind is 0.13.

by distinguishing between the ranges of exhaust scales involved in each study. If the claimed correlation between low-shear reconnection and low β is valid, the bias of the present study towards larger events and higher shears leads directly to a bias towards high β. The connection between low shear and low β, however, is also not present here. In fact, the reconnection state is particularly improbable for current sheets in the low-β, low-shear regime. The relative probability of the reconnection state is summarized for four regimes, corresponding to high/low β and high/low field shear angle, in Table 6.1. The spread in β is large for low-shear reconnecting sheets, spanning several orders of magnitude. The spread in β is significantly smaller for high-shear reconnecting sheets, which tend to have $\beta \sim 0.1$. For stream interaction regions with shear angles of less than 90°, the median plasma β is 0.13, identical to the median value for the solar wind as a whole. For regions with shear angles of greater than 90°, the median β is 0.04.

6.4 Discussion

Having detected many reconnecting current sheets with weak field shear, as previous authors have, and compared them to non-reconnecting current sheets under similar conditions, we conclude that weakly sheared current sheets on scales observable by Voyager 2 are not the most likely to reconnect. We have shown that when the frequency of shear angles is controlled for, the likelihood of observing a current sheet in the exhaust state is actually an increasing function of the field shear. We have also shown that the likelihood of observing the exhaust state increases with plasma-β. Finally, we have found that the reconnection exhaust state is equally likely to be observed over a large range of driving flow speeds and velocity shears, although there is some evidence that thin reconnecting sheets tend to occur under strong forcing and/or KH-unstable conditions.

Each of these results suggest that the scale of the exhaust widths and the detectability limit are playing significant roles. Our results lead us to ask the following questions:

1. If exhaust states are equally likely under all driving conditions, why are they only observed a small fraction of the time?

2. In cases where turbulence and/or KH instability are active, why are multiple jets not observed?

3. Why does the probability of reconnection with (α,β) contradict the previous claims from 1 AU studies?

The answers to all of these questions are probably derived from the sub-structure of the current sheet. If turbulent deformation is typical in all cases, then perhaps most or all forced current sheets in the solar wind reconnect primarily across irregular separatrices and not across a single, macroscopic laminar structure. In that case, forced current sheets not exhibiting outflows may simply be patchy or thin, and should not necessarily be interpreted as non-reconnecting. The low-shear, low-β turbulent current sheets observed at relatively high resolutions with 1 AU spacecraft are not detected here with Voyager 2. Instead, we find it likely once again that only a small fraction of the reconnection in the solar wind is carried out by broad, long-lived structures.

Chapter 7

Summary and future considerations

This thesis has presented a comprehensive, systematic study of the direct evidence for fast magnetic reconnection in solar wind environments observed by Voyager 2. We have designed and successfully implemented an automated algorithm that unambiguously detects current sheets with reconnection outflows in turbulent time series data. The biases and detection thresholds of this algorithm have been characterized so that the resulting reconnection survey can be put in context with other related studies.

Evidence of magnetic reconnection in the solar wind has been found, for the first time, at distances beyond the orbit of Jupiter. The solar wind magnetic field is found to be reconnecting via large, quasi-steady slow mode structures as far out as 30 AU. We have shown through a scaled superposition of different time signatures that about 1/3 of the flow diversion in these structures occurs very close to the slow-mode like discontinuities. Exhaust outflows tend to be fanned out, implying a wedge configuration, with a maximum Alfvénic flow along the central axis. In one instance, a well-developed reconnection structure was shown to be in good agreement with Petschek's slow-mode shock model for fast reconnection in a quasi-2D geometry. This is the first reported example of a reconnection exhaust that satisfies the full jump conditions for a stationary slow-mode shock pair.

Reconnection structures with crossing times from minutes to several hours have been shown to be strongly correlated with stream interactions in the solar wind, and accordingly also correlated with the solar activity cycle. These reconnection exhausts tend to align with the Parker spiral direction, reflecting reconnection of global-scale current sheets at corotating interaction regions. A complete investigation into the forcing of current sheets at CIRs in the Voyager 2 data revealed that detectable reconnection structure occurs in about 23% of

globally CIR-forced current sheets. Signatures of this kind are most likely to be observed for current sheets where the magnetic field shear and the plasma-β are high. Evidence has been found of thinner reconnecting current sheets in interfaces that are strongly sheared and potentially unstable to Kelvin-Helmholtz modes.

The picture of fast reconnection in the solar wind that emerges from this study is incomplete. While we have verified that reconnection occurs in quasi-steady, Petschek-like structures under a wide range of conditions, the increased rate of occurrence at short timescales and the absence of reconnection signatures under most forced current sheet conditions lead us to believe that we have seen only a small part of the picture. The emerging emphasis on large, steady reconnection structure in the literature today is probably a direct result of the fact that large, steady structure is more easily resolved and interpreted than small, short-lived, and perhaps stochastic structures. Future statistical work in this area should continue to focus on the scaling statistics of outflow-like structures at timescales and length scales approaching the ion inertial length. A full understanding of magnetic relaxation in the solar wind will require us to connect this scaled fluid-like outflow behavior on long-lived current sheets to a theory of the turbulent current sheets that dominate on the smallest scales. As theoretical, computational, and observational efforts converge on such a picture, we envision several avenues for continuing this work with Voyager 2 and other spacecraft.

One project with implications for shock modeling involves the re-analysis of Voyager 2 particle distributions at slow-mode boundaries. In light of observations near 1 AU showing interpenetration of inflows, rather than shock transitions, across reconnection exhaust regions [39], the Voyager 2 exhaust distributions should be re-analyzed to check for double-Maxwellian distributions separated along the field. This is most easily accomplished for cases with radial inflows, such as the case study event of Section 5.2. In that particular case, no evidence of interpenetration was found. The two-Maxwellian analysis of all events, however, is ongoing.

The automated analysis characterized here can be also be applied exhaustively to data from Wind, ACE, and other spacecraft. We can use this tool to build the largest possible statistical database and to better characterize the outflow scaling distributions at 1 AU. Based on the techniques used here and elsewhere to estimate exhaust sizes, orientations, and reconnection rates, it will be possible to make some model-dependent estimates of the total volumetric reconnection rate in the solar wind under different conditions. By studying the heating of the solar wind and the decay of the magnetic field systematically, the energy budget and global role of quasi-steady reconnection in the heliosphere might be placed in proper context.

Bibliography

[1] S. K. Antiochos, C. R. DeVore, and J. A. Klimchuk. A Model for Solar Coronal Mass Ejections. *Astrophysical Journal*, 510:485–493, January 1999.

[2] M. G. Baring, K. W. Ogilvie, D. C. Ellison, and R. J. Forsyth. Acceleration of Solar Wind Ions by Nearby Interplanetary Shocks: Comparison of Monte Carlo Simulations with ULYSSES Observations. *Astrophysical Journal*, 476:889–+, February 1997.

[3] A. Barnes. Collisionless Heating of the Solar-Wind Plasma. II. Application of the Theory of Plasma Heating by Hydromagnetic Waves. *Astrophysical Journal*, 155:311–+, January 1969.

[4] K. Baumgärtel. Soliton approach to magnetic holes. *Journal of Geophysical Research (Space Physics)*, 104:28295–+, December 1999.

[5] K. W. Behannon, M. H. Acuna, L. F. Burlaga, R. P. Lepping, N. F. Ness, and F. M. Neubauer. Magnetic field experiment for Voyagers 1 and 2. *Space Science Reviews*, 21:235–257, December 1977.

[6] K. W. Behannon, L. F. Burlaga, J. T. Hoeksema, and L. W. Klein. Spatial variation and evolution of heliospheric sector structure. *Journal of Geophysical Research (Space Physics)*, 94:1245–1260, February 1989.

[7] J. Birn, K. Galsgaard, M. Hesse, M. Hoshino, J. Huba, G. Lapenta, P. L. Pritchett, K. Schindler, L. Yin, J. Büchner, T. Neukirch, and E. R. Priest. Forced magnetic reconnection. *Geophysical Research Letters (Space Physics)*, 32:6105–+, March 2005.

[8] A. Bratenahl and C. M. Yeates. Experimental Study of Magnetic Flux Transfer at the Hyperbolic Neutral Point. *Physics of Fluids*, 13:2696–2709, November 1970.

[9] H. S. Bridge, J. W. Belcher, R. J. Butler, A. J. Lazarus, A. M. Mavretic, J. D. Sullivan, G. L. Siscoe, and V. M. Vasyliunas. The plasma experiment on the 1977 Voyager mission. *Space Science Reviews*, 21:259–287, December 1977.

[10] L. F. Burlaga and J. K. Chao. Reverse and forward slow shocks in the solar wind. *Journal of Geophysical Research (Space Physics)*, 76:7516–7521, 1971.

[11] L. F. Burlaga and J. F. Lemaire. Interplanetary magnetic holes - Theory. *Journal of Geophysical Research (Space Physics)*, 83:5157–5160, November 1978.

[12] L. F. Burlaga and N. F. Ness. Merged interaction regions and large-scale magnetic field fluctuations during 1991: Voyager 2 observations. *Journal of Geophysical Research (Space Physics)*, 99:19341–+, October 1994.

[13] L. F. Burlaga and N. F. Ness. Merged interaction regions observed by Voyagers 1 and 2 during 1998. *Journal of Geophysical Research (Space Physics)*, 105:5141–5148, March 2000.

[14] L. F. Burlaga, N. F. Ness, and M. H. Acuña. Magnetic Fields in the Heliosheath: Voyager 1 Observations. *Astrophysical Journal*, 642:584–592, May 2006.

[15] L. F. Burlaga, N. F. Ness, Y.-M. Wang, and N. R. Sheeley. Heliospheric magnetic field strength and polarity from 1 to 81 AU during the ascending phase of solar cycle 23. *Journal of Geophysical Research (Space Physics)*, 107:1410–+, November 2002.

[16] P. A. Cassak, M. A. Shay, and J. F. Drake. Catastrophe Model for Fast Magnetic Reconnection Onset. *Physical Review Letters*, 95(23):235002–+, November 2005.

[17] J. K. Chao and S. Olbert. Observations of bow shocks in interplanetary space. *Journal of Geophysical Research (Space Physics)*, 75:6394–6397, 1970.

[18] J. K. Chao, X. X. Zhang, and P. Song. Derivation of temperature anisotropy from shock jump relations: Theory and observations. *Geophysical Research Letters (Space Physics)*, 22:2409–2412, 1995.

[19] P. J. Coleman, Jr. Turbulence, Viscosity, and Dissipation in the Solar-Wind Plasma. *Astrophysical Journal*, 153:371–+, August 1968.

[20] S. R. Cranmer. Ion Cyclotron Wave Dissipation in the Solar Corona: The Summed Effect of More than 2000 Ion Species. *Astrophysical Journal*, 532:1197–1208, April 2000.

[21] J. F. Drake, D. Biskamp, and A. Zeiler. Breakup of the electron current layer during 3-D collisionless magnetic reconnection. *Geophysical Research Letters (Space Physics)*, 24:2921–2924, November 1997.

[22] L. A. Fisk and T. H. Zurbuchen. Distribution and properties of open magnetic flux outside of coronal holes. *Journal of Geophysical Research (Space Physics)*, 111:9115–+, September 2006.

[23] R. Fitzpatrick. *The Physics of plasmas*. 2008.

[24] M. Fränz, D. Burgess, and T. S. Horbury. Magnetic field depressions in the solar wind. *Journal of Geophysical Research (Space Physics)*, 105:12725–12732, June 2000.

[25] Harold P. Furth, John Killeen, and Marshall N. Rosenbluth. Finite-resistivity instabilities of a sheet pinch. *Physics of Fluids*, 6(4):459–484, 1963.

[26] S. P. Gary, R. M. Skoug, J. T. Steinberg, and C. W. Smith. Proton temperature anisotropy constraint in the solar wind: ACE observations. *Geophysical Research Letters (Space Physics)*, 28:2759–2762, July 2001.

[27] P. R. Gazis and A. J. Lazarus. Voyager observations of solar wind proton temperature - 1-10 AU. *Geophysical Research Letters (Space Physics)*, 9:431–434, April 1982.

[28] S. Giordano, E. Antonucci, G. Noci, M. Romoli, and J. L. Kohl. Identification of the Coronal Sources of the Fast Solar Wind. *Astrophysical Journal*, 531:L79–L82, March 2000.

[29] M. L. Goldstein, D. A. Roberts, and W. H. Matthaeus. Magnetohydrodynamic Turbulence In The Solar Wind. *Annual Review of Astronomy and Astrophysics*, 33:283–326, 1995.

[30] W. D. Gonzalez, B. T. Tsurutani, and A. L. Clúa de Gonzalez. Interplanetary origin of geomagnetic storms. *Space Science Reviews*, 88:529–562, April 1999.

[31] J. T. Gosling. Corotating and Transient Solar Wind Flows in Three Dimensions. *Annual Review of Astronomy and Astrophysics*, 34:35–74, 1996.

[32] J. T. Gosling, S. Eriksson, L. M. Blush, T. D. Phan, J. G. Luhmann, D. J. McComas, R. M. Skoug, M. H. Acuna, C. T. Russell, and K. D. Simunac. Five spacecraft observations of oppositely directed exhaust jets from a magnetic reconnection X-line extending $> 4.26 \times 10^6$ km in the solar wind at 1 AU. *Geophysical Research Letters (Space Physics)*, 34:20108–+, October 2007.

[33] J. T. Gosling, S. Eriksson, D. J. McComas, T. D. Phan, and R. M. Skoug. Multiple magnetic reconnection sites associated with a coronal mass ejection in the solar wind. *Journal of Geophysical Research (Space Physics)*, 112:8106–+, August 2007.

[34] J. T. Gosling, S. Eriksson, and R. Schwenn. Petschek-type magnetic reconnection exhausts in the solar wind well inside 1 AU: Helios. *Journal of Geophysical Research (Space Physics)*, 111:10102–+, October 2006.

[35] J. T. Gosling, S. Eriksson, R. M. Skoug, D. J. McComas, and R. J. Forsyth. Petschek-Type Reconnection Exhausts in the Solar Wind Well beyond 1 AU: Ulysses. *Astrophysical Journal*, 644:613–621, June 2006.

[36] J. T. Gosling, D. J. McComas, D. A. Roberts, and R. M. Skoug. A One-Sided Aspect of Alfvenic Fluctuations in the Solar Wind. *Astrophysical Journal*, 695:L213–L216, April 2009.

[37] J. T. Gosling, T. D. Phan, R. P. Lin, and A. Szabo. Prevalence of magnetic reconnection at small field shear angles in the solar wind. *Geophysical Research Letters (Space Physics)*, 34:15110–+, August 2007.

[38] J. T. Gosling and V. J. Pizzo. Formation and Evolution of Corotating Interaction Regions and their Three Dimensional Structure. *Space Science Reviews*, 89:21–52, July 1999.

[39] J. T. Gosling, R. M. Skoug, D. J. McComas, and C. W. Smith. Direct evidence for magnetic reconnection in the solar wind near 1 AU. *Journal of Geophysical Research (Space Physics)*, 110:1107–+, January 2005.

[40] J. T. Gosling, R. M. Skoug, D. J. McComas, and C. W. Smith. Magnetic disconnection from the Sun: Observations of a reconnection exhaust in the solar wind at the heliospheric current sheet. *Geophysical Research Letters*, 32:5105–+, March 2005.

[41] A. Greco, P. Chuychai, W. H. Matthaeus, S. Servidio, and P. Dmitruk. Intermittent MHD structures and classical discontinuities. *Geophysical Research Letters (Space Physics)*, 35:19111–+, October 2008.

[42] P. Hellinger, P. Trávníček, J. C. Kasper, and A. J. Lazarus. Solar wind proton temperature anisotropy: Linear theory and WIND/SWE observations. *Geophysical Research Letters (Space Physics)*, 33:9101–+, May 2006.

[43] M. Hesse and K. Schindler. A theoretical foundation of general magnetic reconnection. *Journal of Geophysical Research (Space Physics)*, 93:5559–5567, June 1988.

[44] C. M. Ho, B. T. Tsurutani, N. Lin, L. J. Lanzerotti, E. J. Smith, B. E. Goldstein, B. Buti, G. S. Lakhina, and X. Y. Zhou. A pair of forward and reverse slow-mode shocks detected by Ulysses at ~5 AU. *Geophysical Research Letters (Space Physics)*, 25:2613–2616, 1998.

[45] C. M. Ho, B. T. Tsurutani, E. J. Smith, and W. C. Feldman. Properties of slow-mode shocks in the distant ($> 200\,R_E$) geomagnetic tail. *Journal of Geophysical Research (Space Physics)*, 101:15277–15286, July 1996.

[46] E. W. Hones, Jr. Transient phenomena in the magnetotail and their relation to substorms. *Space Science Reviews*, 23:393–410, May 1979.

[47] P. A. Isenberg, C. W. Smith, and W. H. Matthaeus. Turbulent Heating of the Distant Solar Wind by Interstellar Pickup Protons. *Astrophysical Journal*, 592:564–573, July 2003.

[48] L. Jian, C. T. Russell, J. G. Luhmann, and R. M. Skoug. Properties of Stream Interactions at One AU During 1995 2004. *Solar Physics*, 239:337–392, December 2006.

[49] S. Jurac and J. D. Richardson. The dependence of plasma and magnetic field correlations in the solar wind on geomagnetic activity. *Journal of Geophysical Research (Space Physics)*, 106:29195–29206, December 2001.

[50] J. C. Kasper. CfA Interplanetary Shock Database. *CfA Interplanetary Shock Database, online catalogue.*

[51] J. C. Kasper, A. J. Lazarus, and S. P. Gary. Wind/SWE observations of firehose constraint on solar wind proton temperature anisotropy. *Geophysical Research Letters (Space Physics)*, 29(17):170000–1, September 2002.

[52] A. Lazarian, E. Vishniac, and G. Kowal. Model of Reconnection of Weakly Stochastic Magnetic Field and its Testing. In N. V. Pogorelov, E. Audit, P. Colella, and G. P. Zank, editors, *Astronomical Society of the Pacific Conference Series*, volume 406 of *Astronomical Society of the Pacific Conference Series*, pages 23–+, April 2009.

[53] A. Lazarian and E. T. Vishniac. Reconnection in a Weakly Stochastic Field. *Astrophysical Journal*, 517:700–718, June 1999.

[54] R. J. Leamon, W. H. Matthaeus, C. W. Smith, and H. K. Wong. Contribution of Cyclotron-resonant Damping to Kinetic Dissipation of Interplanetary Turbulence. *Astrophysical Journal Letters*, 507:L181–L184, November 1998.

[55] E. Leer, T. E. Holzer, and T. Fla. Acceleration of the solar wind. *Space Science Reviews*, 33:161–200, March 1982.

[56] R. P. Lepping, M. H. Acũna, L. F. Burlaga, W. M. Farrell, J. A. Slavin, K. H. Schatten, F. Mariani, N. F. Ness, F. M. Neubauer, Y. C. Whang, J. B. Byrnes, R. S. Kennon, P. V. Panetta, J. Scheifele, and E. M. Worley. The Wind Magnetic Field Investigation. *Space Science Reviews*, 71:207–229, February 1995.

[57] R. P. Lin, K. A. Anderson, S. Ashford, C. Carlson, D. Curtis, R. Ergun, D. Larson, J. McFadden, M. McCarthy, G. K. Parks, H. Rème, J. M. Bosqued, J. Coutelier, F. Cotin, C. D'Uston, K.-P. Wenzel, T. R. Sanderson, J. Henrion, J. C. Ronnet, and G. Paschmann. A Three-Dimensional Plasma and Energetic Particle Investigation for the Wind Spacecraft. *Space Science Reviews*, 71:125–153, February 1995.

[58] Y. Liu, J. D. Richardson, J. W. Belcher, J. C. Kasper, and R. M. Skoug. Plasma depletion and mirror waves ahead of interplanetary coronal mass ejections. *Journal of Geophysical Research (Space Physics)*, 111:9108–+, September 2006.

[59] N. F. Loureiro, A. A. Schekochihin, and S. C. Cowley. Instability of current sheets and formation of plasmoid chains. *Physics of Plasmas*, 14(10):100703–+, October 2007.

[60] E. Marsch. Kinetic Physics of the Solar Corona and Solar Wind. *Living Reviews in Solar Physics*, 3:1–+, July 2006.

[61] W. H. Matthaeus, P. Dmitruk, S. Oughton, and D. Mullan. Turbulent dissipation in the solar wind and corona. In M. Velli, R. Bruno, F. Malara, and B. Bucci, editors, *Solar Wind Ten*, volume 679 of *American Institute of Physics Conference Series*, pages 427–432, September 2003.

[62] W. H. Matthaeus and S. L. Lamkin. Turbulent magnetic reconnection. *Physics of Fluids*, 29:2513–2534, August 1986.

[63] N. F. Ness, K. W. Behannon, R. P. Lepping, and K. H. Schatten. Use of two magnetometers for magnetic field measurements on a spacecraft. *Journal of Geophysical Research (Space Physics)*, 76:3564–3573, 1971.

[64] K. Otmianowska-Mazur, G. Kowal, A. Lazarian, and E. Vishniac. Effects of turbulence on magnetic reconnection: 3D numerical simulations. In *IAU Symposium*, volume 259 of *IAU Symposium*, pages 671–674, April 2009.

[65] F. G. E. Pantellini. A model of the formation of stable nonpropagating magnetic structures in the solar wind based on the nonlinear mirror instability. *Journal of Geophysical Research (Space Physics)*, 103:4789–+, March 1998.

[66] E. N. Parker. The Solar-Flare Phenomenon and the Theory of Reconnection and Annihiliation of Magnetic Fields. *Astrophysical Journals*, 8:177–+, July 1963.

[67] E. N. Parker. Magnetic Neutral Sheets in Evolving Fields - Part Two - Formation of the Solar Corona. *Astrophysical Journal*, 264:642–+, January 1983.

[68] G. K. Parks. *Physics of space plasmas : an introduction*. 2004.

[69] G. Paschmann, B. U. Ö. Sonnerup, I. Papamastorakis, N. Sckopke, and G. Haerendel. Plasma acceleration at the Earth's magnetopause: evidence for reconnection. *Nature*, 282:243–246, November 1979.

[70] H. E. Petschek. Magnetic Field Annihilation. In W. N. Hess, editor, *The Physics of Solar Flares*, pages 425–+, 1964.

[71] H. E. Petschek. Magnetic Field Annihilation. *NASA Special Publication*, 50:425–+, 1964.

[72] T. D. Phan, J. T. Gosling, M. S. Davis, R. M. Skoug, M. Øieroset, R. P. Lin, R. P. Lepping, D. J. McComas, C. W. Smith, H. Reme, and A. Balogh. A magnetic reconnection X-line extending more than 390 Earth radii in the solar wind. *Nature*, 439:175–178, January 2006.

[73] O. A. Pokhotelov, R. A. Treumann, R. Z. Sagdeev, M. A. Balikhin, O. G. Onishchenko, V. P. Pavlenko, and I. Sandberg. Linear theory of the mirror instability in non-Maxwellian space plasmas. *Journal of Geophysical Research (Space Physics)*, 107:1312–+, October 2002.

[74] William Press, Saul Teukolsky, William Vetterling, and Brian Flannery. *Numerical Recipes in C.* Cambridge University Press, Cambridge, UK, 2nd edition, 1992.

[75] E. Priest and T. Forbes. *Magnetic Reconnection.* June 2000.

[76] Y. Ren, M. Yamada, S. Gerhardt, H. Ji, R. Kulsrud, and A. Kuritsyn. Experimental Verification of the Hall Effect during Magnetic Reconnection in a Laboratory Plasma. *Physical Review Letters*, 95(5):055003–+, July 2005.

[77] A. Retinò, R. Nakamura, A. Vaivads, Y. Khotyaintsev, T. Hayakawa, K. Tanaka, S. Kasahara, M. Fujimoto, I. Shinohara, J. P. Eastwood, M. André, W. Baumjohann, P. W. Daly, E. A. Kronberg, and N. Cornilleau-Wehrlin. Cluster observations of energetic electrons and electromagnetic fields within a reconnecting thin current sheet in the Earth's magnetotail. *Journal of Geophysical Research (Space Physics)*, 113:12215–+, December 2008.

[78] A. Retinò, D. Sundkvist, A. Vaivads, F. Mozer, M. André, and C. J. Owen. In situ evidence of magnetic reconnection in turbulent plasma. *Nature Physics*, 3:236–238, April 2007.

[79] A. K. Richter. *Interplanetary slow shocks.*, pages 23–44. 1991.

[80] Vincenzo Carbone Roberto Bruno. The solar wind as a turbulence laboratory. *Living Reviews in Solar Physics*, 2(4), 2005.

[81] D. A. Roberts, M. L. Goldstein, L. W. Klein, and W. H. Matthaeus. Origin and evolution of fluctuations in the solar wind - HELIOS observations and Helios-Voyager comparisons. *Journal of Geophysical Research (Space Physics)*, 92:12023–12035, November 1987.

[82] C. T. Russell and R. C. Elphic. ISEE observations of flux transfer events at the dayside magnetopause. *Geophysical Research Letters*, 6:33–36, January 1979.

[83] R. Samtaney, N. F. Loureiro, D. A. Uzdensky, A. A. Schekochihin, and S. C. Cowley. Formation of Plasmoid Chains in Magnetic Reconnection. *ArXiv e-prints*, March 2009.

[84] J. D. Scudder, H. Y. Karamibadi, H. X. Vu, and P. K. Montag. Two Rotational Discontinuities in Collision: An Alternate Interpretation to the Suggestion of Widespread "Magnetic Reconnection" in the Solar Wind. *AGU Fall Meeting Abstracts*, pages A5+, December 2008.

[85] S. Servidio, W. H. Matthaeus, M. A. Shay, P. A. Cassak, and P. Dmitruk. Magnetic Reconnection in Two-Dimensional Magnetohydrodynamic Turbulence. *Physical Review Letters*, 102(11):115003–+, March 2009.

[86] K. Shibata. Evidence of Magnetic Reconnection in Solar Flares and a Unified Model of Flares. *Astrophysics and Space Science*, 264:129–144, 1999.

[87] SIDC-team. The International Sunspot Number. *Monthly Report on the International Sunspot Number, online catalogue.*

[88] P. Song and C. T. Russell. Time Series Data Analyses in Space Physics. *Space Science Reviews*, 87:387–463, January 1999.

[89] B. U. O. Sonnerup, G. Paschmann, I. Papamastorakis, N. Sckopke, G. Haerendel, S. J. Bame, J. R. Asbridge, J. T. Gosling, and C. T. Russell. Evidence for magnetic field reconnection at the earth's magnetopause. *Journal of Geophysical Research (Space Physics)*, 86:10049–10067, November 1981.

[90] M. L. Stevens and J. C. Kasper. A scale-free analysis of magnetic holes at 1 AU. *Journal of Geophysical Research (Space Physics)*, 112:5109–+, May 2007.

[91] D. Sundkvist, A. Retinò, A. Vaivads, and S. D. Bale. Dissipation in Turbulent Plasma due to Reconnection in Thin Current Sheets. *Physical Review Letters*, 99(2):025004–+, July 2007.

[92] P. A. Sweet. The Neutral Point Theory of Solar Flares. In B. Lehnert, editor, *Electromagnetic Phenomena in Cosmical Physics*, volume 6 of *IAU Symposium*, pages 123–+, 1958.

[93] B. T. Tsurutani, C. Galvan, J. K. Arballo, D. Winterhalter, R. Sakurai, E. J. Smith, B. Buti, G. S. Lakhina, and A. Balogh. Relationship between discontinuities, magnetic holes, magnetic decreases, and nonlinear Alfvén waves: Ulysses observations over the solar poles. *Geophysical Research Letters (Space Physics)*, 29(11):110000–1, June 2002.

[94] A. V. Usmanov and M. L. Goldstein. A three-dimensional MHD solar wind model with pickup protons. *Journal of Geophysical Research (Space Physics)*, 111:7101–+, July 2006.

[95] D. A. Uzdensky. The Fast Collisionless Reconnection Condition and the Self-Organization of Solar Coronal Heating. *Astrophysical Journal*, 671:2139–2153, December 2007.

[96] A. A. van Ballegooijen and P. C. H. Martens. Formation and eruption of solar prominences. *Astrophysical Journal*, 343:971–984, August 1989.

[97] Y. C. Whang and L. F. Burlaga. Recurrent solar wind structures in the outer heliosphere. *Advances in Space Research*, 9:111–116, 1989.

[98] D. Winterhalter, M. Neugebauer, B. E. Goldstein, E. J. Smith, S. J. Bame, and A. Balogh. ULYSSES field and plasma observations of magnetic holes in the solar wind and their relation to mirror-mode structures. *Journal of Geophysical Research (Space Physics)*, 99:23371–+, December 1994.

[99] M. Yamada. *Recent Experiments on Magnetic Reconnection in Laboratory Plasmas*, pages 215–+. The American Geophysical Union, 1995.

[100] M. Yamada, Y. Ren, and H. Ji. Recent Progress in Study of Magnetic Reconnection in a Laboratory Plasma and Possible Application to Space Astrophysical Plasmas. In K. Shibata, S. Nagata, and T. Sakurai, editors, *New Solar Physics with Solar-B Mission*, volume 369 of *Astronomical Society of the Pacific Conference Series*, pages 391–+, October 2007.

[101] Masaaki Yamada, Hantao Ji, Scott Hsu, Troy Carter, Russell Kulsrud, Norton Bretz, Forrest Jobes, Yasushi Ono, and Francis Perkins. Study of driven magnetic reconnection in a laboratory plasma. volume 4, pages 1936–1944. AIP, 1997.

[102] T. Yokoyama and K. Shibata. What is the condition for fast magnetic reconnection? *Astrophysical Journal*, 436:L197–L200, December 1994.